ZEUS–01–019
22. June 2001

The Transverse Polarimeter (TPOL) Test Beam at DESY in January-February 2001

C. Collins-Tooth, V. Gharibyan, R.Hamatsu, M. Inuzuka,
K. Long, K.Matsuzawa, F. Metlica, S. Schmitt

k.long@ic.ac.uk, metlica@mail.desy.de, c.collins-tooth@ic.ac.uk: IC-London, ZEUS

hamatsu@comp.metro-u.ac.jp, inuzuka@mail.desy.de, kmatsu@mail.desy.de: Tokyo Metro-Univ, ZEUS

vaagn@hermes.desy.de: FLC-DESY, sschmitt@mail.desy.de: FH1-DESY

Abstract

The HERA ring is being upgraded during the long 2000-2001 shutdown to increase the HERA ring luminosity and provide longitudinal lepton beam polarization to the HERA experiments. The Transverse Polarimeter (TPOL) has also to be upgraded to improve the present transverse polarization measurement precision from ∼5% to ∼1%. The upgrade consists in a fast DAQ and a position sensitive detector for the TPOL. During January-February 2001 the TPOL calorimeter was instrumented with a prototype position sensitive silicon microstrip detector, and tested in a DESY electron test beam with energies up to 6 GeV. The TPOL test beam setup and results are presented in this note.

Contents

1 Introduction

HERA, the world's first and unique electron-proton collider, is used to study the structure of the proton in deep inelastic scattering in the low Bjorken-x and the large-Q^2 regions. During the long shutdown of 2000/2001, the HERA ring is being upgraded in order to collect luminosities five times larger than before, and to provide longitudinal electron beam polarization of up to 70 %. In parallel to the luminosity upgrade project, pairs of spin rotators are installed around the interaction regions of the ZEUS and H1 detectors. Therefore, after the upgrade it will be possible to carry out experiments using collisions between longitudinally polarized electrons and unpolarized protons.

Measurements that will be possible with longitudinally polarized electron beams include:

- The determination of the upper limit of the right-handed charged current cross section ($\sigma_R^{CC}/\sigma_L^{CC} \leq 0.02$) [1,2];
- The precise measurement of the electroweak parameters ($\Delta M_W \approx 55\,\mathrm{MeV}$) [3];
- The measurement of the light quark couplings to the Z^0 boson [4];
- Search for new physics as Contact Interactions.

In order to exploit the physics potential of HERA for the above measurements, it is required that the electron polarization, P, should be measured with an accuracy of $\delta P/P \leq 0.02$. This is the main goal of the Polarization 2000 project [5].

The electron polarization at HERA has been measured with two independent polarimeters: the longitudinal polarimeter (LPOL) and the transverse polarimeter (TPOL). The basic idea behind the polarization measurements is similar for both LPOL and TPOL. Circularly polarized laser light scatters off the polarized electron beam producing back-scattered Compton photons which are then detected in the calorimeter, which sits 60 m downstream of the interaction point [6, 7]. The LPOL installed near the East Hall measures the longitudinal polarization using the difference between the energy spectra of back-scattered Compton photons with right-circular polarized and left-circular polarized laser light. The TPOL, which is located near the West Hall, measures the transverse polarization from the asymmetry of vertical hit positions (y) at the calorimeter.

The TPOL calorimeter is a tungsten-scintillator sandwich calorimeter [8]. Because the upper and lower halves of scintillator layers are optically decoupled, the calorimeter can be considered to consists of two modules or parts. The vertical hit position, y, of the back-scattered Compton photons is not measured directly. Instead, y is deduced from the measured energy asymmetry η:

$$\eta = \frac{E_u - E_d}{E_u + E_d} \tag{1}$$

where E_u and E_d are the measured energy deposits in the upper (UP module) and lower module (DOWN module) of the calorimeter, respectively.

The electron transverse polarization P is related to the difference of the mean value of η obtained using left-circular polarized laser light (L) and right-circular polarized laser light (R) as follows:

$$\Delta\eta(E_\gamma) = \frac{<\eta>_L - <\eta>_R}{2} = P \cdot \frac{S_{3,L} - S_{3,R}}{2} \cdot \Pi_\eta \tag{2}$$

where $S_{3,L}$ and $S_{3,R}$ are related to the left- and right-circular polarization components of the laser light and E_γ is the Compton photon energy. From the above formula, the uncertainty on the measured polarization can be expressed as:

$$\delta P/P = \delta\Pi_\eta/\Pi_\eta + \cdots \tag{3}$$

therefore the analyzing power, Π_η, dominates the analysis.

The transformation from the measured η to y was measured in the test-beams at DESY and at CERN independently [8]. The results of fits for the $\eta - y$ transformation were included into the analyzing power term. This difference between the analyzing power obtained at DESY and that obtained at CERN can be as large as 4.4 %. This is significantly larger than our goal of $\delta P/P \leq 0.02$ [5]. In order to reduce the systematic uncertainty due to the $\eta - y$ transformation, the Polarization-2000 group decided to install a silicon-microstrip position sensitive detector in front of the TPOL calorimeter for the in-situ calibration of the $\eta - y$ transformation during data-taking.

The upgraded TPOL was installed at the T22 DESY test beam area in Halle 2 for testing during January 2001. From January 29th to February 12th in 2001, we carried out test-beam measurements. The upgraded TPOL consisted of a prototype silicon-microstrip position sensitive detector, a calibration fiber detector and the TPOL calorimeter together with a prototype of the new DAQ system for bunch-by-bunch and minute-by-minute polarization measurement. This note describes the TPOL and test-beam setup, and then presents the results from the test-beam measurements for the TPOL upgraded system.

2 The Experimental Setup

The complete TPOL polarimeter comprising three subdetectors i.e. the calorimeter, silicon detector and fiber detector, was tested with an electron test beam of maximum energy 6 GeV at DESY. It was installed in the T22 test beam area in Halle 2. The DAQ and trigger electronics were placed in the electronics hut right next to the T22 test beam area, see figure 1.

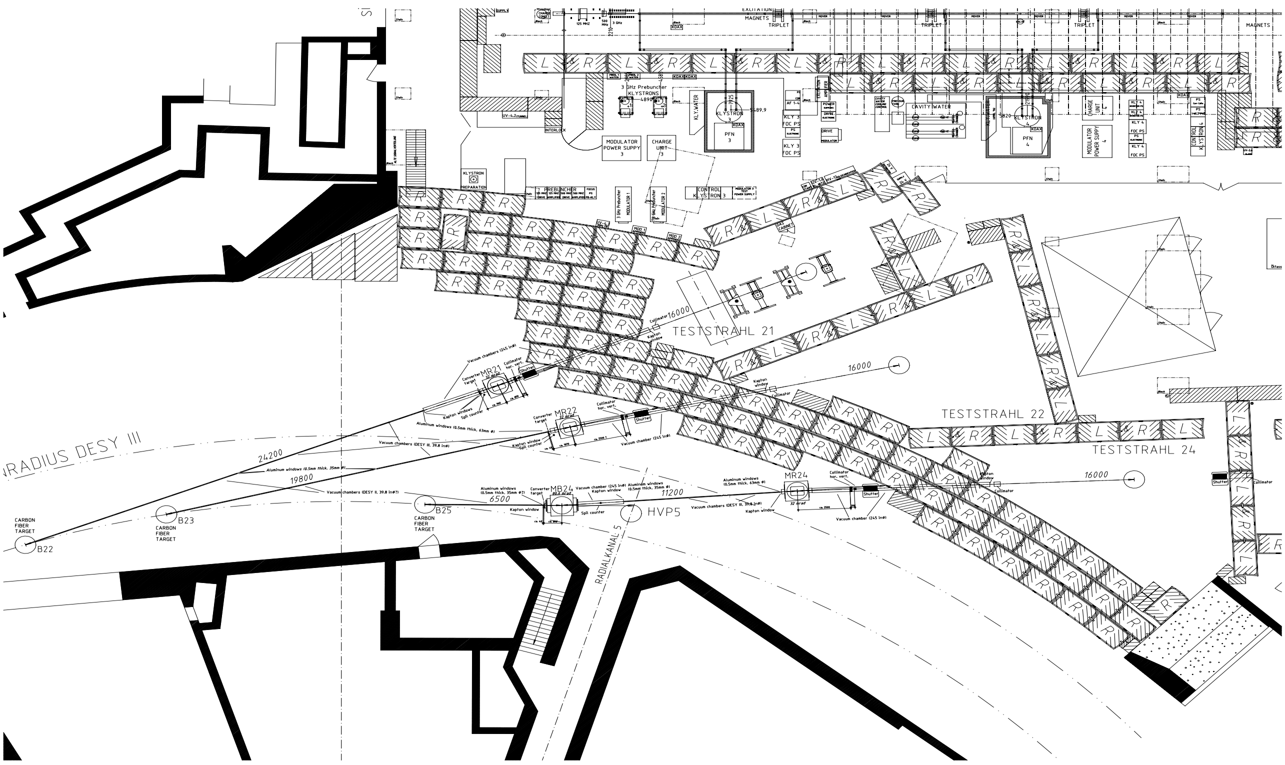

Figure 1: *DESY2 and the test beam areas, including T22, in Halle 2.*

2.1 The Electron Test Beam

The test beam is an electron test beam, having a maximum energy of 6 GeV. The electron test beam is obtained from the DESYII synchrotron ring which stores either e^+ or e^-, see figure 2. The DESYII ring has 292.8 m circumference, a 1.024 MHz revolution frequency, and reaches a maximum energy of 7 GeV. The test beam is obtained from the DESYII synchrotron ring in the following way. The DESYII beam is extracted and brought to hit a 10 μm fiber, giving rise to Bremsstrahlung photons. These in turn are converted by a converter plate into e^+/e^- pairs. A magnet separates the e^+ from e^- and a collimator plate allows only e^- to reach the test beam area. The test beam area is called T22, (figure 1). By changing the magnet current value it is possible to vary the test beam energy between 1 GeV and 6 GeV. There are 3.5 test beam particle spills per second, each spill is 50 $msec$. Figure 2 shows the layout scheme of the electron test beam.

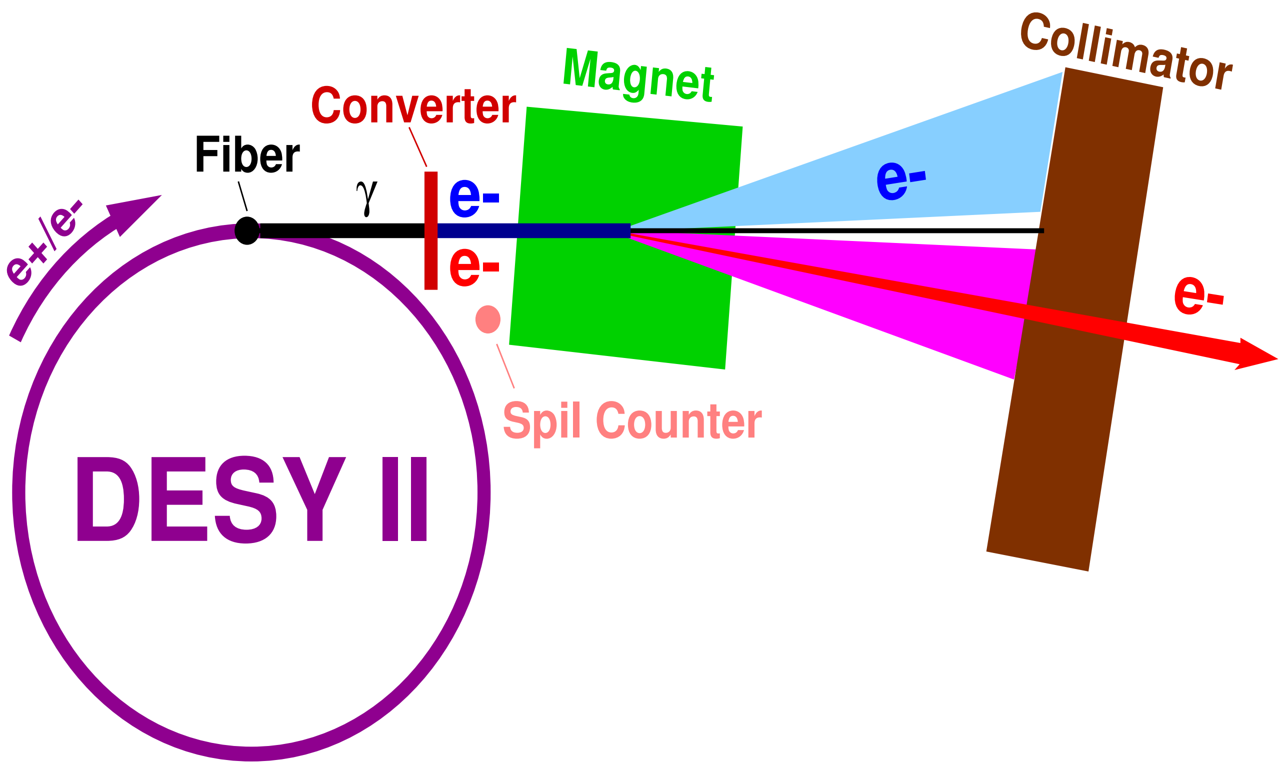

Figure 2: *Scheme for the electron test beam setup at DESY. In the scheme, after the converter plate the blue label (light grey) correspond to positrons (top)while the red label (dark grey) correspond to electrons (bottom).*

2.2 The Experimental Setup in the T22 Test Beam Area

Figure 3 shows a schematic view of the experimental setup in the area.

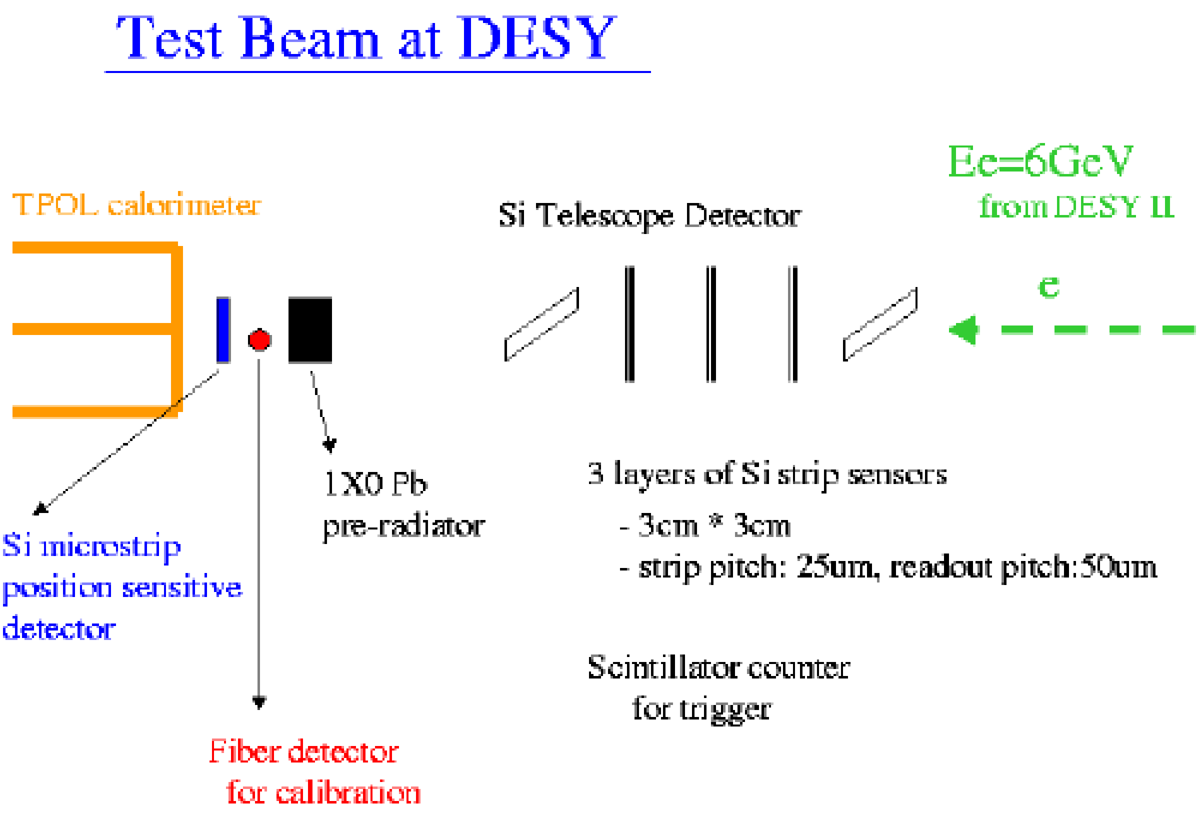

Figure 3: *A schematic view of the testarea.*

The TPOL spare calorimeter [8] (see Section 3.1) was aligned to the beam line. In front of the calorimeter, the silicon microstrip position sensitive detector (see Section 3.2) was installed together with a 1 X_0 of Pb pre-shower. The pre-shower is necessary to convert back-scattered Compton photons into electron-positron pairs in HERA tunnel. However, it was removed in the latter half of our measurements in order to understand the performance of the silicon detector with single electrons. For the calibration of the linearity of the silicon detector, a scintillating fiber detector (see Section 3.3) was also installed between the silicon detector and the pre-shower. The TPOL calorimeter, silicon detector and fiber detector were placed in an aluminium light-tight box on movable table. The horizontal and vertical table position was controlled remotely from the hut beside the test beam area.

The events were triggered by horizontal scintillator counters as mentioned in the next section. As shown in Fig. 3, a silicon telescope detector was placed [9] between the trigger counters. The telescope consists of three layers of silicon microstrip detectors with $50\,\mu$m readout pitch and 3cm*3cm active area. Each telescope plane was equipped with horizontal and vertical silicon-microstrips. The information of the reconstructed position from the telescope detector will be used to estimate the resolution and efficiency of our silicon position sensitive detector in Section 4.2.

2.3 Trigger and DAQ system

This section explains the trigger and DAQ system that was used. Scintillating counters are placed upstream and downstream the telescope detector (See Fig. 3) provided two kinds of trigger signals: 'Gated Trigger' and 'Ungated Trigger' signals as shown in Fig. 4.

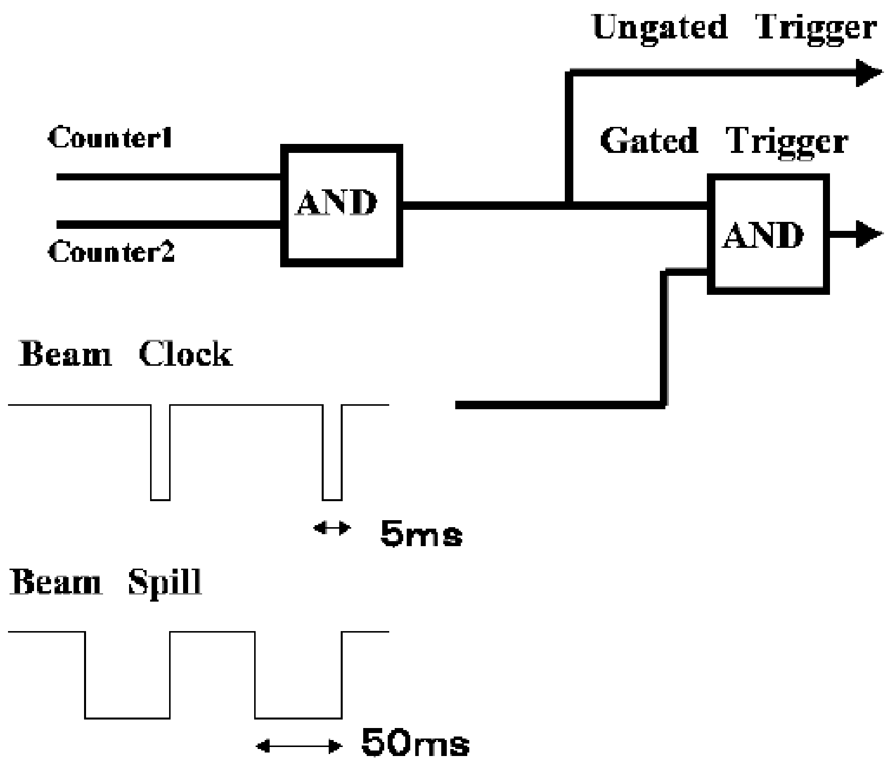

Figure 4: *Gated and Ungated Trigger logic.*

The Ungated Trigger signals were simply the coincidence of the two scintillation counters. Figure 5 shows a schematic diagram of the DAQ system in the hut. As shown in Fig. 5, the 'Si Trigger' is formed as a logical OR of the Ungated (or Gated) Trigger signal and a clock signal which is used as a 'Random Trigger'. The 'Random Trigger' is used to collect pedestal events. The Si Trigger signals are not sent to the DAQ systems while the SEQSI (See Section 3.2.1) inhibits the data-taking. The typical rate of the Si Trigger

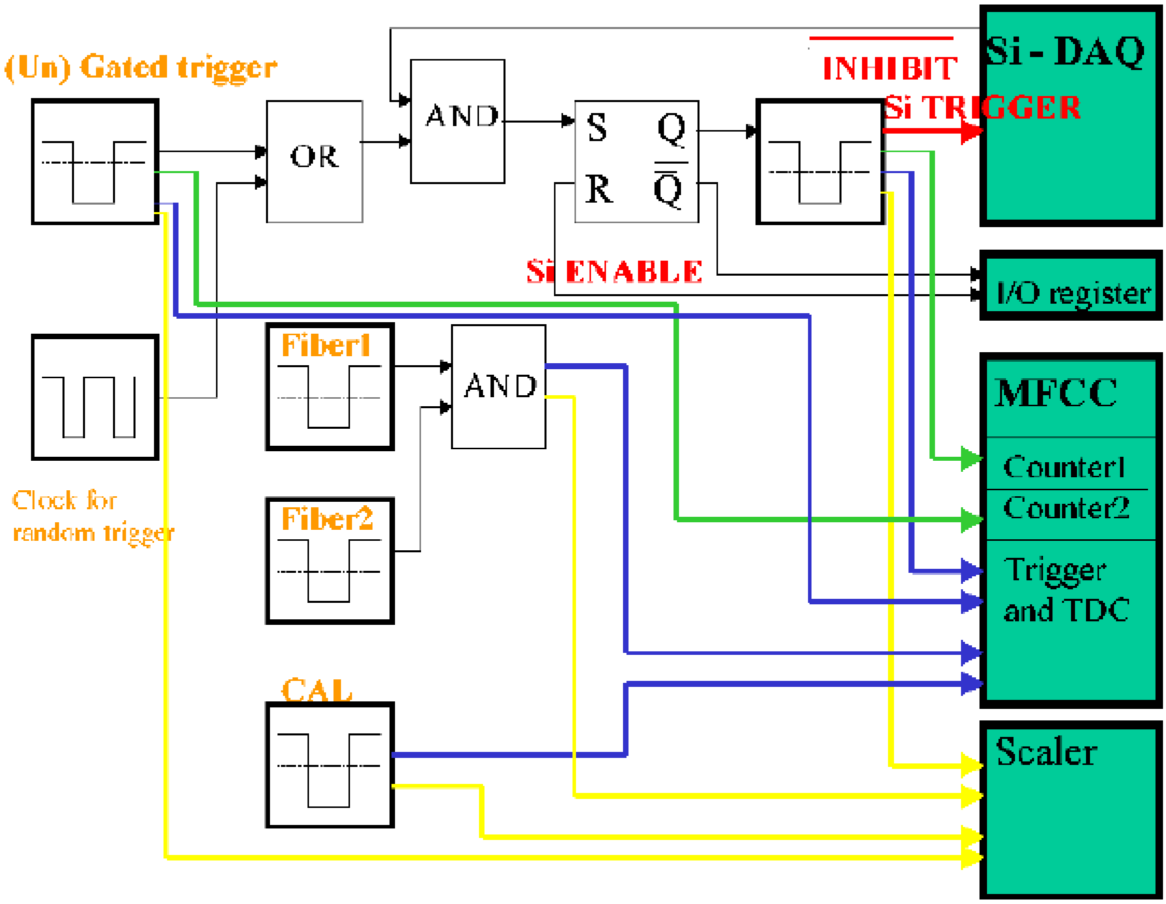

Figure 5: *DAQ system of the polarimeter.*

from the Ungated Trigger was about 20 Hz. Those events were mainly used to determine the precision of the fiber calibration (See Section 4.3).

More than 80 % of the Ungated Triggered events did not contain either the silicon data or telescope data because of the dead-time of the Si-DAQ and the telescope DAQ (not shown in Fig 5). This kind of event was not useful for the study of the alignment of the detectors, the estimation of the detector resolution and of the detector efficiency. In order to take events in which the data from both detectors are available efficiently, the Gated Trigger was used.

As mentioned in Section 2.1. the frequency and width of the electron beam was 3.5 Hz and 50 msec respectively. In order to form the Gated Trigger signal, we prepared the beam clock with a width of 5 msec synchronized to the end of each beam spill (See Fig. 4). The Gated Trigger is the coincidence of the Ungated Trigger signal and the beam clock. The typical rate of the Si Trigger was about 3 Hz. These events were mainly used for the study of the reconstruction of the silicon detector, alignment of the detector with respect to the telescope detector and the spatial resolution of the silicon detector (See Section 4.2).

As can be seen in Fig. 5, the trigger signals were also formed using the calorimeter and fiber signals. Although these trigger signals were used in the offline analysis, they were not used online for data-taking.

The energy deposits in the calorimeter and fiber detectors were read out by the local high rate DAQ system which consisted of a VME powerPC mother board equipped with a Multi-Function Computer Core, MFCC [5]. With the help of the latch and the IO-register, the Si-DAQ and the MFCC-DAQ were synchronized. Further, the counters on MFCC ensured a unique match of the events from the telescope, silicon and calorimeter.

2.4 The Telescope

The high position sensitivity of the silicon strip detector in the TPOL ($\sim \frac{80}{\sqrt{12}}\ \mu m$) compared to the calorimeter (position sensitivity $\sim 1000\ \mu m$) means that using the calorimeter alone to calibrate the position response of the silicon would not reveal the accuracy of the silicon. A calibration instument was needed for the testbeam which would expose the experimental limits of the silicon. For this reason the Telescope was used. The Telescope consists of three position sensitive silicon detectors (T1,T2 and T3). Each detector has a set of 600 vertical and a set of 640 horizontal strips, each of pitch 50 μm. Consequently, at 3.2cm $\times$ 3cm, the telescope silicon was of roughly nine times the area of the prototype TPOL silicon. Also included was a pair of scintillating finger counters (telescope finger counters) which acted as the trigger for the Telescope and TPOL.

2.4.1 Setup in the Test Beam

The Telescope was mounted as a unit on a movable table as close as possible to the TPOL. As part of another experiment, a fourth detector was inserted into the Telescope. For the

TPOL test this was considered to be 'dead' material. The TPOL was aligned with the Telescope along the beam axis. This arrangement is shown in figure 6.

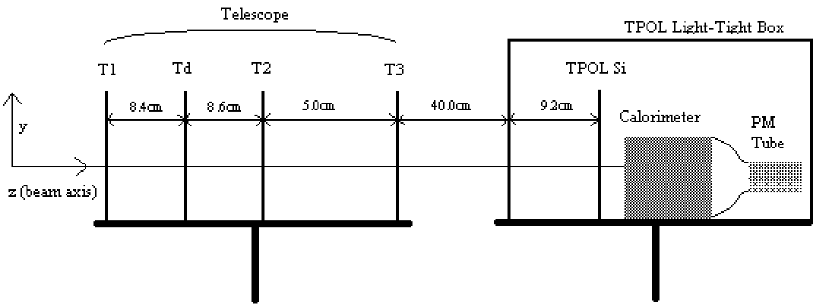

Figure 6: *The setup of the TPOL and Telescope in the test beam. The electron test beam arrives from the left in the picture*

3 The Polarimeter

The Transverse Polarimeter detector (TPOL) consisted of 3 subdetectors: calorimeter, silicon, and fiber detector. Each subdetector will be described in detail in the next subsections. Figure 7 shows the schematic layout of the 3 subdetectors, while figure 8 is a photo of the polarimeter installed in the testbeam area. The pre-radiator (or preshower) is a 5.6 mm thick x 30 mm diameter piece of lead, corresponding to 1 radiation length, 1 X_0.

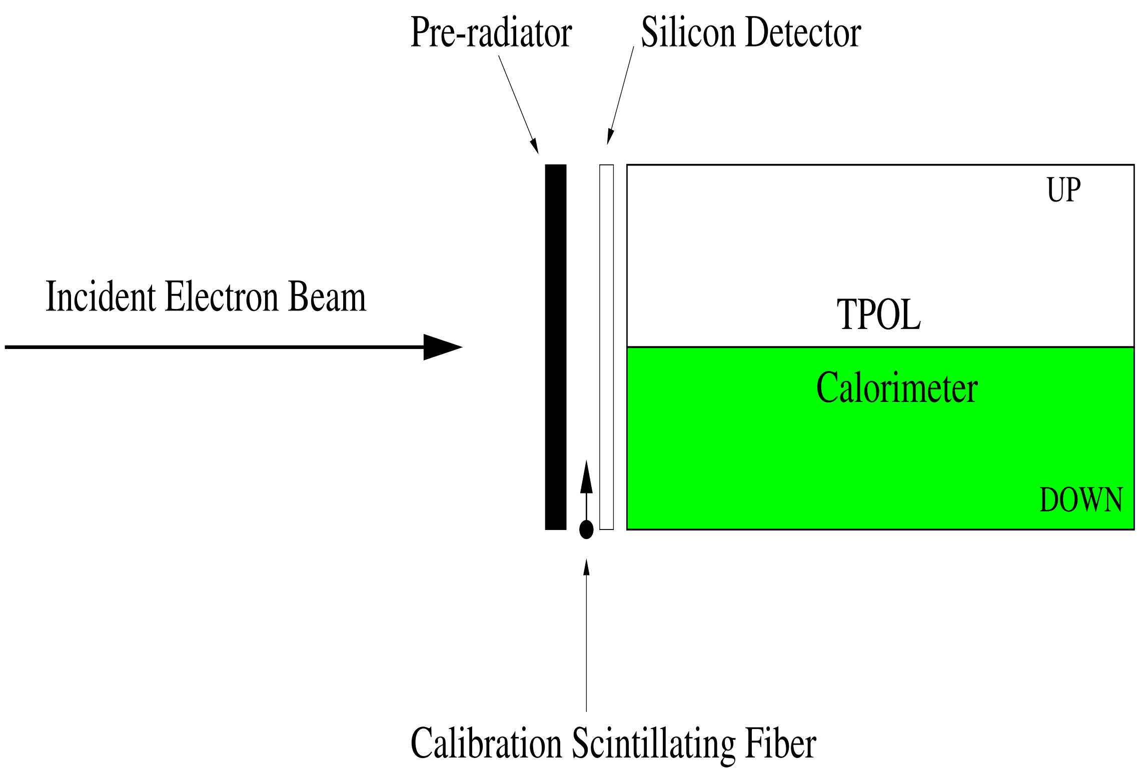

Figure 7: *Diagram showing the polarimeter detector setup, consisting of three subdetectors: calorimeter, silicon, and fiber detector. In the HERA tunnel setup, Compton photons are the particles incident on the TPOL. The pre-radiator is necessary for Compton photon conversion.*

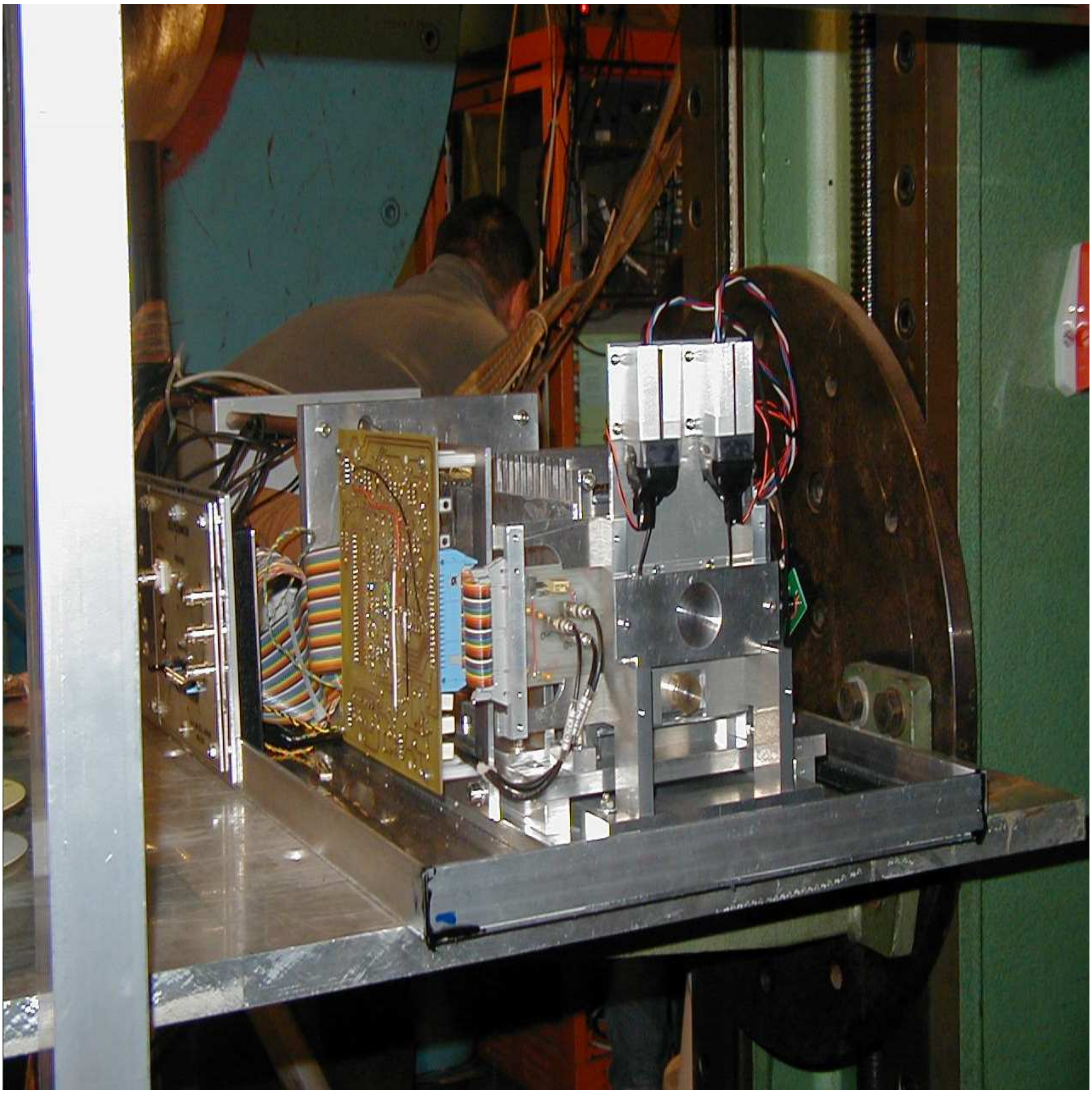

Figure 8: *Front view photo of the polarimeter mounted on the movable table in the test-beam area. The preshower (rectangular plate with circle in the middle) and the fiber PMs (directly above the preshower) with the silicon interface board (left board) can clearly be seen. The silicon detector board is fixed behind the preshower, only part of it is seen protruding towards the left (3 black cables are plugged into it). The calorimeter is positioned directly behind the silicon and preshower.*

3.1 The Calorimeter

The calorimeter [6], [7], [8] consists of 12 layers of tungsten and scintillator as shown in figure 9 . Each layer consists of a single absorber plate (DENSIMET17, $60 \times 55 \times 6.2$ mm^3, $1.6X_0$) set in a lead frame of $120 \times 100 \times 6.2$ mm^3 and two optically decoupled scintillator plates (SCSN-38, $120 \times 100 \times 2.6$ mm^3). Conceptually the calorimeter can be considered to consist of two calorimeters, one on top of the other; i.e. an UP and a DOWN calorimeter module.

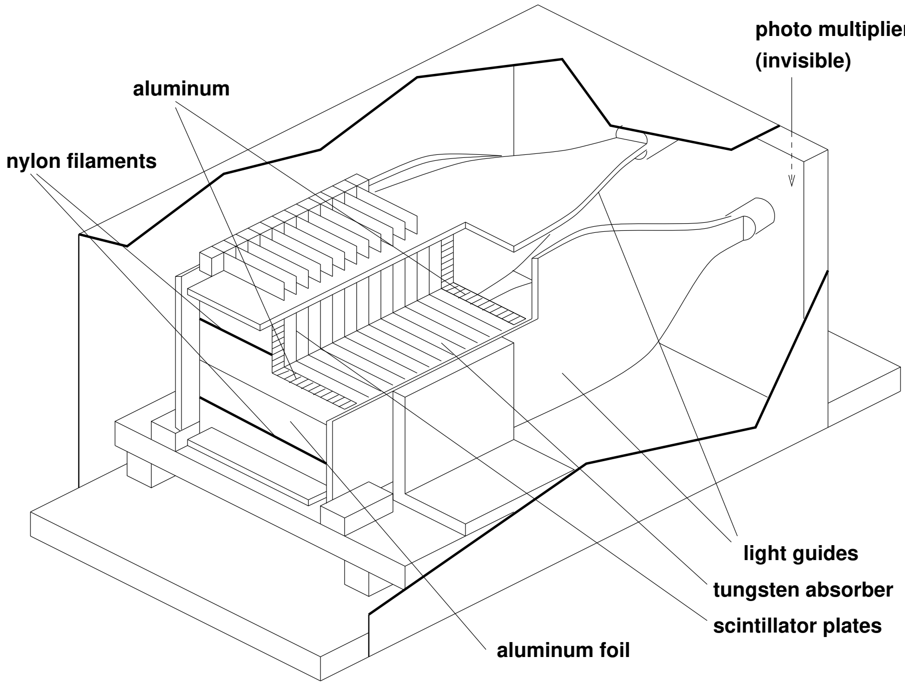

Figure 9: *A cut away, perspective view of the tungsten scintillator calorimeter. The calorimeter has an upper and a lower half which are optically decoupled. The scintillating light is collected by wavelength shifters on all four sides. The asymmetry of the shower development in the upper and lower half is used to measure the vertical projection of the impact point of the Compton photon.*

The scintillation light from each half is collected with wavelength shifters (WLS) along the top and the bottom of the detector (channels U and D). The WLS is made of an acrylic plate doped with a fluorescent material commercially called Y-7. The energy of an incoming photon is derived from the sum of the energies in the two halves:

$$E_\gamma = (E_U + E_D)\,, \tag{4}$$

and the vertical position is measured using the asymmetry of the energies:

$$\eta_V(y) = \frac{E_U - E_D}{E_U + E_D}. \tag{5}$$

For calibration purposes there are also WLSs on the right and the left sides which read the upper and lower halves together (channels R and L). Photo multiplier tubes (Hamamatsu R580) transform the light from the WLSs into an electrical signal. The voltages of the individual electrodes of the PMTs are generated by Cockroft–Walton bases which deliver constant cathode and anode voltages up to anode currents of 40 μA [10].

The calibration of the calorimeter is made by adjusting the voltages of the four PMTs with the detector centered in the electron beam. The relative calibration of channels L and R is done by measuring the distribution of the horizontal energy asymmetry η_H:

$$\eta_H(x) = \frac{E_L - E_R}{E_L + E_R}. \tag{6}$$

The distribution is Gaussian and the width is determined by light attenuation and photo-electron statistics. When the two channels are properly calibrated the mean of $\eta_H(x)$ is zero.

The vertical channels are calibrated utilizing the calibrated horizontal channels through the energy ratio

$$R(\eta_V) = \frac{E_V}{E_H} = \frac{E_U + E_D}{E_L + E_R}\,. \tag{7}$$

As the horizontal and vertical readout channels view the same scintillators, this ratio, apart from minor effects due to light attenuation in the scintillator, is independent of the position and energy if the relative calibration of U and D is properly set. The relative calibration of the horizontal and vertical channels is set with the requirement that at the center ($\eta_V = 0$) $R = 1$.

The fractional energy resolution defined as $\sigma(E)/E$ is dominated by sampling fluctuations and photo-electron statistics leading to $\sigma(E)/E$ scaling with $1/\sqrt{E}$. At high energies deviations from $1/\sqrt{E}$ can occur because of noise, pedestal fluctuations, non-uniformities and incomplete shower containment. Such effects are usually included by adding a constant term to $\sigma(E)/E$. In our case the additive constant term arises mainly from the momentum resolution of the DESY test beam and may be neglected by properly including the resolution into data errors.

The vertical position y_0 of an incoming high energy electron or photon is measured using the energy asymmetry η_V deposited in the upper (UP) and lower (DOWN) halves of the detector:

$$\eta_V(y_0) = \frac{E_U - E_D}{E_U + E_D}. \tag{8}$$

Using the sum of two exponentials as a parametrisation of the electro-magnetic transverse shower shape dE/dy [6], [8] :

$$f(y - y_0) \equiv \frac{dE}{dy} = P_1 e^{-P_2|y-y_0|} + P_4 e^{-P_3|y-y_0|} , \tag{9}$$

the vertical impact point y_0 can be calculated from the energies E_U and E_D

$$E_D = E_V \int_{-\infty}^{0} f(y - y_0) dy \tag{10}$$

$$E_U = E_V \int_{0}^{\infty} f(y - y_0) dy , \tag{11}$$

with $E_V = E_U + E_D$. The normalization

$$\int_{-\infty}^{\infty} f(y, y_0) dy = 1 \tag{12}$$

reduces the number of free parameters

$$\frac{P_1}{P_2} + \frac{P_4}{P_3} = \frac{1}{2} , \tag{13}$$

so that the following expression for the energy asymmetry η_V as a function of the vertical position y_0 of the electron is obtained:

$$\eta_V(y_0) = \frac{|y_0|}{y_0} \left[1 - e^{-P_3|y_0|} + \frac{2P_1}{P_2} (e^{-P_3|y_0|} - e^{-P_2|y_0|}) \right] . \tag{14}$$

The vertical position resolution σ_y is expected to scale as $1/\sqrt{E}$ and is approximately a linear function of the vertical position with respect to the split between the upper and lower halves.

3.2 The Silicon Detector

The silicon detector is a position sensitive microstrip detector consisting basically of a small sized prototype of the radiation hard ATLAS Silicon Microstrip detector [11] and of the APV25 Amplifier/Multiplexer Readout chip [12]. The silicon detector size is 1*1 cm^2, of which 0.8*0.8 cm^2 is allocated for the 100 readout strips; the pitch is 8 0μm. The APV25 Amplifier/Multiplexer Readout Chip, is a 128 readout channel analogue pipeline (192 element deep) chip ($\sim$ 1*1 cm^2). In figure 10, the drawing of the silicon detector front-end electronics board, containing the silicon microstrip detector and the APV25 is shown. The various silicon detector components and the electronics that where necessary

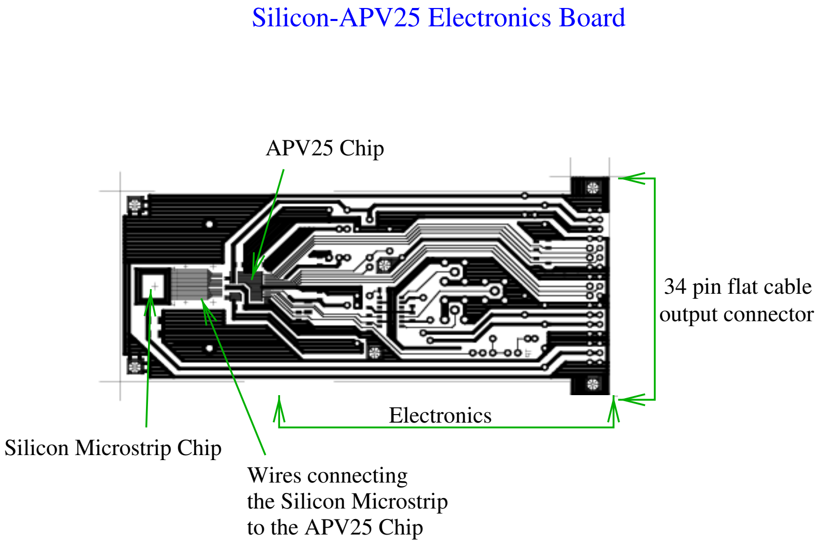

Figure 10: *Silicon-APV25 detector electronics board.*

for the silicon detector operation in the testbeam setup are listed below:

- The ATLAS Silicon Microstrip: 1*1 cm^2, 100 strips, pitch 80 μm, single sided, bias voltage $\sim$ -100 V;
- The APV25 Amplifier/Multiplexer Readout Chip: developed for CMS; $\sim$ 1*1 cm^2, 128 channel analogue pipeline (192 deep) chip. The sampling rate was 40 MHz while the data readout rate was 20 MHz;
- The Silicon-APV25 detector electronics board: 13*5 cm^2 containing the Silicon and APV25 chips, see figure 10;

- The Interface board: Interface board between the Silicon-APV25 electronics board and the VME modules;
- The VME Crate which contains: the FIC 8234 Processor [13]; the I2C [14] module working as a control interface using the I2C standard to set and check the APV25 configuration; the flash ADC [15] SIROCO2-12bit, 20 MHz (CAEN mod. V686,SDR FLASH); the SEQSI [16] -provides control signals for driving the APV25; various boards (Power Supply Module +/-12 V and +/-5 V, Adaptor Board, Miniboard);
- NIM Crate: housing the trigger electronics;
- Bias Voltage box: voltage supply between 0 to -120 V.

3.2.1 Setup in the Test Beam

The silicon detector was mounted together with the 2 other detectors (calorimeter and fiber detector) on a support plate. All 3 detectors where enclosed in a large aluminum light-tight box, and the support plate was fixed to a movable table in the testbeam area T22. All Silicon electronics (NIM trigger electronics and VME electronics) were placed in a rack in T22 at about 3 m from the polarimeter detector. Figure 11 shows the the schematic layout for the silicon detector setup. The box labeled Silicon Detector in the scheme represents the Silicon-APV25 electronics board (figure 10) and the interface board. These are contained within the large aluminum light-tight polarimeter box. A patch panel in the polarimeter box side is used to connect the Silicon Detector to the VME modules (I2C,ADC,SEQSI), the voltage bias, and the power supply +/-12V, in the rack. The silicon microstrip chip is kept at -100V bias. The VME crate and modules are controlled by a FIC 8234 Processor running the OS9 operating system. The APV25 is controlled and set through the I2C module.

The SEQSI is a pulse generator (40 MHz clock) which provides control signals for driving the APV25: a Reset signal -resets the APV25 chip; a Trigger signal -sent to readout the APV25, and a Clock signal - the 40 MHz clock required for the APV25 operation. The SEQSI is designed to respond to random external triggers. The SEQSI generates a sequence, which loops back to the start of the sequence $loopstart$ each time the end of the sequence $loopend$ is reached i.e. a continuous looping sequence. The sequence is incremented by one sequence unit for each clock cycle. Near the beginning of the sequence a Reset signal is sent to the APV25, then the SEQSI waits for a random external trigger to arrive, if not it loops back at the beginning of the sequence $loopstart$, this happens when the sequence end $loopend$ is reached. If an external trigger arrives, then the SEQSI sequence jumps to a point beyond the end of the looping sequence $loopend + jump$, in this case the sequence till continues until $seqendexttrig$ is reached. In this extended part

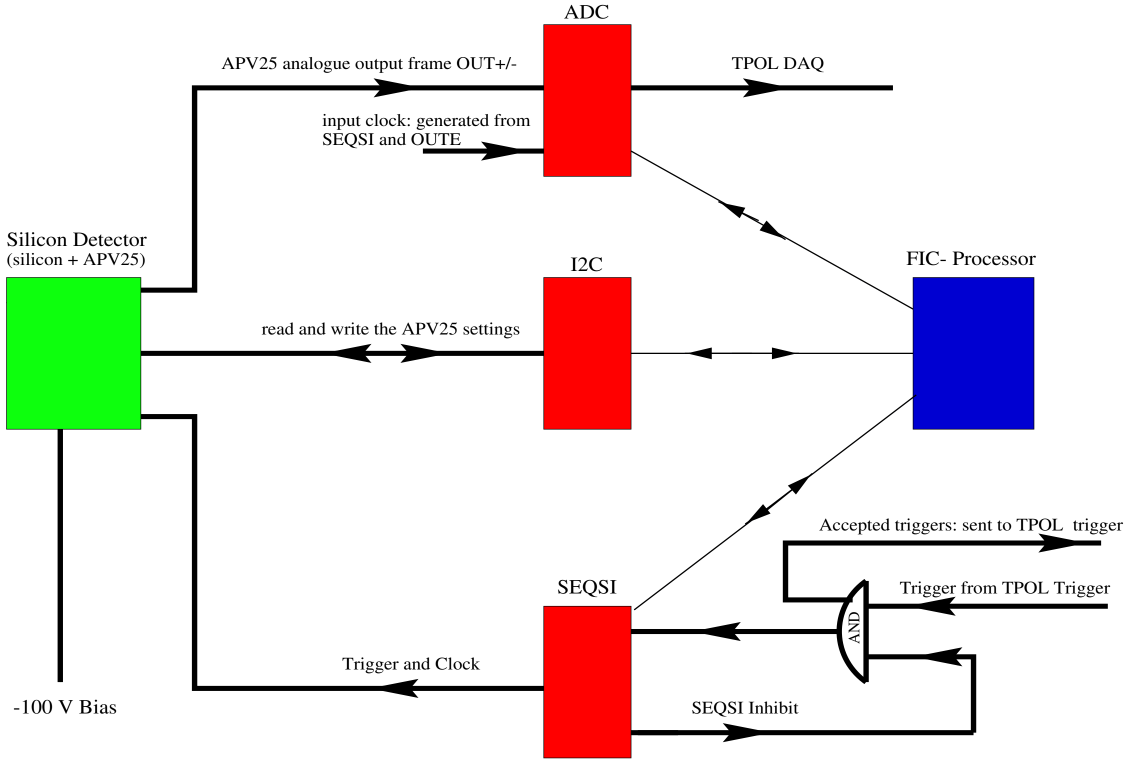

Figure 11: *Simplified scheme for the silicon detector setup in the testbeam.*

of the sequence, between *loopend* + *jump* and *seqendexttrig*, a trigger signal is sent to the APV25 and then sufficient time is given for the APV25 to be readout and to send the analogue data to the ADC. When *seqendexttrig* is reached the SEQSI loops back to the beginning of the sequence *loopstart* , starting the sequence loop all over again.

The trigger signal sent by the SEQSI to the APV25 for readout must have the correct clock sequence timing to match the latency of the silicon detector system. The trigger signal is sent by the SEQSI to the APV25 at a specified clock number value in the SEQSI sequence, to readout the APV25 pipeline column containing the silicon chip signals generated by a hit in the silicon. The correct sequence clock number value is obtained by taking several data runs with different sequence clock number values, but containing the same number of events. All signals in each given run are summed up. The run with the highest total sum signal value is the one with the correct clock sequence number. This clock sequence number is used in the SEQSI sequence, to send correctly timed trigger signals to the APV25 for readout, for all testbeam runs.

The random external trigger signal is sent to the SEQSI from the polarimeter trigger electronics (TPOL trigger). In the NIM crate a coincidence between the TPOL trigger signal and the SEQSI Inhibit signal is made. The TPOL trigger is allowed to reach the SEQSI whenever the SEQSI Inhibit is off. The SEQSI Inhibit is on when the SEQSI is resetting the APV25 (beginning part of the sequence) and when the APV25 is readout (between $loopend + jump$ and $seqendexttrig$). One of the outputs from this coincidence is sent to the TPOL trigger electronics, to check how many of the sent TPOL triggers are accepted by the SEQSI i.e. the silicon detector. When acquiring a data run there are two triggers sent to the SEQSI: a physics trigger that is used to collect physics data and a pedestal trigger which sends a trigger to the silicon randomly whenever there is no physics trigger. The pedestal trigger is used to collect pedestal events. So in a given data run there are both physics events and pedestal events.

The SEQSI has a $40MHz$ clock which corresponds to a $25ns$ clock cycle. When the external random trigger signal is inputted into the SEQSI, it has to synchronized with the SEQSI system clock, which can be done only within one clock cycle. This creates a $25ns$ jitter, in the SEQSI trigger signal sent to the APV25 for readout, between different events. The APV25 processed pulse shapes corresponding to the silicon detector hits, which are continuously sampled every $25ns$, are wide enough to limit the effect of this jitter. The digitized signal value varies between 5% - 10%, due to this jitter effect.

The APV25 readout is at $20MHz$, its analogue output signal is sent to the flash ADC for digitizing. The analogue output signal is a differential current output consisting of two signals equal but opposite OUT+,OUT-. The ADC begins to digitize whenever an input clock train ($20MHz$) is fed to it and stops when the clock train has ended. So to digitize the APV25 analogue output frame, the ADC requires an input clock train to arrive simultaneously and to be in phase with the APV25 analogue output, and to be long enough to digitize the complete APV25 analogue output frame. The input clock train is at $20MHz$ and slightly longer than the APV25 analogue output. The clock train is generated by making a NIM coincidence between the $20MHz$ clock obtained from the SEQSI and a slightly lengthened OUTE signal generated by the APV25. NIM electronics are used to lengthen the OUTE signal. The OUTE (OUTE=output enable) signal is a gate that is generated whenever the APV25 is readout, its length is that of the APV25 analogue output. The SEQSI sequence jumps from the looping sequence to the extended part of the sequence each time an external trigger arrives; to have the same clock phase as before the jump, an electronics miniboard is used to extract from the SEQSI a $20MHz$ continuous clock. During the setting up of the system the relative phase of the input clock train and the APV25 analogue output frame are checked with an oscilloscope, for correct signal digitization. The APV25 has some fixed reference pulses which can be used for synchronization purposes.

The APV25 digitized data are sent to the TPOL DAQ where they will be combined offline for each event with the fiber and calorimeter data. Only after that the ADC has sent all the digitized data for a given event to the TPOL DAQ, can the TPOL trigger send another trigger to the Silicon detector.

3.3 The Fiber Detector

Before the long shutdown of HERA in 2000, the rate of the back-scattered Compton photons and the bremsstrahlung photons was found to be about 100 kHz in total at the TPOL calorimeter. From a Monte Carlo simulation study, the radiation dose at the silicon detector, which will be installed in front of the calorimeter, was estimated to be 1.9 Mrad per year [17]. In order to monitor, calibrate and correct the linearity of the silicon detector, we will install another calibration device, which consists of a scintillating fiber as described below.

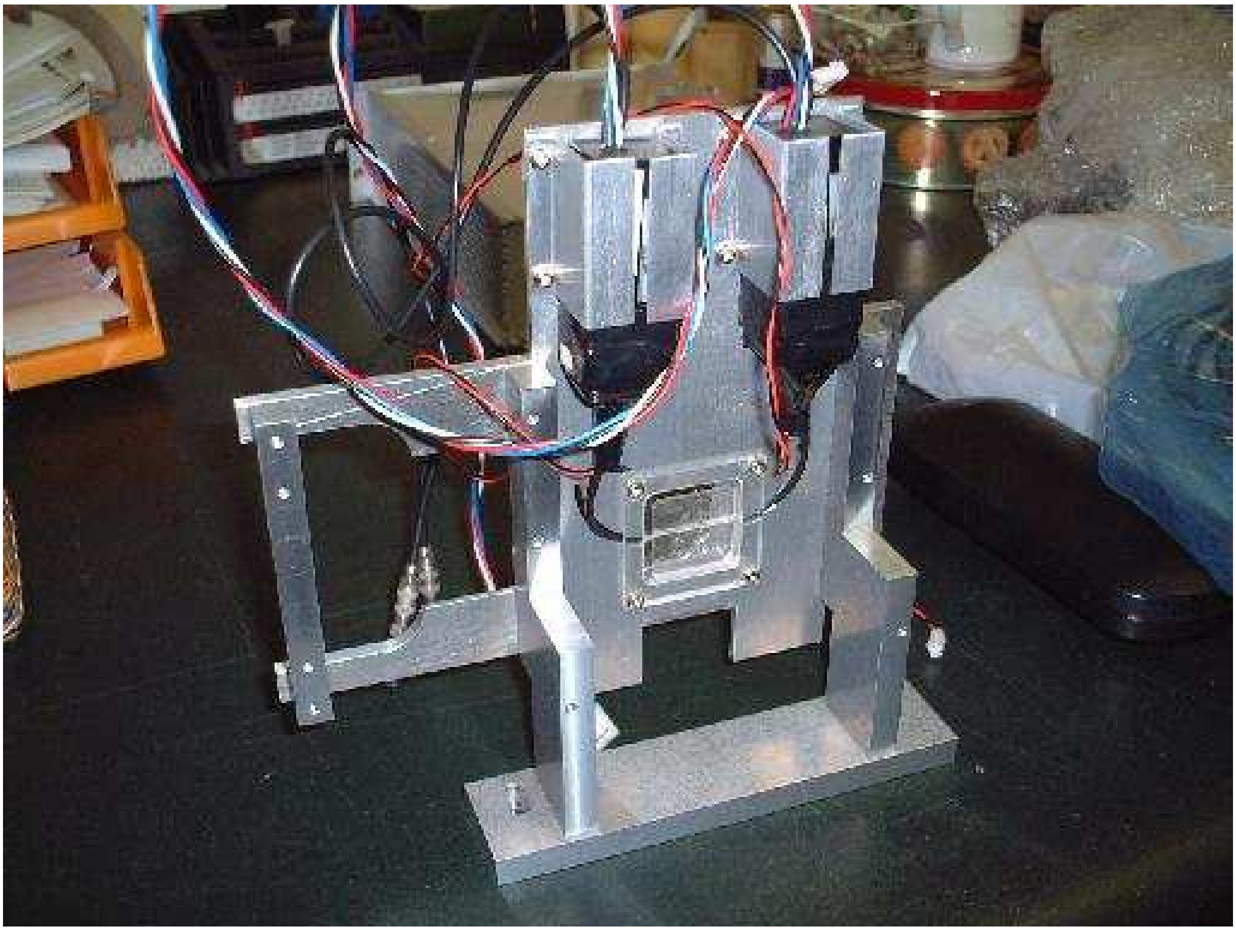

Figure 12: *A photograph of the fiber detector.*

Figure 12 shows a photograph of the fiber detector, which was installed in front of the silicon detector. The detector components are listed below:

- A double cladded scintillating fiber (KURARAY, SCSF-81M) is put horizontally in a groove on the plastic window. The length and diameter of the fiber is 20 mm and 1 mm, respectively.
- The signals from both ends of the scintillating fiber are transported via double claded clear fibers (Edmund Scientific Japan Co., Ltd.), which are bent upwards to the photosensor modules.
- The photosensor modules (HAMAMATSU, H6780) include a compact photomultiplier (PMT) and a power supply. These PMTs feature low voltage operation (from +11.5 to 15.5 V). The gains of PMTs are adjusted by a control voltage (from 0 to 1.0 V). During this test-beam, PMTs were operated with the control voltage set to 0.87 V.
- As seen in Fig. 12, the above components are supported by an aluminum plate.
- The aluminum plate is mounted on a metal ring. The height of the fiber detector is adjusted by replacing different diameters of the metal rings.

The power supply and control voltage for the PMTs were controlled by a VME DAC module (Advme 1614, Advanet Inc.) [18]. The pulse height of the output signals from the PMTs was typically 20 mV. After amplifying them by a factor of 10 using a NIM module (4ch PM AMP N-TM 230, Technoland Co.), we made a coincidence of these PMT signals to supply a trigger signal. This is referred to as 'Fiber Trigger' in this note.

4 Test Beam Results

In this section the analysis and results of the test beam data will be presented and discussed: calorimeter, silicon detector, fiber detector and the test beam telescope.

4.1 Data Analysis and Results from the Calorimeter

The spare calorimeter is an exact copy of the TPOL calorimeter [6] and was tested with the CERN 8 GeV - 50 GeV electron beam in 1997 [8]. We will compare the measurements made in the DESY test-beam with electron energy inside of 1 GeV - 6 GeV, mainly with those from the CERN test-beam at the lowest energy of 8 GeV.

Prior to data taking the calorimeter was calibrated using 6 GeV electrons to equalize single channel responses by adjusting PMT voltages as described in [6] and [8]. Residual deviations of the calibration constants were corrected by software using fine gain adjustments. Results of a beam energy scan in the range of 1 GeV-6 GeV are shown in fig. 13. One can see the main contribution to uncertainty of data points comes from a spread of the beam energy which is estimated to be 5%-10% depending on the first collimator opening [19]. The best χ^2 fit to linearity response was achieved for the beam energy spread 5% with only one parameter. Adding more parameters (to describe an ADC pedestal shift or nonlinearity) or increasing the beam energy spread above 5% lead to unacceptably small χ^2 values which indicates the correct pedestal subtraction and negligible nonlinearity of the detector. This was also observed at CERN with different electronics [8]. A two parameter conventional fit [8] was applied for the description of the calorimeter energy resolution fig. 13(right plots). The observed resolution $\sigma_E = 29\% - 30\%$ to be compared to $\sigma_E = 23\% - 24\%$ which was obtained at CERN. The decrease in the resolution is accounted for by the additional material in front of calorimeter which is responsible for the 25% degradation of σ_E.

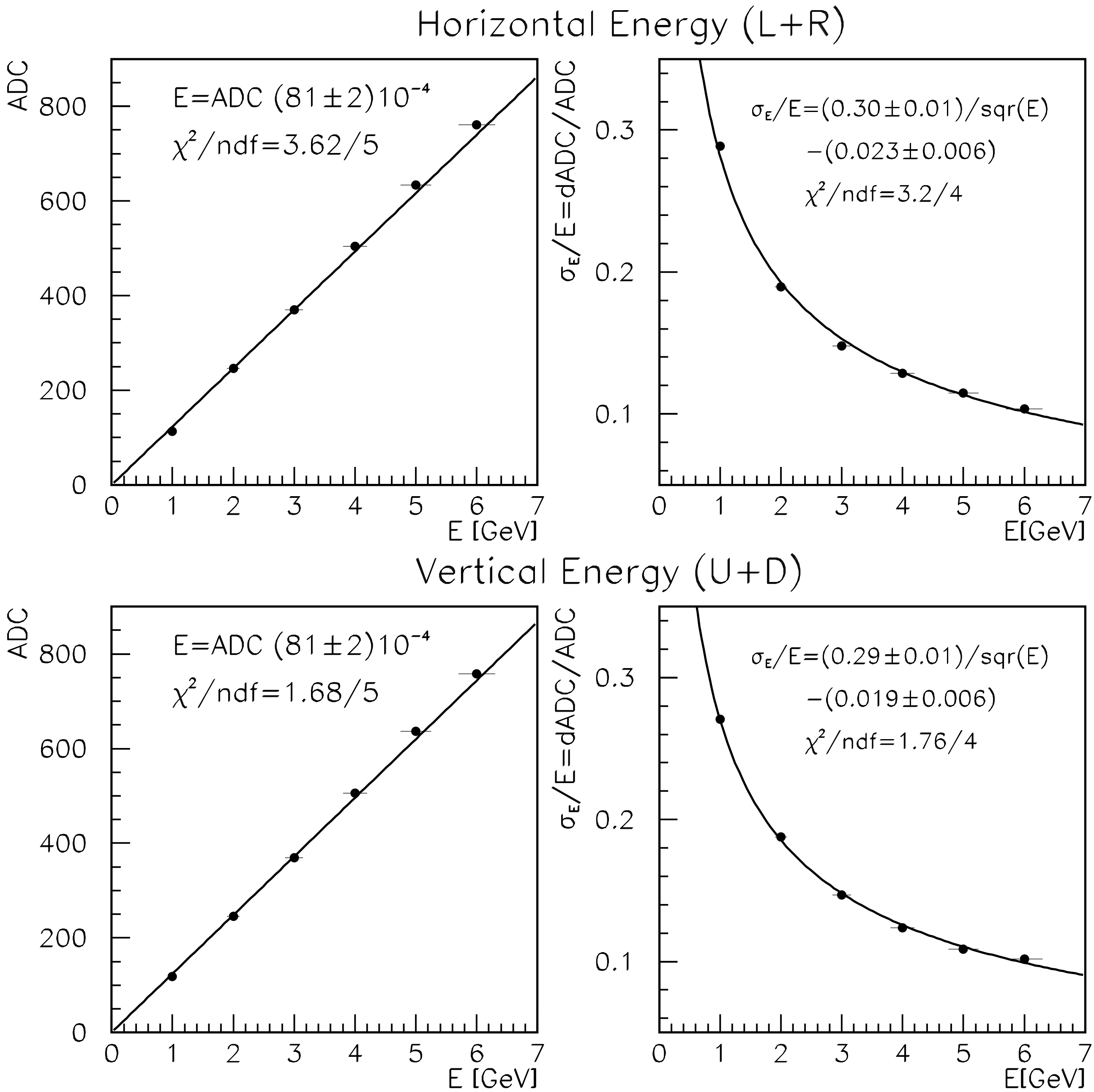

Figure 13: *Calorimeter response linearity (left column) and energy resolution (right column) for sum of left and right (upper row), up and down (lower row) channels.*

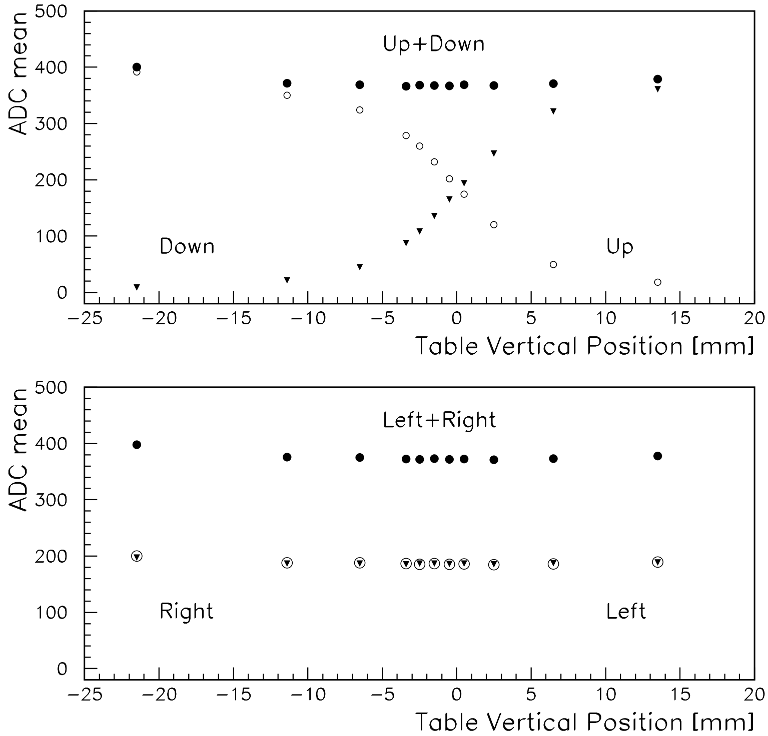

Figure 14: *Calorimeter average signals from Up, Down, Left, Right channels versus beam vertical position*

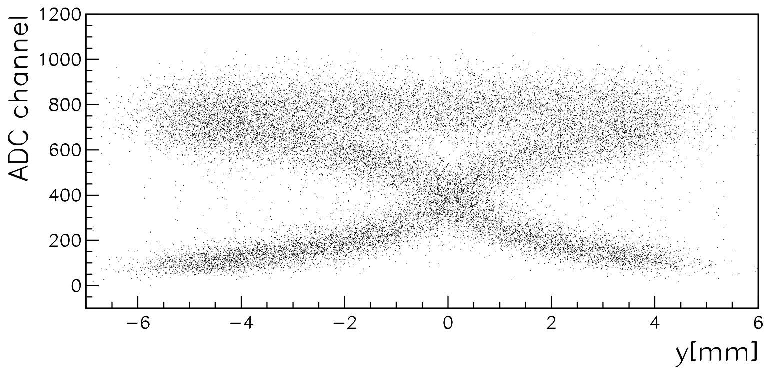

Figure 15: *Calorimeter Up and Down channels ADC signals as a function of the vertical impact point y.*

The calorimeter table vertical scan, performed at electron beam energy 3 GeV (fig. 14), shows an excellent spatial uniformity of the detector. The same is seen for a smaller vertical spatial range when the calorimeter is centered on a 6 GeV beam and hit positions are provided by the Telescope (fig. 15). At the CERN test beam a 2%-3% energy loss due to shower (light) absorption by the calorimeter middle plane was observed when particles hit the calorimeter vertical center. This dip is highly reduced and hardly observable at the DESY test setup most likely due to smearing by the same preshower.

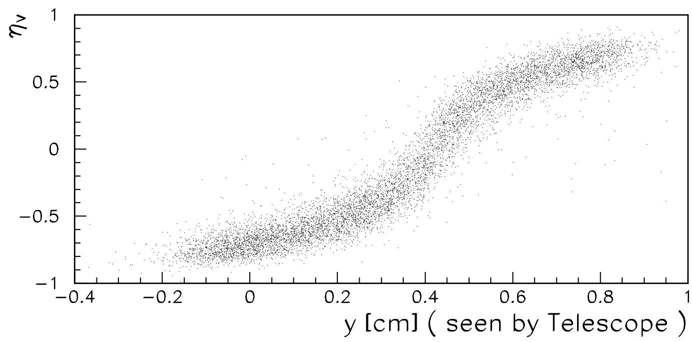

Figure 16: *Vertical energy asymmetry* $\eta_V = (E_U - E_D)/(E_U + E_D)$ *as a function of the vertical impact point* y *for a beam energy of 6 GeV.*

A data sample with removed preshower at the electron beam energy 6 GeV is utilized to derive the calorimeter position response function $\eta - y$ transformation (fig. 16).

The η distributions in 33 y slices were approximated by Gaussians and Gaussian means are fitted using a 3 parameter function as displayed in fig. 17. As already seen from fig. 16- the η distribution inside a y slice deviates from Gaussian more and more as y approaches the calorimeter center. This was the main source of difficulty to describe correctly the $\eta - y$ distributions for the spare and the original calorimeter test beam data using only 3 parameters and was often compensated by adding more parameters. While this is true also for our data, the fit χ^2 and residuals show a good approximation using 3 parameters even for no-preshower data. The flattening of the $\eta - y$ distribution caused by the preshower makes Gaussian approximations more valid.

The fitted $\eta - y$ response function allows to estimate the detector position resolution σ_y which is proportional to the width of η distribution (fig. 18). While lower beam energy compared to CERN 8 GeV are expected to worsen σ_y, the observed resolutions at different y are better by as much as factor of 2 compared to those observed at CERN. A possible explanation could be an underestimation of the multiple scattering in the CERN test beam setup.

To summarize, the DESY test beam results show very good linearity and spatial uniformity of the calorimeter, energy resolution $\sigma_E = 29\%$, spatial resolution $\sigma_y = 0.4$ mm at 6 GeV $y = 0$.

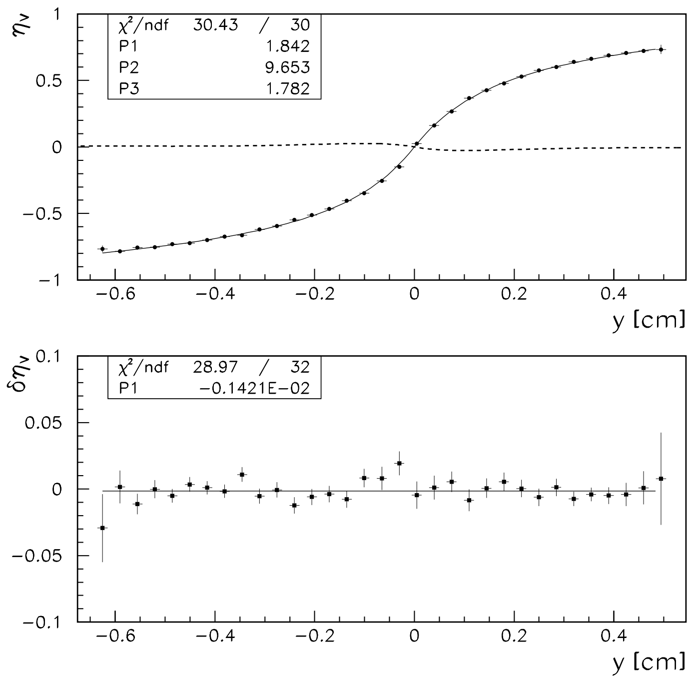

Figure 17: *Vertical energy asymmetry* $\eta_V = (E_U - E_D)/(E_U + E_D)$ *as a function of the vertical impact point y (telescope) for a beam energy of 6 GeV. Also shown a fit to the parameterization* $\eta_V(y) = \frac{|y|}{y}\left[1 - e^{-P_3|y|} + \frac{2P_1}{P_2}(e^{-P_3|y|} - e^{-P_2|y|})\right]$ *and fit residuals (lower plot) fitted by a constant. The dotted line on the upper plot is the difference between the fit and CERN test beam 8 GeV parameterization.*

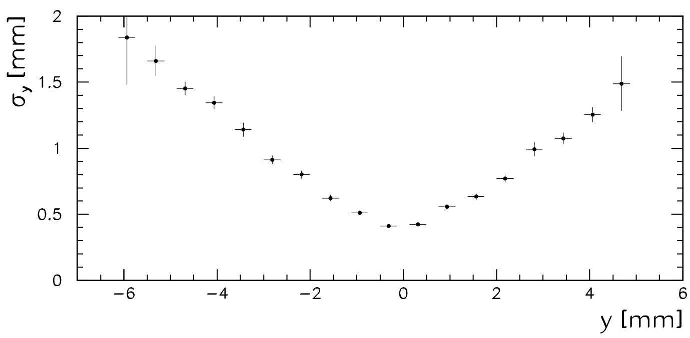

Figure 18: *Vertical position resolution* σ_y *as a function of the vertical impact point y.*

4.2 Data Analysis and Results from the Silicon Detector

Results from the silicon detector will be presented in this section. Two data run types have been used for this analysis: preshower data runs- a lead preshower (5.6 mm thick equivalent to 1 X_0) is placed in front of the silicon detector; no-preshower data runs- the preshower and some other material was removed to reduce the total amount of material in front of the silicon, see scheme in figure 7.

The main data sets displayed in the plots, for the silicon microstrip detector studies are:

- preshower runs: run: 273, trigger: ungated, Beam Energy: 6 GeV, events: $\sim$200 k, bias: -100 V, table position y=65.5 mm, x=-132.2 mm.
- no-preshower runs:396,397,400,403, trigger: ungated, Beam Energy: 6 GeV, events: $\sim$200 k, bias: -100 V, table position y=67.5 mm, x=-132.2 mm.
- bias voltage scan: run 261-265, trigger: ungated, Beam Energy: 3 GeV, events: $\sim$50 k, bias:-20 to -100 V, table position y=67.5 mm, x=-132.2 mm, preshower material in front of silicon.

The preshower and no-preshower runs differ by 2 mm in the vertical polarimeter position. Other data runs have been used to cross-check the results.

The pedestal and noise is calculated from the pedestal data found in each run for each channel; each run has both pedestal and physics data, see section 2.3. The common mode baseline shift is calculated for each event. The signal for a given channel is obtained by subtracting the pedestal and common mode from the raw ADC value; a threshold cut is applied to define the lower limit for the signal value. Clusters are built from a group of adjacent strips satisfying a given set of requirements. A detailed description of the analysis is given in the following paragraphs. The following topics will be discussed and analyzed:

- strip studies: pedestals, noise, signals;
- cluster studies;
- bias voltage scan;
- eta-y transformation.

4.2.1 The Silicon Raw Data Structure

For each event, the silicon raw data consists of 150 ADC numbers: the first 128 numbers correspond the 128 APV25 channels (APV25 readout output frame), the 129nth is the APV25 readout output end-marker signal, and the last 21 numbers correspond to the typical baseline values between the successive APV25 readout output frames. Figure 19 (left plots), shows an event display for typical raw data events. The channels displayed follow the APV25 multiplexer readout channel order (called APV25 channel order) , which is different from the physical silicon strip channel ordering (called strip order). The silicon chip has only 100 strips, which are connected to 100 of the 128 APV25 channels. In the two right plots the corresponding event is displayed according to the physical channel order (strip order). Only the 100 silicon strip-channels that are bonded to the APV25 are displayed. In the physical channel ordering only physical APV25 channels (strips) 14 to 113 inclusive, are bonded to the silicon. Data taken without preshower (run 397) has fewer hit strips than preshower data (run 273), as would be expected. In the data analysis only the 100 bonded strips will be considered for signal and cluster finding, the other channels are used for cross checking.

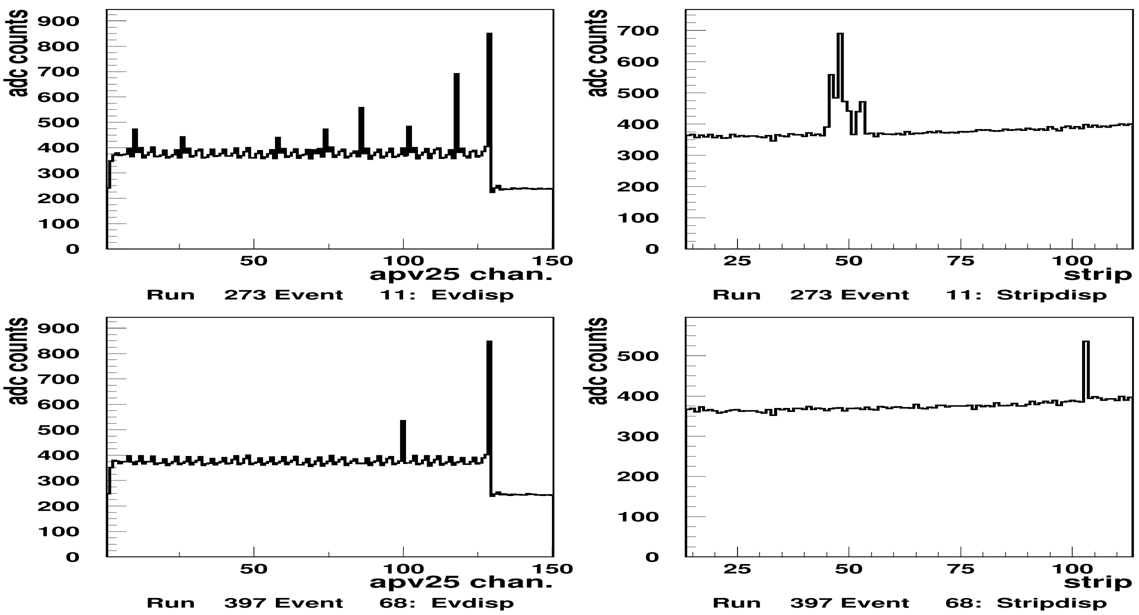

Figure 19: *Event display according to the APV25 channel order (left plots) and strip channel order (right plots). Run 273 preshower data, run 397 no-preshower data. The peaks indicate the hit channels. The highest peak on the right is the end-marker (present only in the left plots). In the strip order event display only the100 connected strips are displayed, while in the APV25 channel order event display all 150 ADC values are displayed.*

4.2.2 Pedestals and Raw Noise

The pedestal values are obtained from the pedestal events present throughout the data run (pedestal trigger); 10-15% of the events in a data run are pedestal events. The pedestal value for a given channel is obtained by averaging over all pedestal events in the data run corresponding to the channel. The raw noise of a given channel is defined as the RMS of the pedestal distribution for the channel. Figure 20 displays the mean pedestal and raw noise values of the connected silicon strips, for 4 different runs taken some days apart during the test beam. The mean values vary little from run to run and therefore from one day to another; showing that the pedestal and noise are quite stable during the test-beam running. The mean pedestal value increases with the strip number; this a characteristic of the APV25 readout chip. The mean raw noise value is between 6 and 8 ADC counts for most channels except for some noisy channels. The abrupt change in the mean raw noise value around strip 65 is probably due to some physical characteristic of the silicon-APV25 chips, which is not understood.

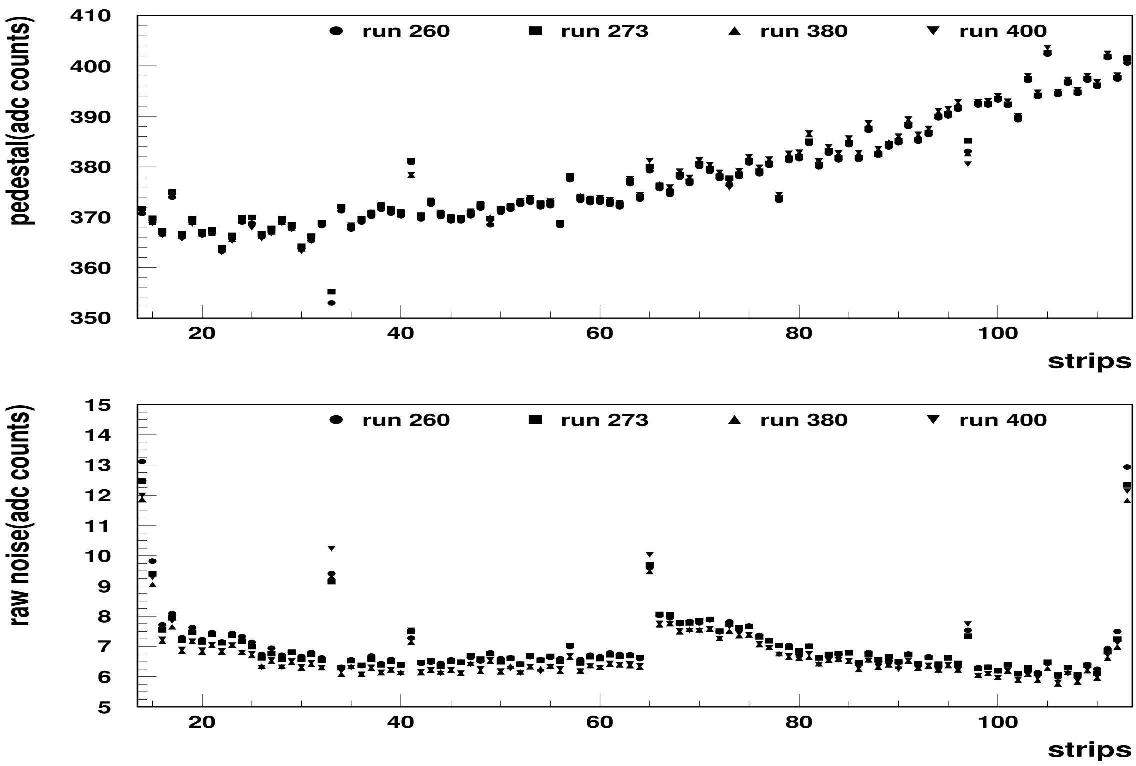

Figure 20: *The mean pedestal and raw noise values of the connected silicon strips, for 4 different runs.*

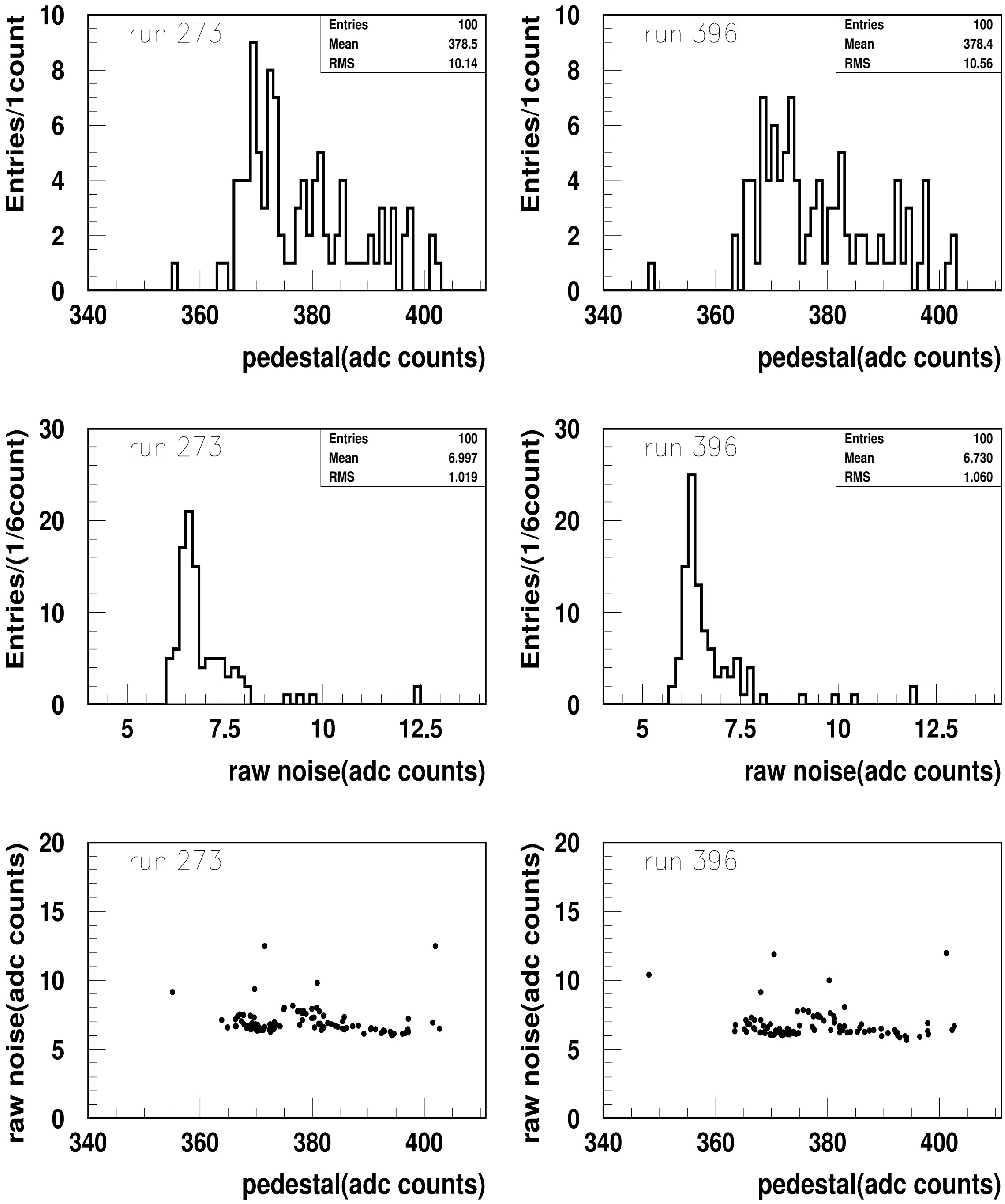

Figure 21: *The mean pedestal, raw noise and raw noise versus pedestal distributions for the 100 silicon channels; for run 273(preshower run) and runs 396,397,400,403 combined (no preshower run).The two data sets have approximately the same number of events. In the right plots only the first run number of the data set (396,397,400,403) is indicated.*

Figure 21 shows the pedestal, raw noise and raw noise versus pedestal, distributions for two sets of runs. The mean value and RMS of the distributions varies little from one another, and the raw noise versus pedestal distribution is basically flat in both cases. Figure 22 shows the mean pedestal values and the raw noise values calculated for all 128 APV25 channels, also for the 28 unconnected ones. The data is taken from the two data sets: preshower run 273, and no-preshower runs 396,397,400,403. The unconnected strips have a lower raw noise value and the mean pedestal value is flat in the unconnected strips region.

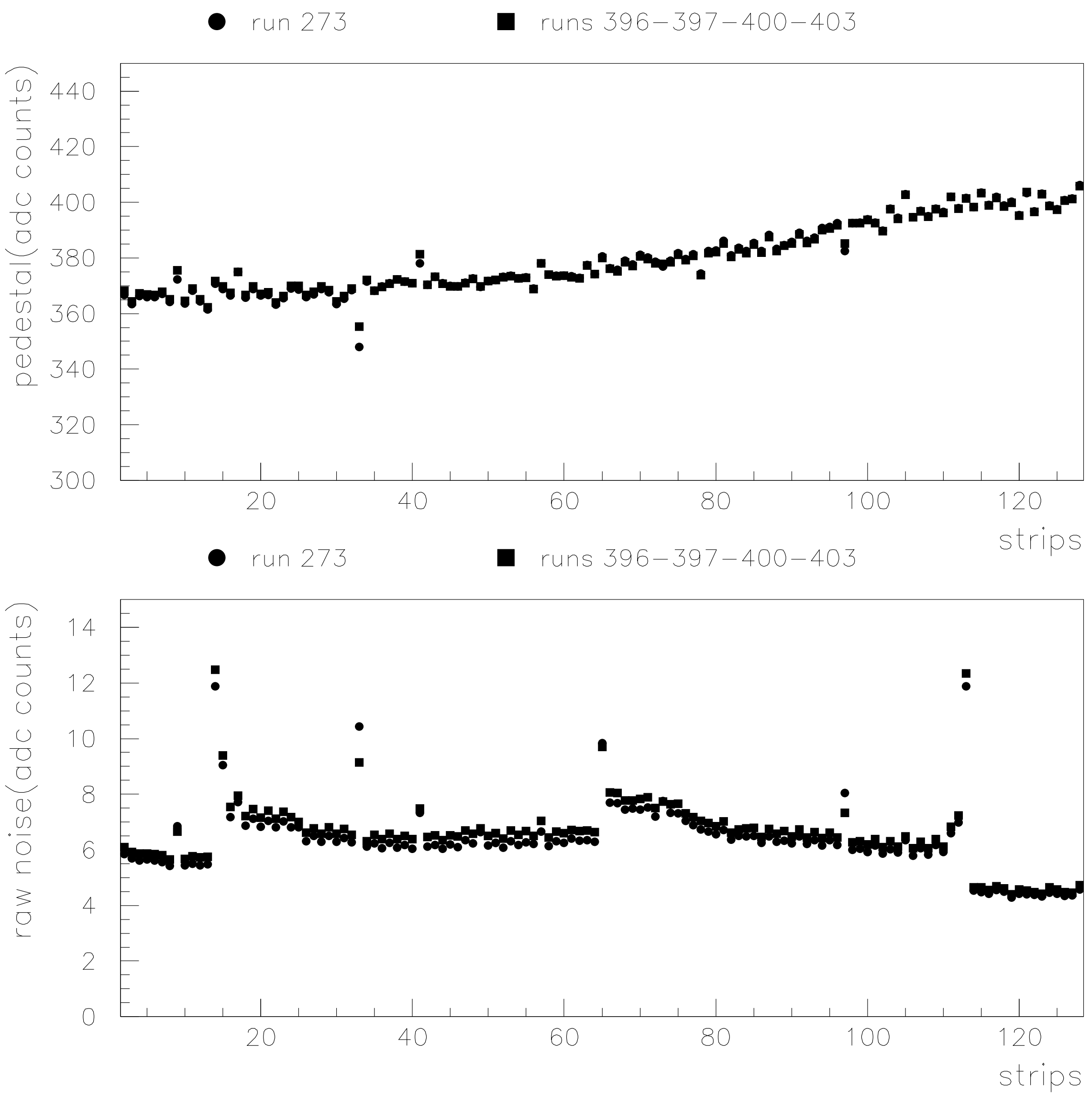

Figure 22: *The mean pedestal value and the raw noise values calculated for all 128 APV25 channels, for the two run datasets. The APV25 channels are displayed in strip order.*

4.2.3 Common Mode Correction

A common mode subtraction (symbolized by CM) is applied to correct for the baseline shift of the whole APV25 analogue output frame. The baseline fluctuation is mainly due to power supply variations and noise pickup. For the CM calculation only the 100 connected strips are considered. The CM is calculated by finding for each event the average raw ADC value of all strips that do not have a signal, but are within the noise limit. All strips that have a raw ADC count value within 3 RMS of the mean pedestal value are considered in the CM calculation. Figure 23 displays the CM for 4 different runs. The CM distribution is not a good Gaussian; it is centered around zero and has an RMS of 6-6.5 ADC counts. The CM distribution is not necessarily expected to be Gaussian because there might be some CM systematics, which result in a non-Gaussian shape.

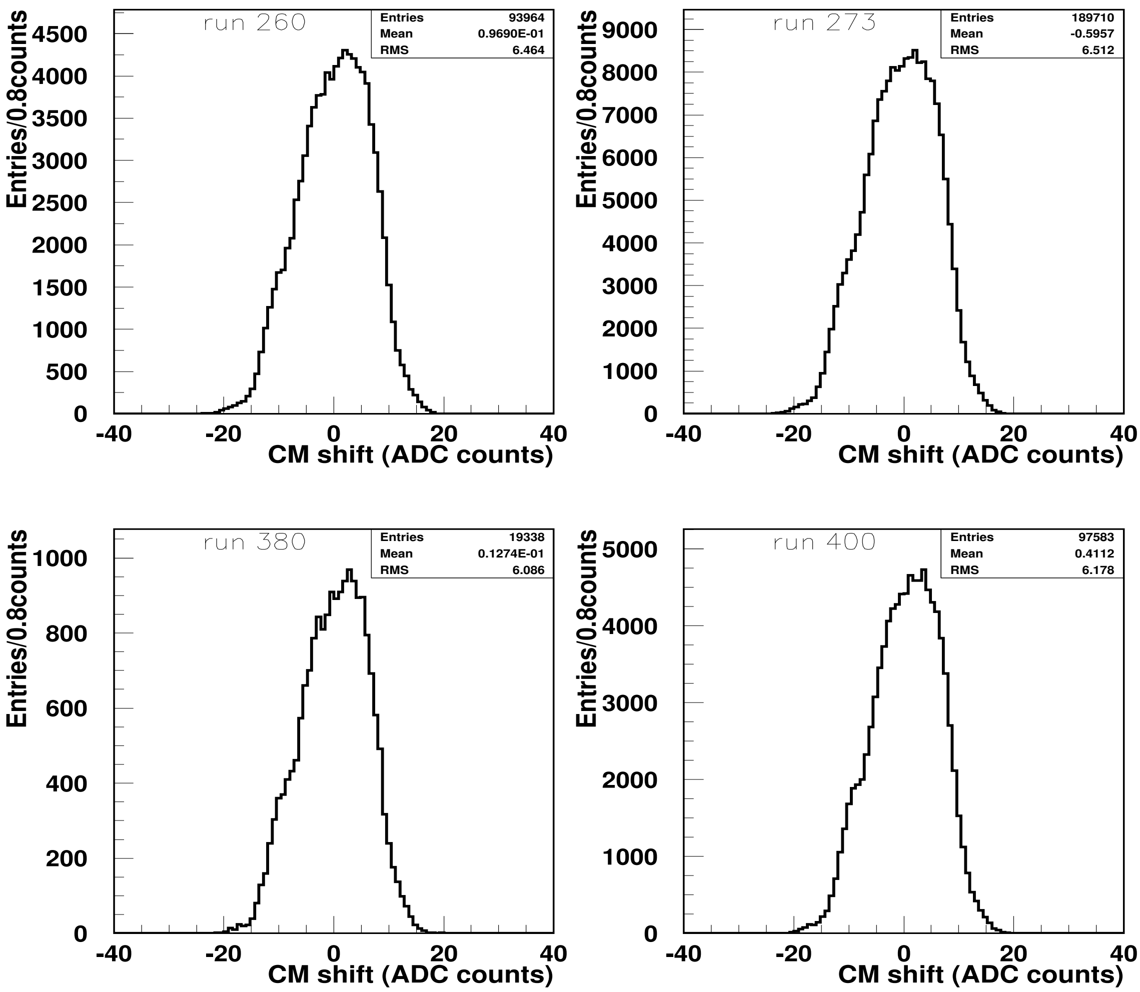

Figure 23: *The common mode baseline shift (CM) for 4 different runs. The entries indicate the number of events in the run.*

4.2.4 Signals

We first present and define some terminology regarding the silicon signals, that will be used throughout this section.

Strip Pulse Height PH_i**:** For each data event in a run the pulse height PH_i for strip i (i=14,113 for the connected strips) is calculated from the following equation:

$$PH_i = ADC_i - PED_i - CM \tag{15}$$

where:
ADC_i = raw ADC counts in strip i;
PED_i = mean pedestal value in ADC counts, averaged over all pedestal events in the run, for strip i;
CM = Common Mode baseline shift correction for the event.

Strip Noise Definition N_i**:** The corrected noise of a given strip i.e. strip noise N_i, is calculated as the RMS of PH_i for pedestal events i.e. the RMS of the strip i pedestal pulse height distribution:

$$N_i = RMS(PH_i) \tag{16}$$

where $PH_i = ADC_i - PED_i - CM$ for pedestal events.
The strip noise is referred to as the corrected noise for a given strip because the CM shift is subtracted from the raw ADC counts, when calculating it.

Signal Definition S_i**:** For a given event, strip i is considered to have a signal S_i, if the PH_i value is greater the three times the RMS of the strip noise N_i:

$$S_i = PH_i > 3 * N_i. \tag{17}$$

First of all the typical strip pulse height distributions PH, for pedestal and physics data, and the strip noise will be shown.

The two top plots of figure 24 display the strip noise (or corrected noise, as defined previously) for the 100 silicon strips, which varies between 2 to 3 ADC counts, except for some noisier channels.

The two middle plots display the PH distribution for pedestal events for strip 50, which is well fitted by a Gaussian distribution; similar values are obtained for the RMS and sigma of the PH distribution. The RMS of the distribution is used to calculate the noise because it is simpler to extract. For simplicity strip 50 has been chosen to be displayed here, but it is representative of all the other silicon strips.

The lowest plots display the PH distribution for signal events i.e. data triggered by the physics trigger. Fitting with a Gaussian the PH region around zero (hatched area), which corresponds to events which have no signal in the strip (pedestal region), one obtains a sigma value very near to the one obtained from the pure pedestal PH distribution. The no-preshower run (runs 396,397,400,403) has a more pronounced peak when compared to the preshower (run 273) run. This is due to the fact that with no preshower most events have a cluster consisting of 1-2 strips (1 particle hit), instead with the preshower the clusters are wider and more numerous (multi-particle hit). The charge is shared differently between strips, depending on whether it is a single or multi particle hit. In a single particle hit the charge is seen by only one, at most two strips, thus giving a more peaked PH distribution.

In the two lowest plots, the pedestal peak contains many more events then the rest of the PH distribution for two reasons. First, a hit in the silicon will give rise to signals only in a few strips, 1-2 for no-preshower runs and several strips for preshower runs, so that for a given strip only few percent of its physics data PH distribution events will correspond to a hit (i.e. signal in the strip), most events will fall in the pedestal region, because some other strips are hit. Second, not all physics triggers give rise to an event in the silicon, because also if the scintillation trigger counters are triggered, the passing particle might not actually hit the small sized silicon microstrip chip. This is because the test beam and the scintillation trigger counters are wider then the silicon microstrip. Such triggered event will give rise to a pedestal signal in the silicon.

To calculate the gain for the different silicon strips, single strip clusters are studied, see figure 25. Only the no-preshower data set is considered, because the clusters are smaller then the preshower data set. Again, strip 50 is taken as representative of all other strips.

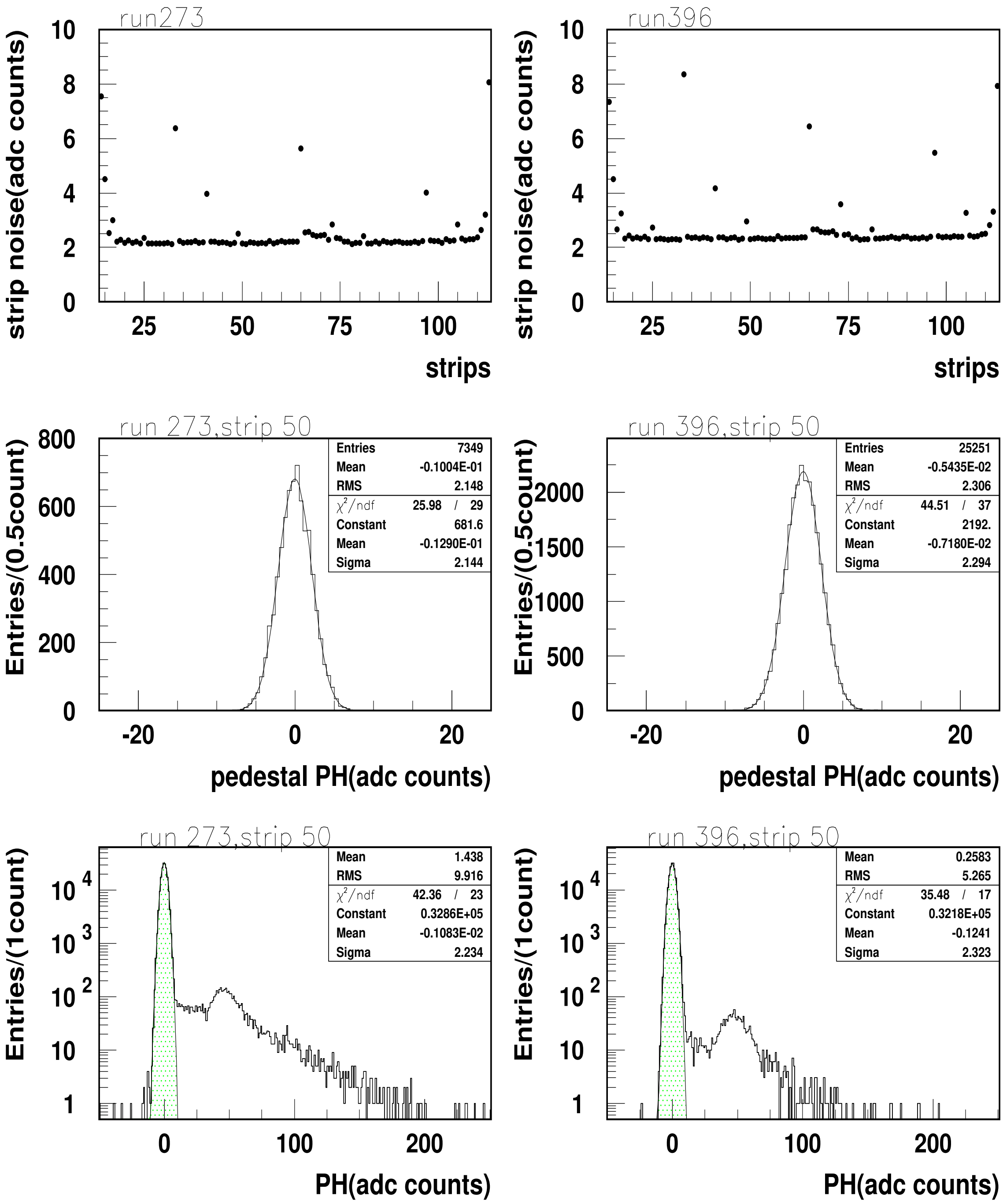

Figure 24: *The strip noise for the 100 connected strips (top), pedestal pulse-height for strip 50 (middle) and signal pulse-height distribution for strip 50, for run 273 preshower, runs 396,397,400,403 no-preshower (only the first run 396 is indicated). In the lowest plots the filled area indicates the Gaussian fit to the pedestal area of the pulse-height distribution.*

Single strip cluster events:
To study the single strip pulse height distributions of signals, single strip cluster events where chosen (NCLUS=1,NSTRIP=1) i.e. there is only one strip in all the silicon that has a signal $S_i = PH_i > 3 * N_i$. Such choice is made to select events where the signal is produced only by one strip. The charge shared between strips is strongly reduced, nearly all of the charge is seen by only one strip- the single strip clusters; see figure 25.

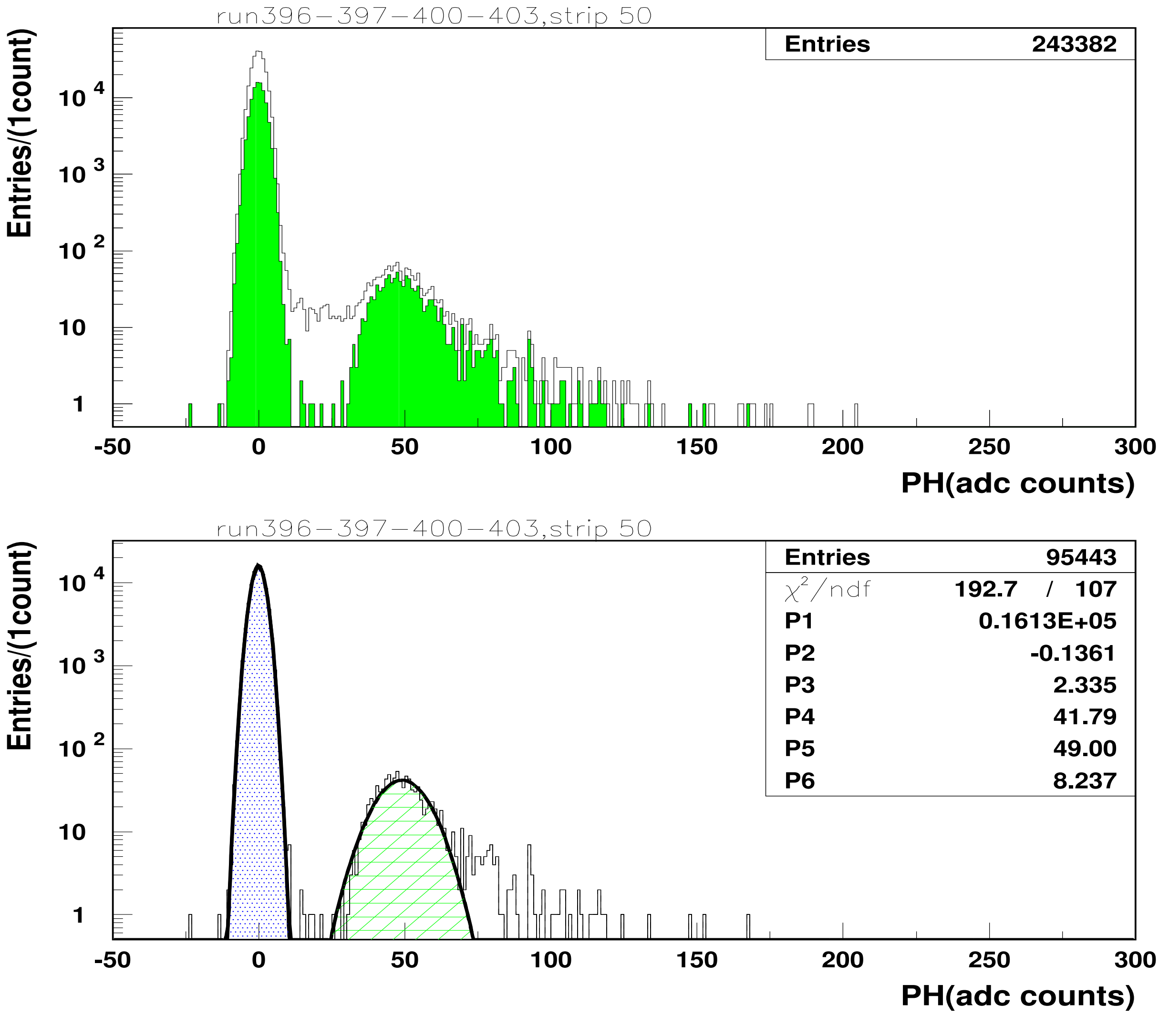

Figure 25: *Pulse height distributions (PH). Top plot, the pulse height distribution for no-preshower runs(396,397,400,403) for strip 50. The superimposed hatched histogram is for single cluster strip events (NCLUS=1,NSTRIP=1). Bottom plot, the same hatched histogram of the top plot for single cluster strip events fitted with two Gaussians. One around zero which is the pedestal area of the distribution; parameter P3 is the sigma value. The other Gaussian fits the strip signal peak; parameter P5 = mean value of the peaked signal distribution.*

Strip Gain:

From these single strip cluster events the strip gain can be obtained. The strip gain is calculated as the average value of the strip's signal pulse height distribution for all single strip cluster events. In figure 25 a comparison is made between the complete pulse height distribution and the single cluster strip pulse height distribution, for strip 50 for no-preshower runs. It is clearly seen that the single cluster strip distribution is more markedly peaked, due to the strongly reduced charge sharing i.e. the charge is seen by only one strip. In the lower plot, a Gaussian is fitted to the pedestal region and another one to the signal peak. The pedestal Gaussian as expected, gives a sigma value similar to the RMS of the pedestal distribution, which is used to calculate the strip noise. Also the mean value of the signal Gaussian is very close to the strip gain value, which for simplicity is calculated as the average strip signal value. The strip gain is in ADC counts, see figure 26 for comparison. The strip gains for all 100 strips is plotted in figure 26. The average strip gain is 48 ADC counts. The strip gains vary between 45 and 52 ADC counts. The signal to noise ratio S/N, is calculated for each strip as the ratio between the strip gain and the strip noise; the average S/N for all the strips is 19. If the noisy strips are excluded, the average S/N $\sim$21. From figures 27 and 28 it can be seen that the the strip signal to noise ratio (S/N) decreases with increasing strip noise, as would be expected; while for the other plots there is no strong correlation.

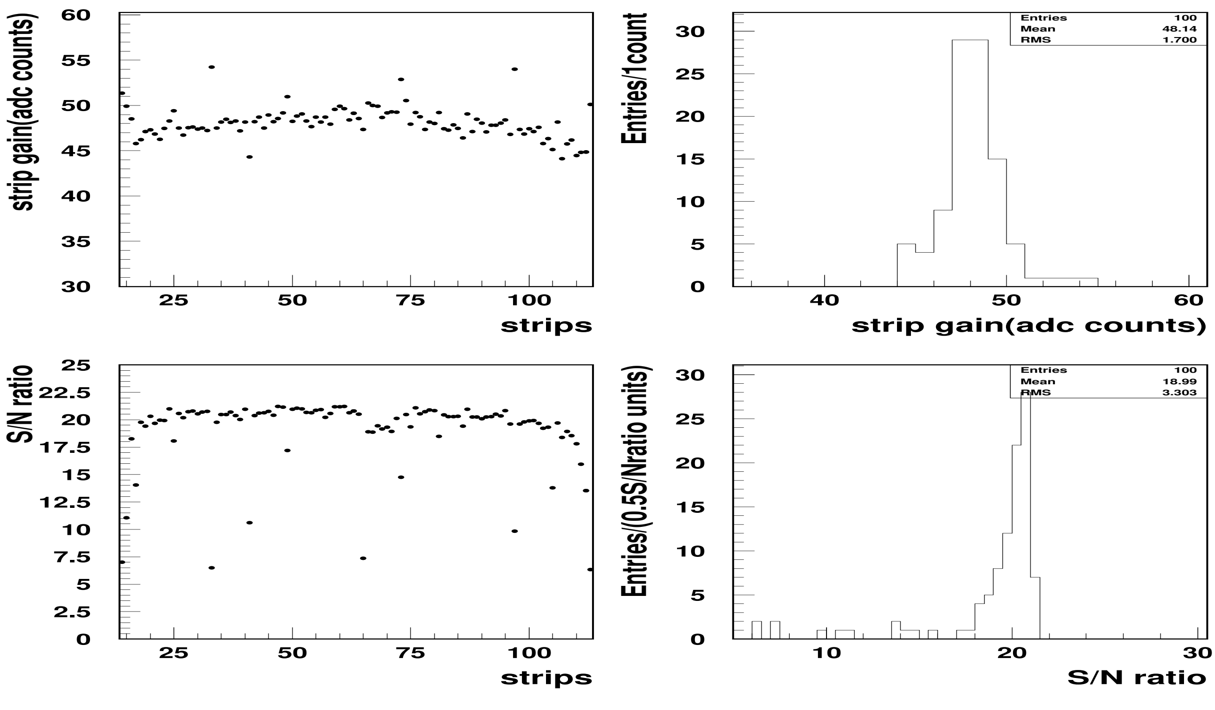

Figure 26: *Top plots, the strip gain in ADC counts versus strip number (left) and the strip gain distribution (right). Bottom plots, strip signal to noise ratio (S/N) versus strip number (left) and the S/N distribution (right).*

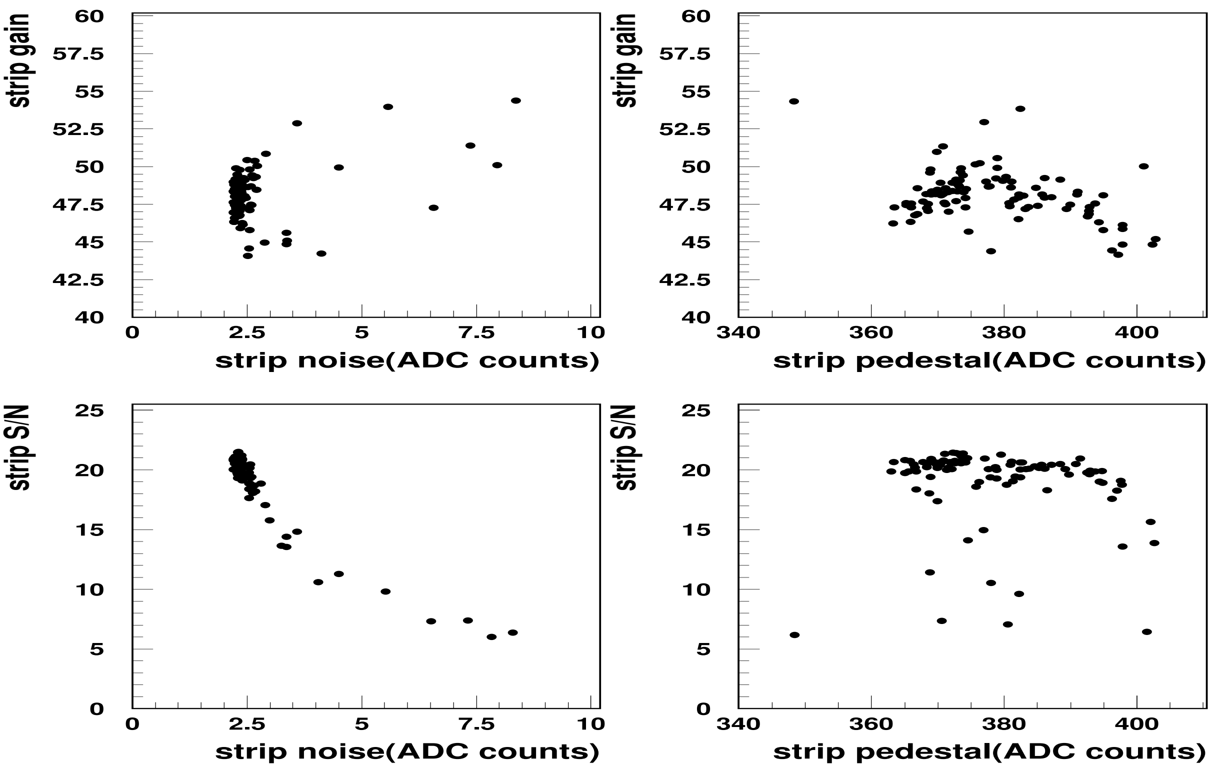

Figure 27: *The strip gain versus strip noise (top left) and the strip gain versus strip pedestal(top right). The strip signal to noise ratio (S/N) versus the strip noise(bottom left) and strip S/N versus the strip pedestal(bottom right). These are calculated from the no-preshower runs 396,397,400,403, for single strip cluster events.*

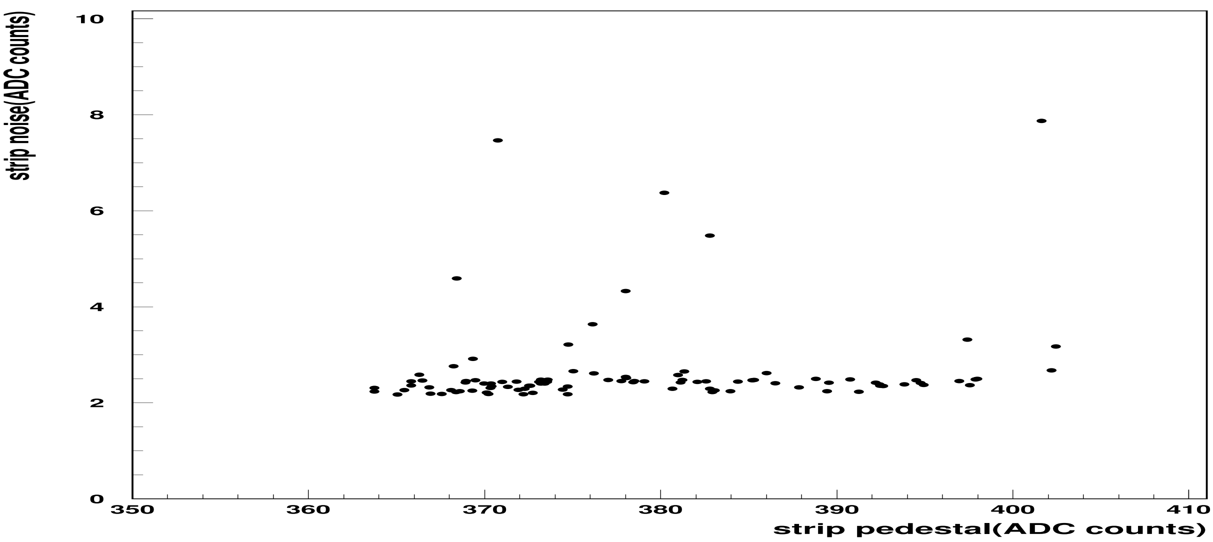

Figure 28: *The strip noise versus the strip pedestal, calculated from the no-preshower runs 396,397,400,403.*

Strip Occupancy:
The ratio between, the total number of events that produce a signal in a given strip i,and the total number of physics events in the run which correspond to a the total number of physics triggers in the run, is called strip occupancy. From figure 29 the average strip occupancy for a no-preshower run is about 0.9%, instead for single strip cluster events it is about 0.4%, which is lower as would be expected. Also by comparing figures 24 and 25 one can get the approximate occupancy value. For preshower runs the strip occupancy is about 3.5%; this higher value is due to the fact that preshower runs have larger clusters consisting of multi-particle events. The ratio for single strip cluster events is not drawn because for preshower runs there are very few single strip cluster events, resulting in very low statistics. The strip occupancy for the preshower run 273 is lower at lower strip number, because for run 273 the silicon detector was in a lower position respect to the incoming electron beam by 2 mm (i.e. not fully centered), resulting in fewer particle hits (signals) in these lower strips. From around strip 50 the strip occupancy flattens out at about 3.5%.

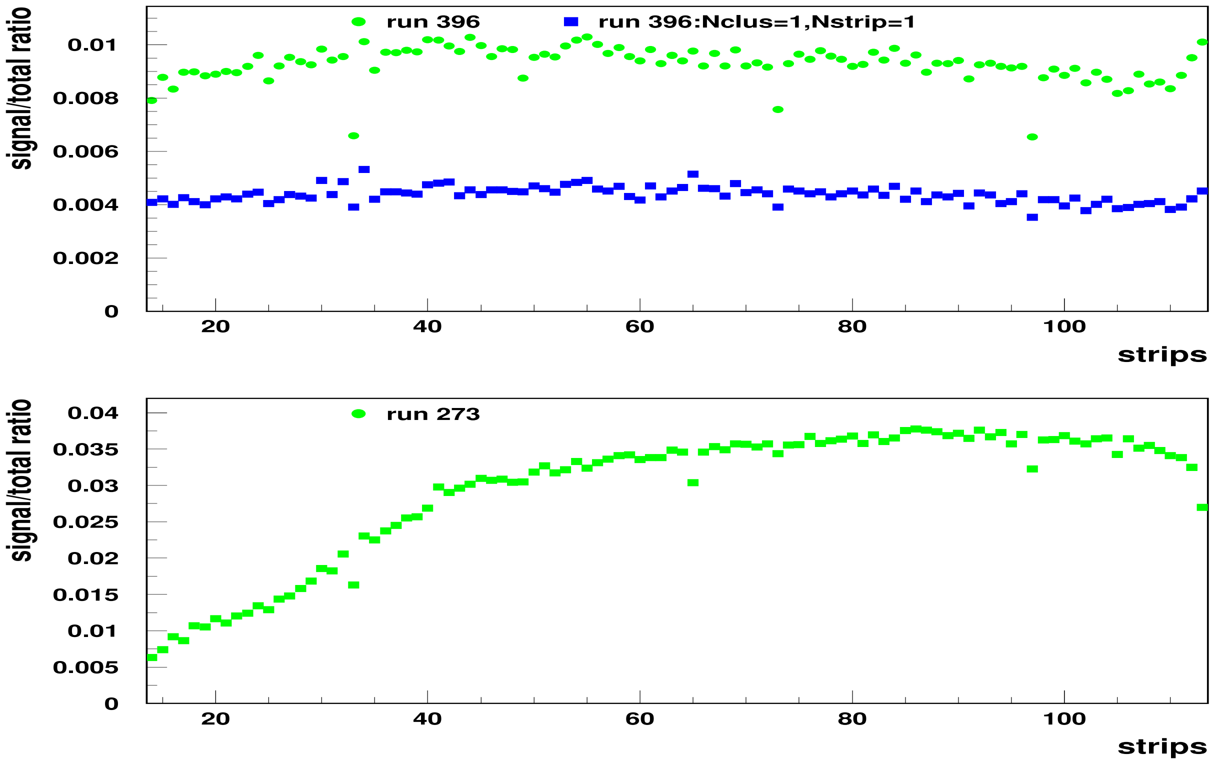

Figure 29: *The ratio between the total number of events that produce a signal in a strip and the total number of events collected in a run, versus the strip number. The ratio is displayed for a preshower run 273 (bottom); and no-preshower runs (396,397,400,403 top) for single strip clusters events and for any cluster type events. Only the first run number 396 is indicted in the label. This ratio is also called the strip occupancy.*

4.2.5 Clusters

Clusters are built from adjacent strips, which share between them the charge deposited by the particle crossing the silicon. A cluster algorithm has been implemented to find and build clusters in the silicon. The cluster algorithm goes through the following steps.
Cluster Algorithm:

- Scan the 100 silicon strips to find the cluster peaks, called also cluster seeds. The condition for a strip i to have a cluster seed is:

$$PH_i = ADC_i - PED_i - CM > 4 * Ni \text{ and } PH_i > 15 \tag{18}$$

  where PH_i is the pulse height in the strip and Ni is the strip noise, see beginning of section 4.2.4. A lower threshold limit on PH_i is applied to cut very low signal clusters.

- Order the cluster seeds in decreasing strip PH_i value.

- Calculate distance between the different cluster seeds i.e. $CLUDIST$ is the number of strips between the two cluster seeds. For example if a cluster seed is at strip 87 and another at strip 80, then CLUDIST=6, and there are 6 strips between the two cluster seeds.

- The minimum distance between two clusters is taken to be $CLUDIST = 6$ i.e there are minimum of 6 strips between the two cluster seeds, otherwise the two cluster seeds are considered to belong to the same cluster. But if there are at least two strips in between the two cluster seeds with no signal, then the two clusters seeds are considered to belong to two separate clusters, even if $CLUDIST \leq 6$.

- If cluster seeds are far apart, $(CLUDIST/2) \geq 7$: then check the PH_i value of ± 7 adjacent strips left and right of the cluster seed, if the strip satisfies $PH_i > 3 * Ni$ add the strip to the cluster seed. Most clusters are only some strips wide, but if the cluster is single or isolated a larger number of strips can be taken into consideration, because anyway the signals will be confined to only to a few strips.

- If cluster seeds are near to one another, $(CLUDIST/2) < 7$: then check the PH_i value for the $\pm lnint(CLUDIST/2)$ adjacent strips left and right of the cluster seed, if the strip satisfies $PH_i > 3 * Ni$ add the strip to the cluster seed ($lnint$ stands for lowest nearest integer).

- The cluster seed with the added strips will constitute a cluster. The reconstructed clusters are ordered in decreasing cluster seed value.

Various parameters (cluster seed signal value, CLUDIST, number of cluster strips, etc.) for the cluster reconstruction have been varied and tested; the above values give the better results.

We first present and define some cluster terminology, that will be used for the reconstructed silicon clusters.

Cluster Signal S_{cl}
The cluster signal S_{cl} is defined as the signal sum of all strips belonging to the cluster:

$$S_{cl} = \sum_{j}^{Nstrips} S_j \tag{19}$$

where:
S_j: is the signal value in strip j;
$Nstrips$: is the number of strips belonging to the cluster.

Cluster Noise N_{cl}
The cluster noise N_{cl} is defined as the quadratic mean of the strip noise for all strips in the cluster:

$$N_{cl} = \sqrt{\sum_{j}^{Nstrips} (N_j)^2/(Nstrips)} \tag{20}$$

where:
N_j: strip noise of strip j;
$Nstrips$: is the number of strips belonging to the cluster.

Cluster Signal to Noise Ratio S/N_{cl}
The cluster signal to noise ratio S/N_{cl} is defined as the ratio between the cluster signal S_{cl} and the cluster noise N_{cl}:

$$S/N_{cl} = \frac{S_{cl}}{N_{cl}} \tag{21}$$

Cluster Position P_{cl}
The cluster position P_{cl} is defined as the signal center of gravity of the cluster:

$$P_{cl} = \frac{\sum_{j}^{Nstrips} S_j j}{\sum_{j}^{Nstrips} S_j}. \tag{22}$$

The particle position is reconstructed using the simple hypothesis that there is a linear charge sharing between the strips. This assumption is valid only as a first approximation.

Figures 31 and 30 show the event displays in the silicon for various cluster types, reconstructed using the above mentioned algorithm. For no-preshower runs (run 396) there is typically one cluster with a width of one or two strips. For preshower runs (run 273) there are typically more clusters, of which each can be made up of several strips. In the top part of each event display the cluster parameters are written, the color (or grey shade) of the text corresponds to the colour (or grey shade) of the cluster. The clusters are ordered according to the decreasing cluster seed (or cluster peak) value. The parameters have the following meaning:

- $Nclus$= total number of clusters found in an event.
- Clu= cluster number, the first cluster corresponds to the cluster with the highest cluster seed value, and so on in decreasing value.
- $Nstrips$= the number of strips belonging to the cluster.
- Sig= total cluster signal, see equation 19.
- $Noise$= cluster noise, see equation 20.
- S/N= cluster signal to noise ratio, see equation 21.
- Pos= the cluster center gravity, see equation 22.
- $clupeak$= the cluster peak value i.e. the cluster seed.

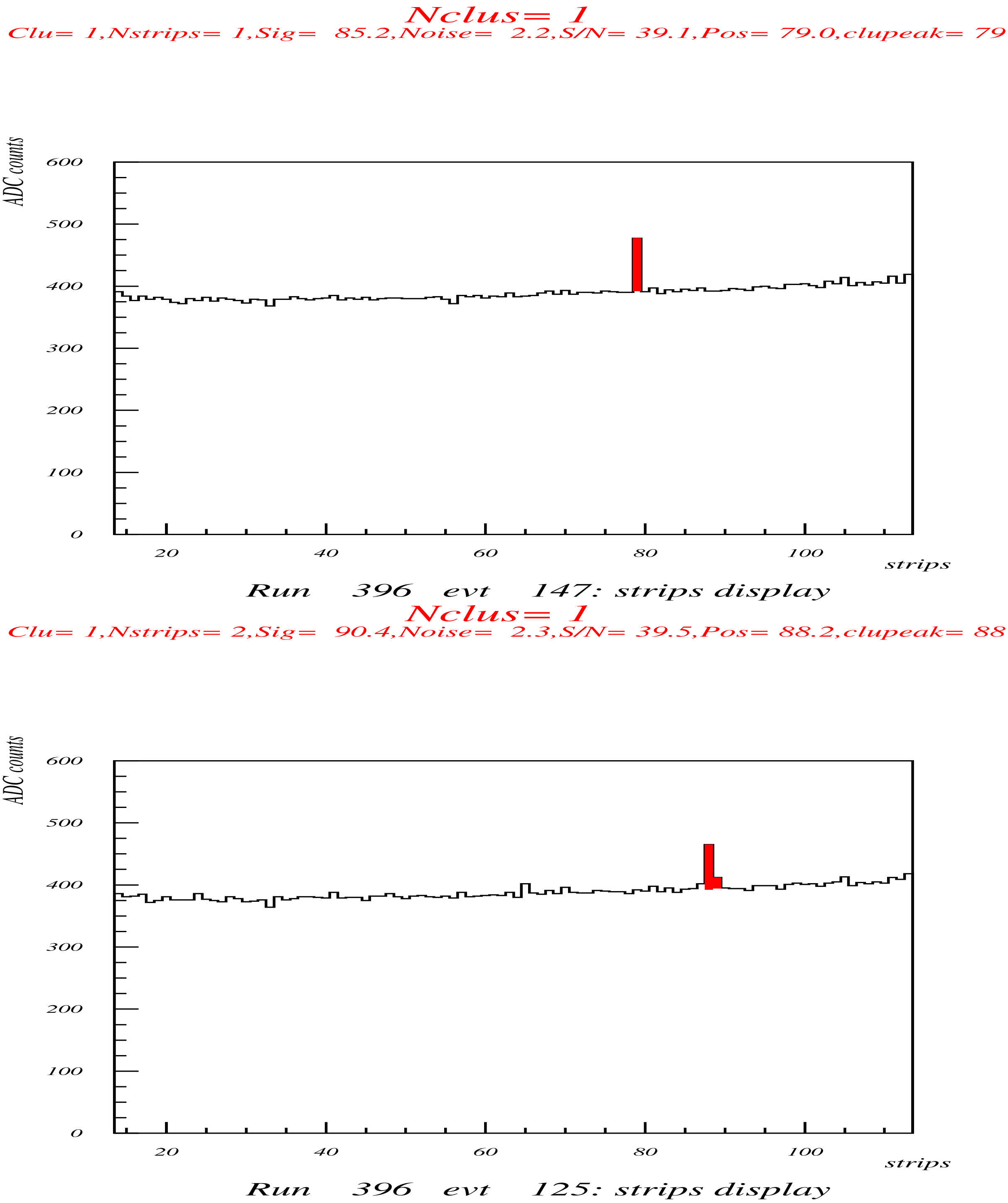

Figure 30: *Event display for clusters found in the silicon for a no-preshower run.*

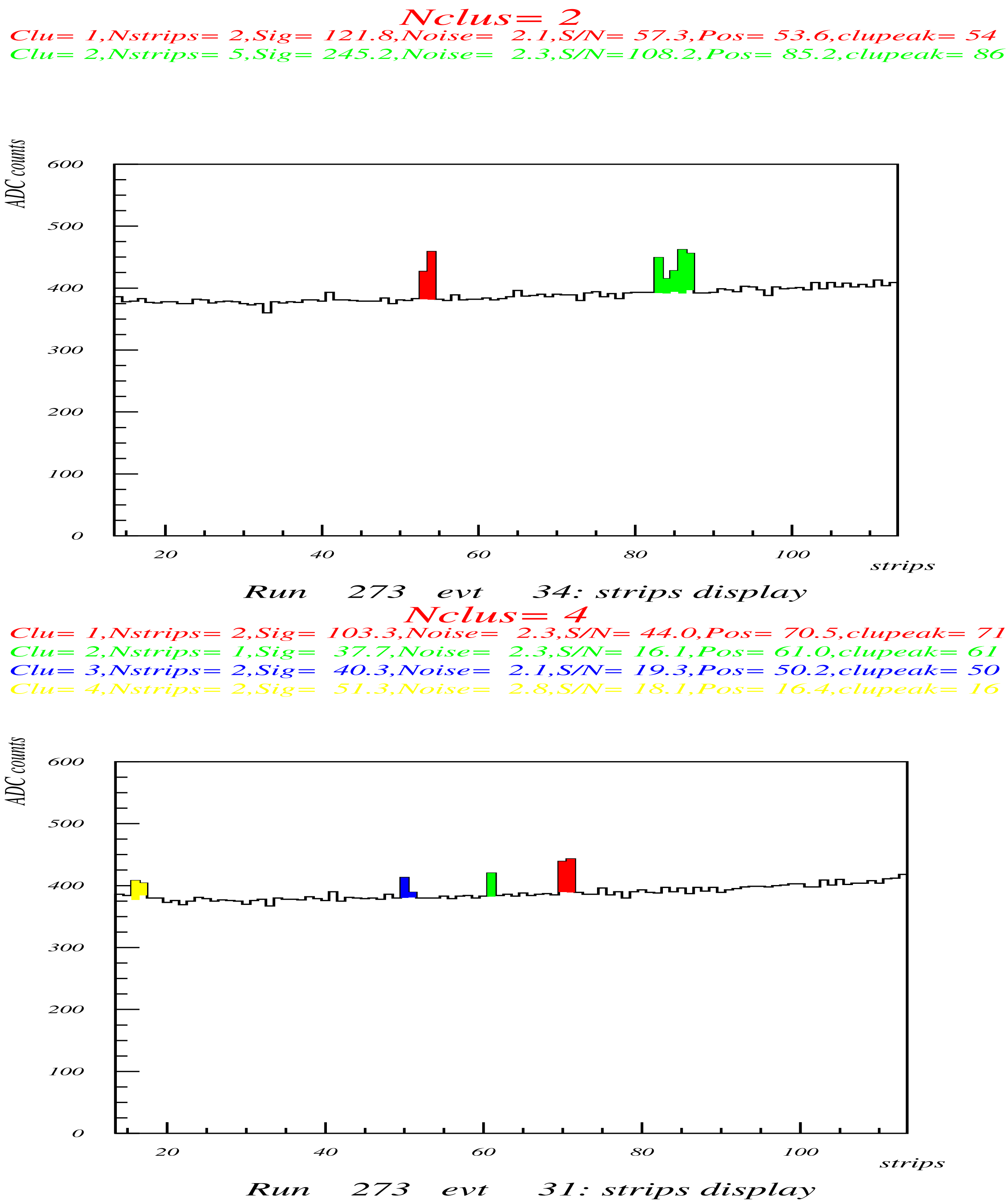

Figure 31: *Event display for clusters found in the silicon for a preshower run.*

The general cluster variables for preshower and no-preshower data are displayed in figures 32,33, 34,35.

- **Cluster Signal**: the cluster signal (no-preshower data) generally follows a Landau distribution as would be expected for a charged particle crossing a thin layer of matter (one particle hit). A Landau distribution is fitted to the cluster signal distribution. In the case of preshower data the cluster signal distribution tail is clearly higher then the Landau curve, because clusters tend to be larger and with more energy deposited in the silicon detector, a multi-particle hit.

- **Cluster Noise**: The cluster noise distribution is non-Gaussian. Its mean value is ~ 2.3ADC-counts. A Gaussian is fitted for comparison. The cluster noise distributions look somewhat different because on average there are fewer strips in a no-preshower cluster than a preshower cluster; which then add up differently in the cluster noise calculation.

- **Cluster Signal/Noise Ratio**: The mean value for the cluster S/N ratio distribution is $\sim$ 25 (no-preshower) and $\sim$ 35 (preshower). Again the difference in the cluster S/N ratio value for the two data sets, is due to the greater number of strips in the preshower clusters. The noisy silicon channels are responsible for the low S/N ratio events in the plot.

- **NCLUS**: No-preshower events have mostly 1, sometimes 2 clusters, while preshower events tend to have several clusters.

- **Number of cluster strips**: Most no-preshower events have clusters composed of 1-2 strips, instead preshower events have wider clusters (several strips).

- **Reconstructed Cluster Position**: The reconstructed cluster position is basically flat for no-preshower data, because the silicon was centered with respect to the beam, and the beam was wide so that all the silicon active surface was hit. For preshower data there are fewer hits at lower silicon strip number because the whole detector was 2 mm lower with respect to the no-preshower data polarimeter table position (see also figure 29 for comparison).

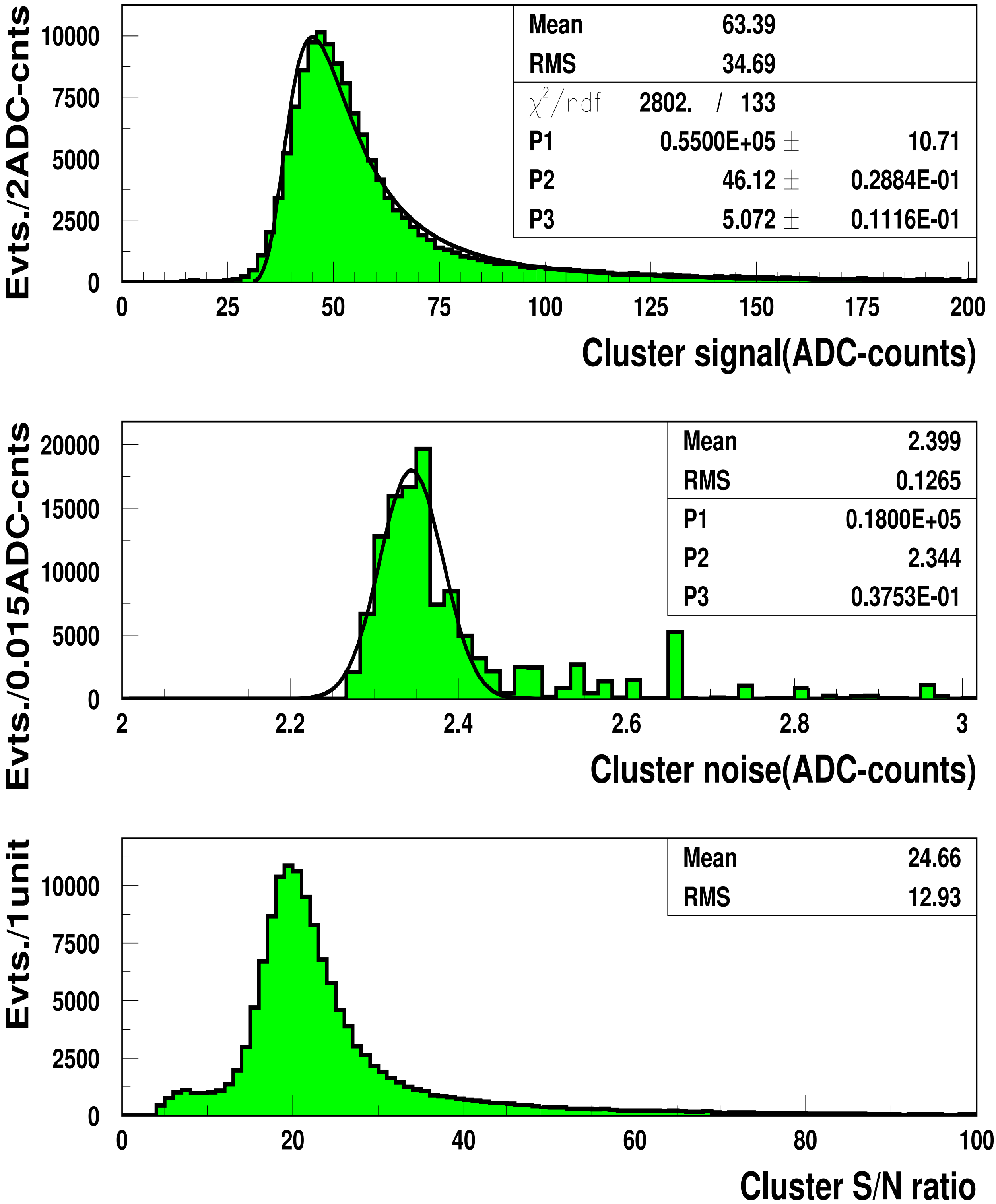

Figure 32: *Cluster variables. No-preshower data (runs 396,397,400,403).*

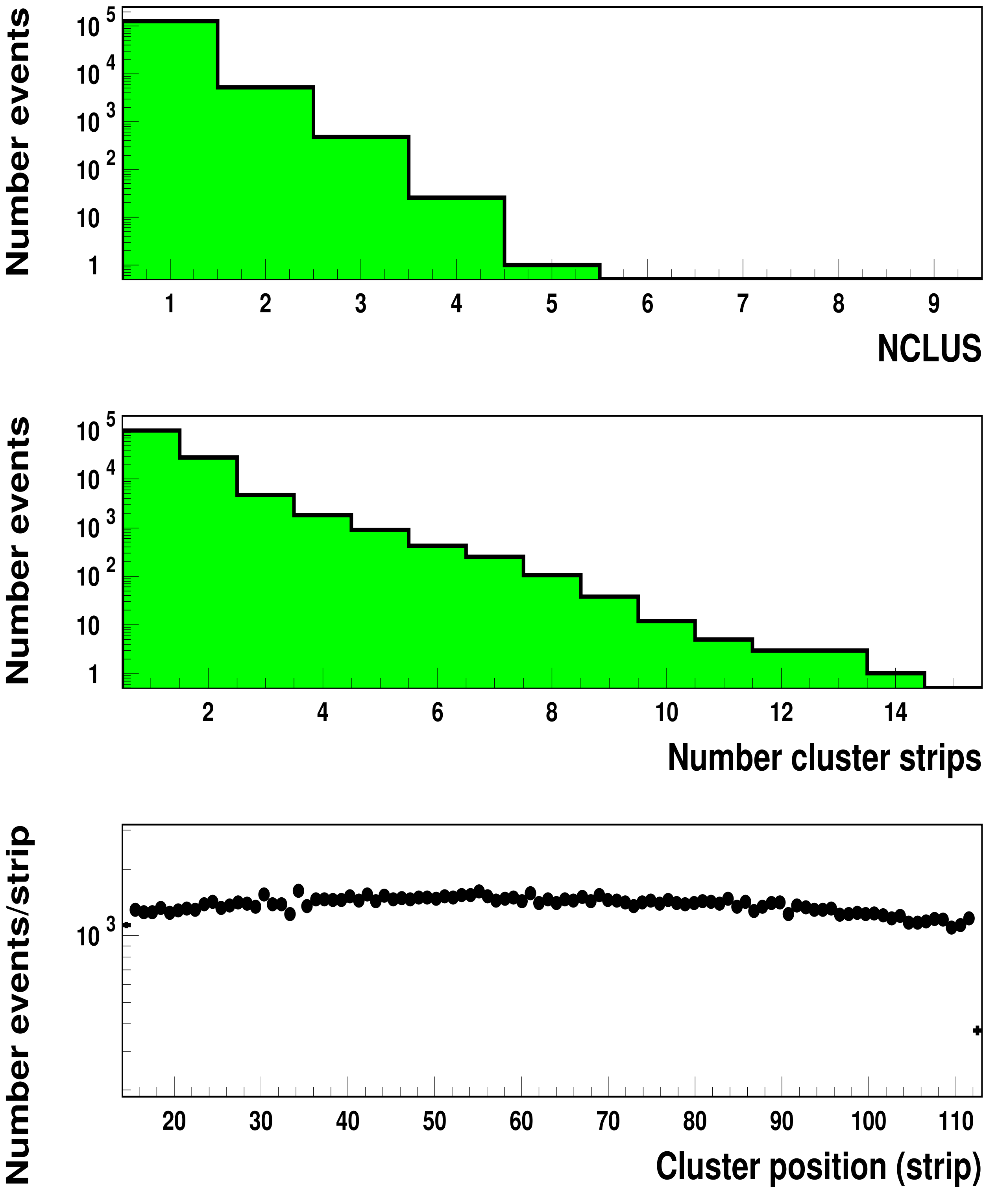

Figure 33: *Cluster variables. No-preshower data (runs 396,397,400,403).*

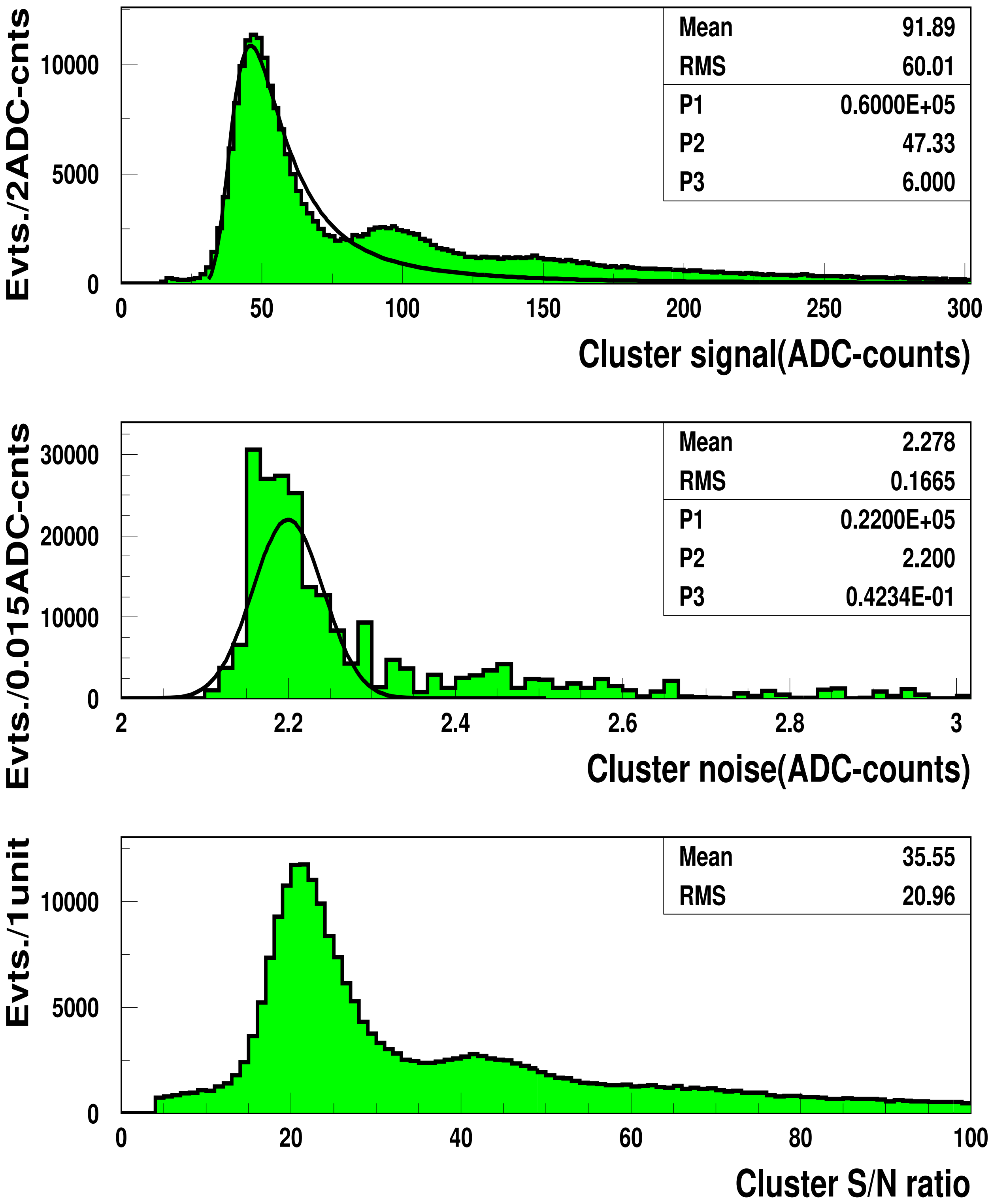

Figure 34: *Cluster variables . Preshower data (run 273).*

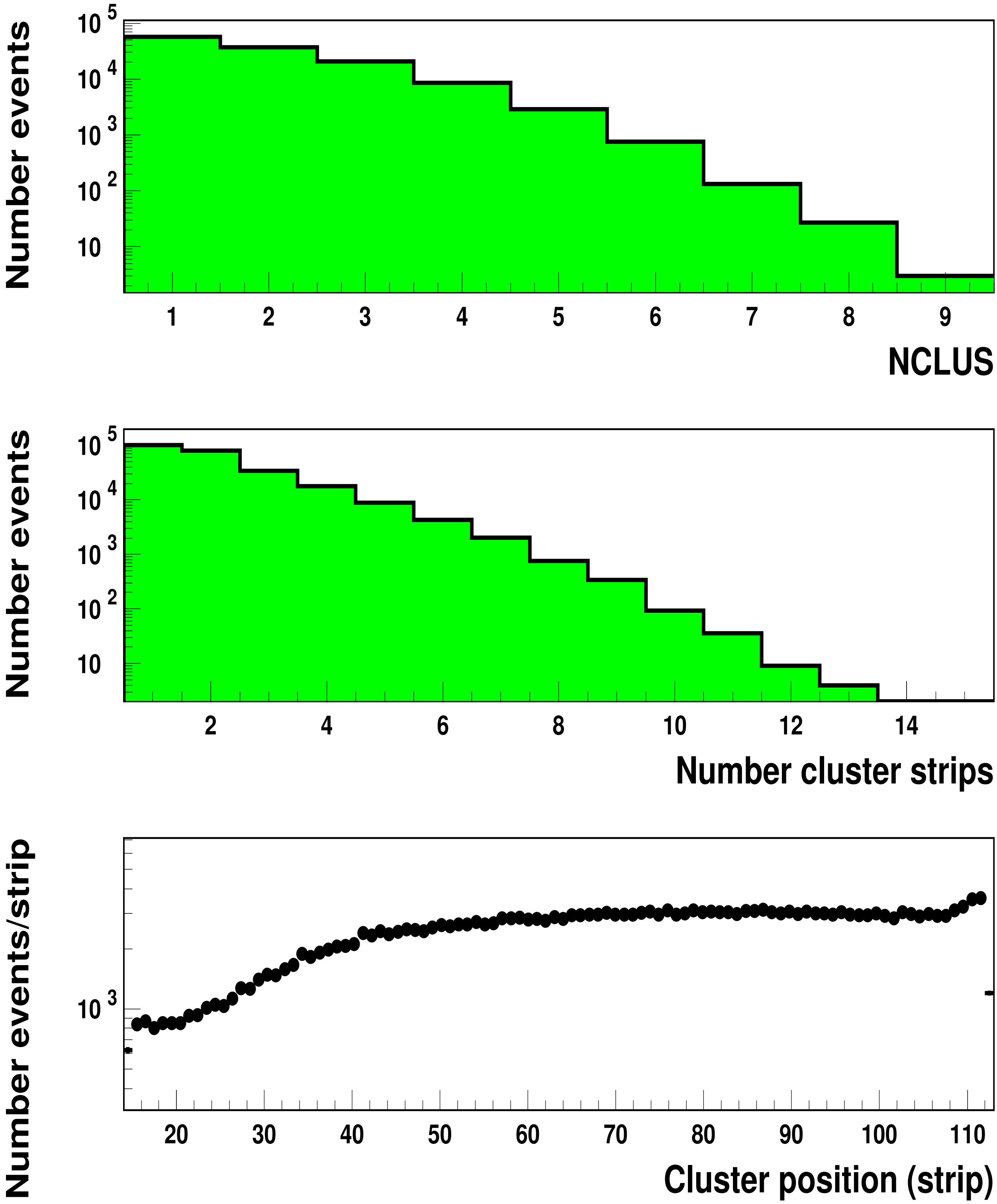

Figure 35: *Cluster variables . Preshower data (run 273).*

The distributions for the number of strips found left and respectively right of the cluster peak strip, are very similar when compared to one another, in both preshower and no-preshower data, as can be seen in figures 36 and 37 (top plots) . The clusters strips L/R distribution is symmetric around the cluster peak as would be expected. The L/R strip distribution falls steeper in the no-preshower case.

The average signal pulse heights for the strips in a cluster as function of the relative strip number is shown in 36, 37 (middle plots). The cluster peak is defined to have a relative strip number of 0, the first strip to the left a relative strip number of -1, and the first strip to the right a relative strip number of 1, and so on. For relative strip numbers ± 1, there is a dip because most clusters consist of up to 3 strips and the signal is smaller in the first left/right strips; for larger clusters signal rises again in the second left/right strips (multi-particle hits) to then be approximately constant on average over the other relative strip numbers. Again there is a difference in the average signal pulse heights between preshower (multi-particle clusters) and no-preshower (mainly single particle clusters) runs because different charge sharing in the cluster strips .

The η_{cl} distribution (figures 36, 37, bottom plots) for clusters consisting of more than one strip, is defined as:

$$\eta_{cl} = \frac{Q_R}{Q_R + Q_L} \tag{23}$$

where Q_R and Q_L are the signal sums of the strips right and left of the cluster reconstructed position. η_{cl} is related to the charge sharing between strips. For two-strip clusters (36, bottom plot, dashed line), η_{cl} close to 0 and 1 is favoured, that is, two-strip clusters occur more often when the incoming particle hit position is close to the readout strips. Meanwhile clusters larger than two strips occur more often when the reconstructed cluster impact position is in the middle area between two readout strips. This can be seen by comparing in figure 36 the dashed plot (Nstrips=2) with the continuous line plot (Nstrips ≥ 2). For the preshower data (figure 37), the two-strip clusters clusters are favoured also for η_{cl} close to 0.5, this because preshower clusters have a different cluster strip structure due to the multi-particle hits.

The cluster signal distribution for different cluster widths (number of strips in cluster), is shown in figures 38, 39. For no-preshower data, clearly most clusters are 1 or 2 strips wide, not so for the pre-shower data. For the preshower data the 1-strip cluster events, follow the Landau curve shape, meanwhile the 2-strip cluster events have a smaller second peak around 95 ADC-counts, due to the effect of multi-particle hit events. These smaller peaks can be seen also on the lower log scale plot of figure 39, for 2-strip, 3-strip, and 4-strip cluster events.

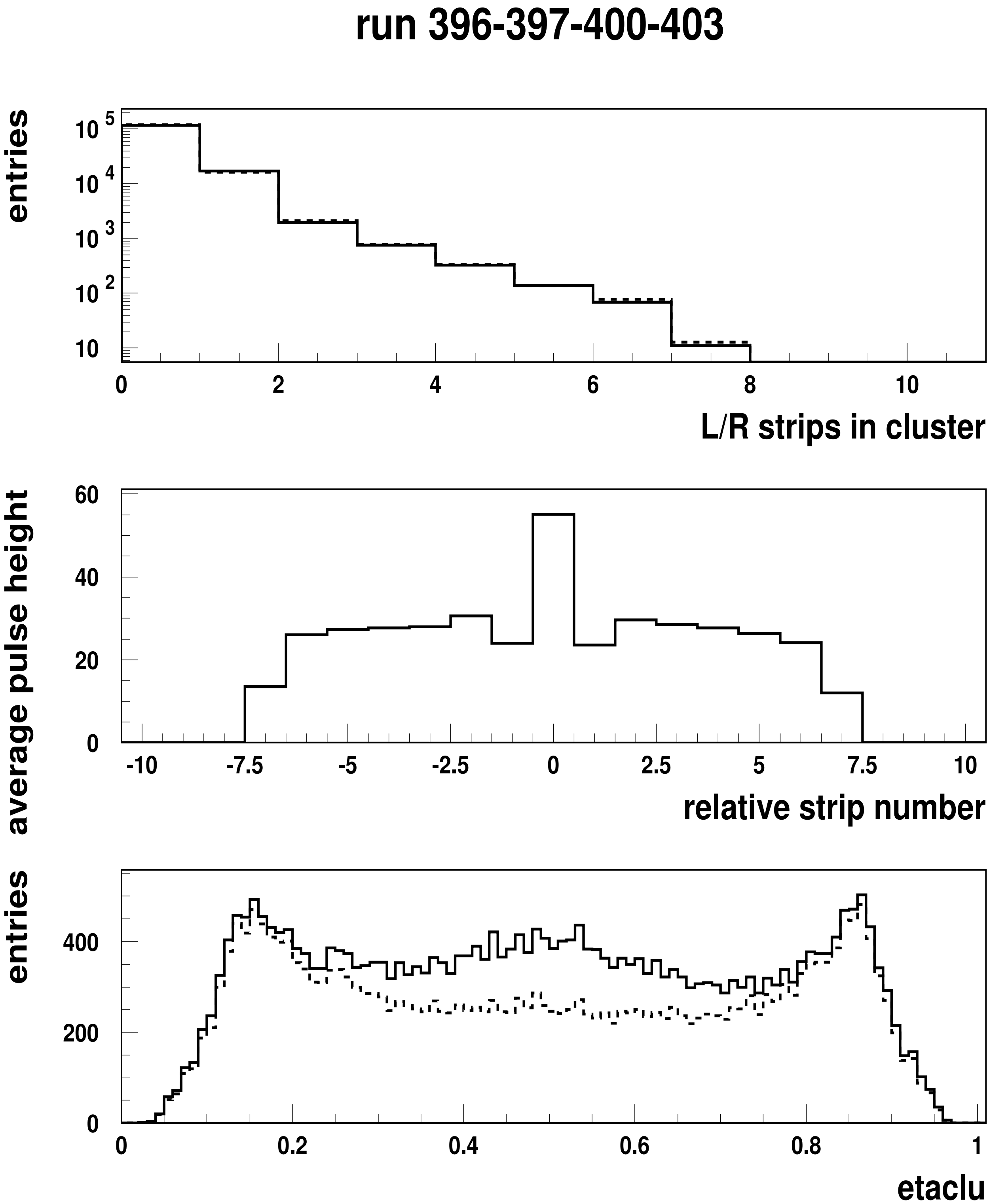

Figure 36: *No-preshower data (runs 396,397,400,403). Top plot, distribution of the number of strips found left and respectively right of the cluster peak strip, superimposed. Middle plot, the average pulse heights for the strips in a cluster as function of the relative strip number. Bottom plot, the η_{cl} distribution; the dashed line corresponds to two strip clusters, while the continuous line corresponds to clusters with two or more strips; only events with one cluster are selected NCLUS=1.*

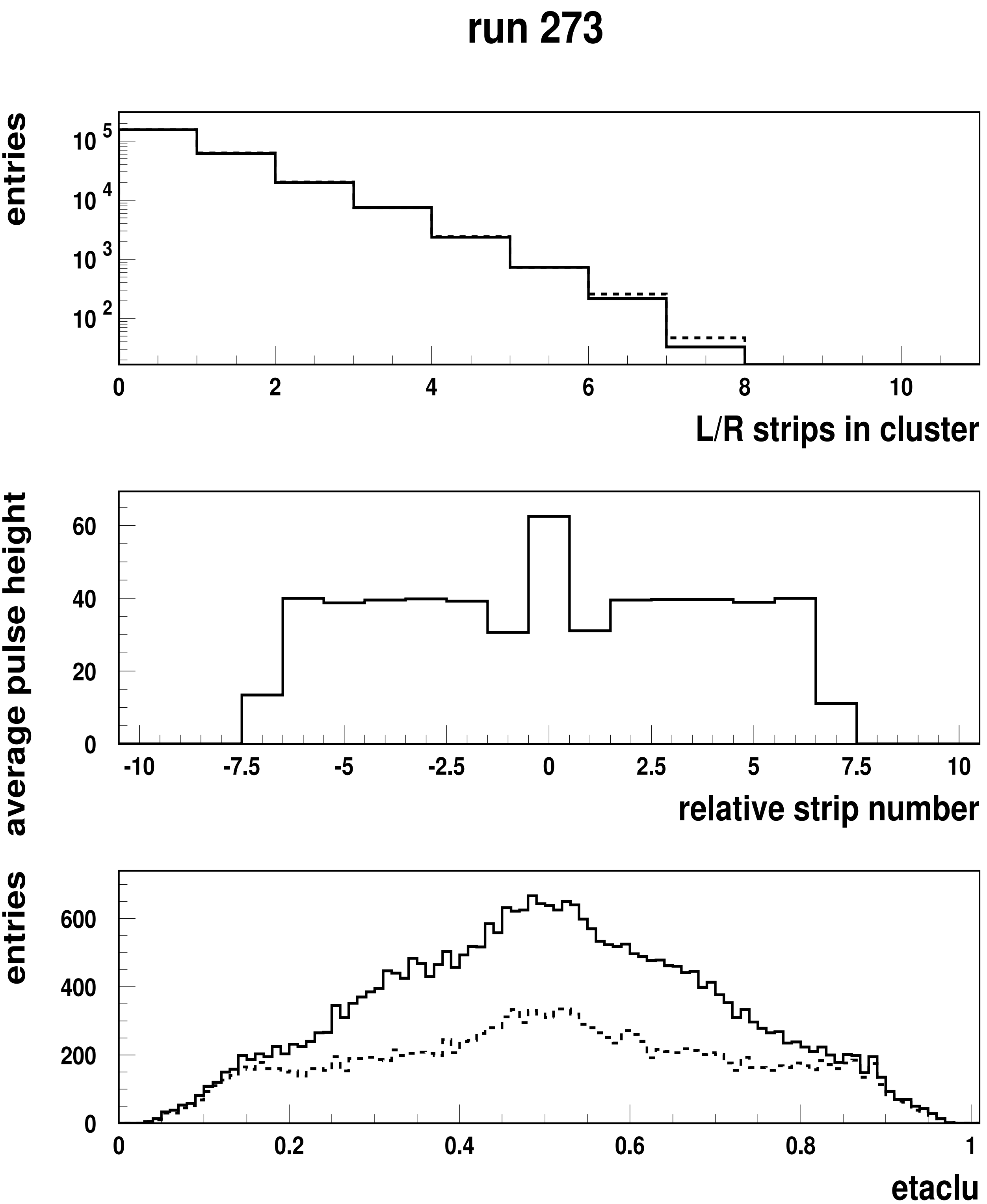

Figure 37: *Preshower data (run 273). Top plot, distribution of the number of strips found left and respectively right of the cluster peak strip, superimposed. Middle plot, the average pulse heights for the strips in a cluster as function of the relative strip number. Bottom plot, the eta$_{cl}$ distribution; the dashed line corresponds to two strip clusters, while the continuous line corresponds to clusters with two or more strips; only events with one cluster are selected NCLUS=1.*

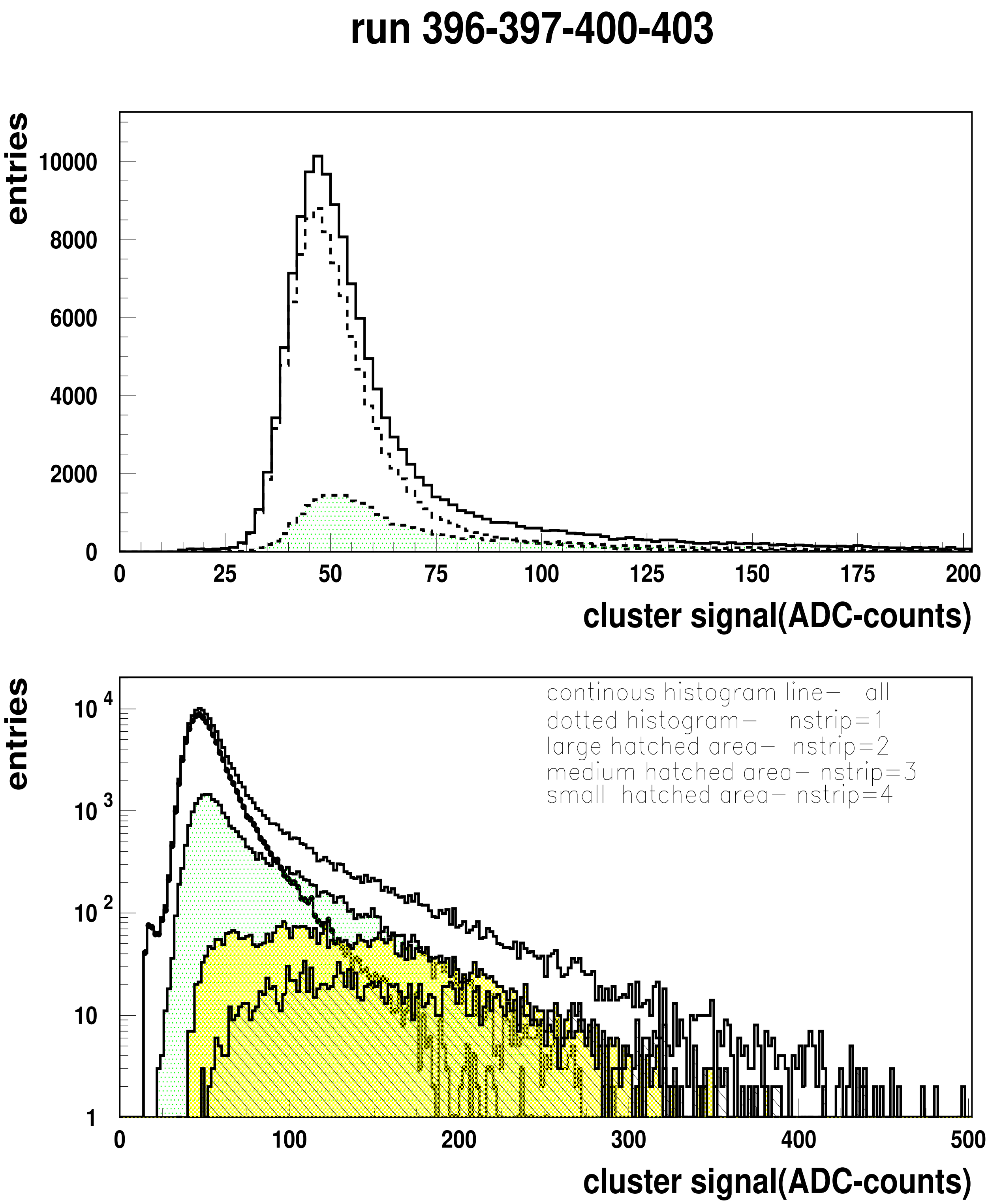

Figure 38: *The cluster signal distribution. Top plot, the cluster signal distribution for all clusters (solid line), for 1-strip clusters (dashed line), for 2-strip clusters (hatched area). Bottom plot,the cluster signal distribution on log scale. No-preshower data (runs 396,397,400,403).*

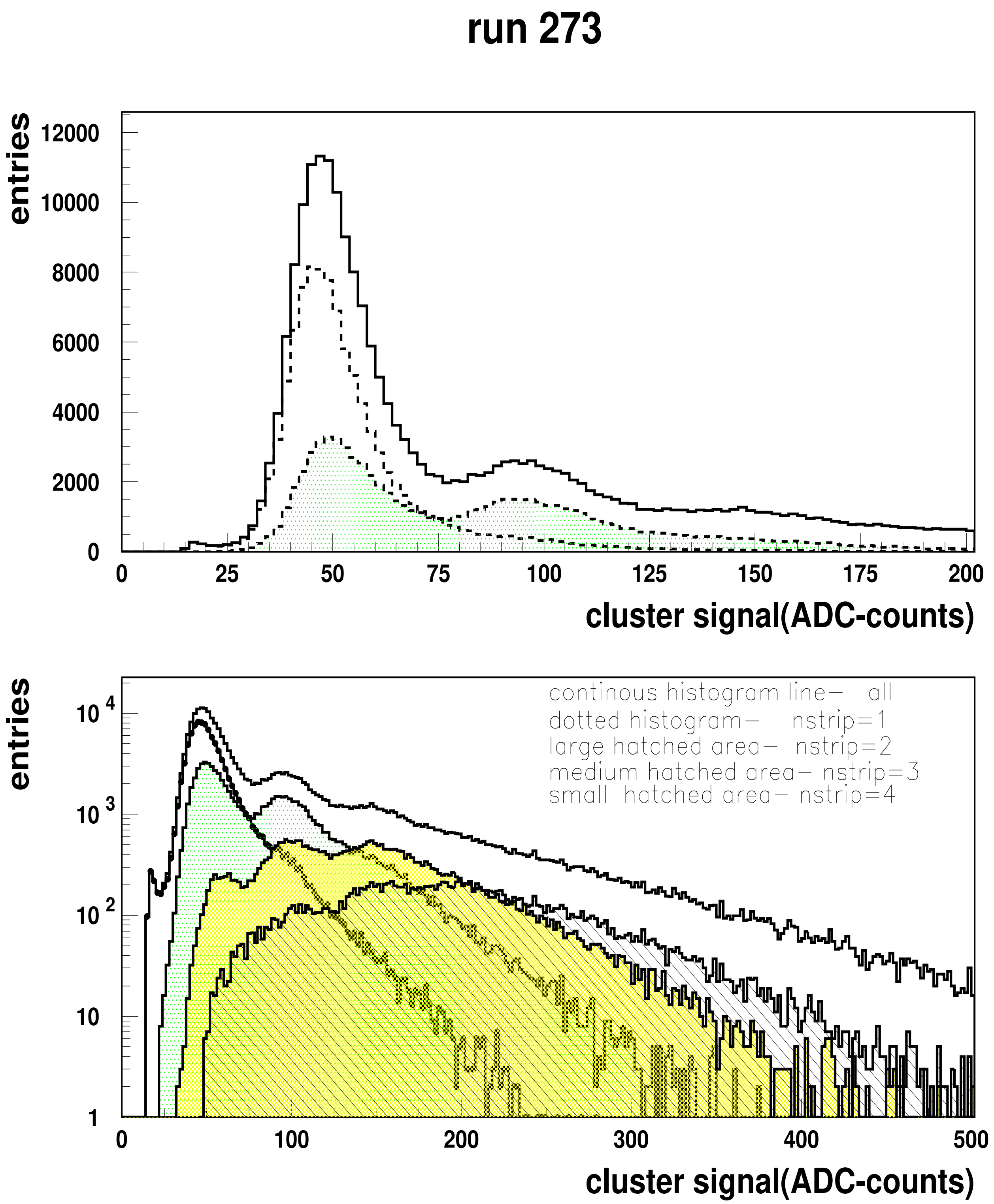

Figure 39: *The cluster signal distribution. Top plot, the cluster signal distribution for all clusters (solid line), for 1-strip clusters (dashed line), for 2-strip clusters (hatched area). Bottom plot,the cluster signal distribution on log scale. Preshower data (run 273).*

4.2.6 Bias Voltage Scan

A bias voltage scan was performed to investigate the effect of different bias voltages on the strips S/N ratio (-20 V,-40 V,-60 V,-80 V,-100 V). Figure 40 shows the mean pedestal value and noise for the 128 APV25 channels, at the different bias voltages (compare with figure 22). The 28 unconnected strips (1-13, and 114-128) have a lower raw noise value and the mean pedestal value is flat in the unconnected strips region. The mean pedestal value is practically unchanged for the different bias voltage settings. The raw noise is clearly higher ~ 8 ADC-counts, at -20 V bias. For the other bias settings the raw noise values differ slightly one from another ~ 6.5 ADC-counts; the lowest values being for -60 V bias.

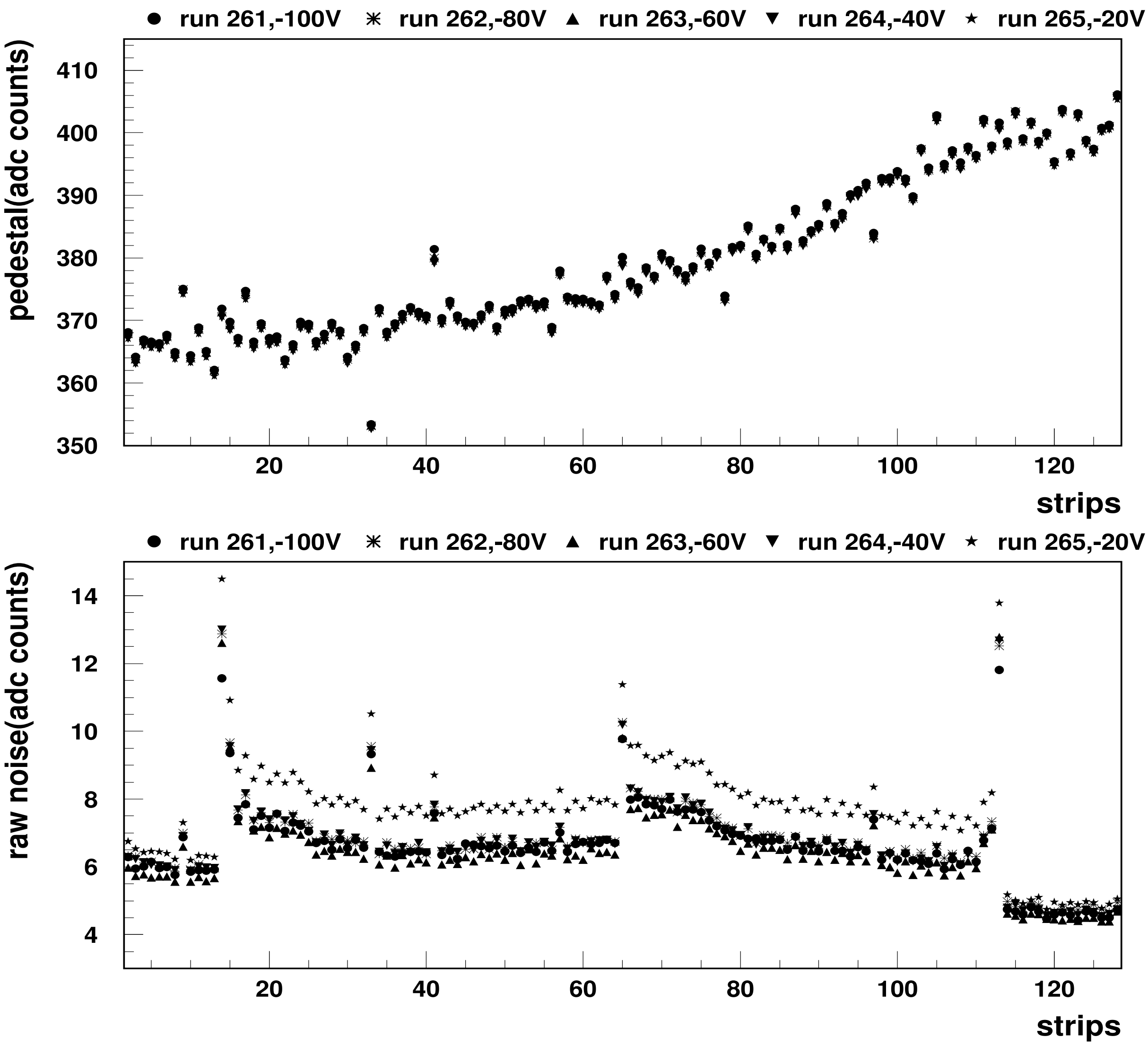

Figure 40: *The mean pedestal value and noise for the 128 APV25 channels, at different bias voltages. Only strips 14 to 113 are connected.*

The common mode baseline shift (CM) for the bias scan is shown in 41. The mean is around zero and the shapes are similar. The RMS of the distribution increases from ~6.5 ADC-counts for (-60 V,-80 V,-100 V) to ~8 ADC-counts for -20 V bias.

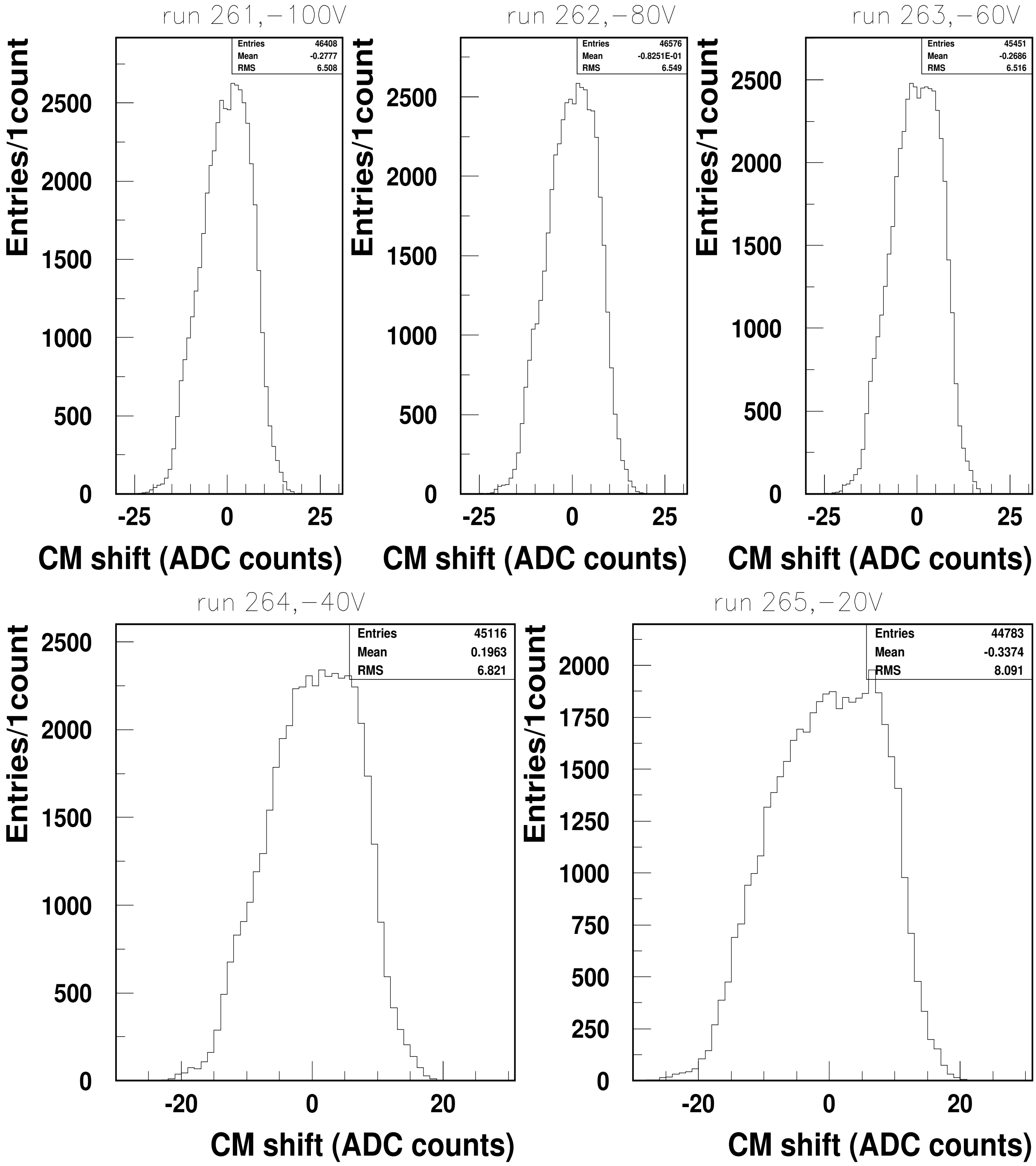

Figure 41: *The common mode baseline shift (CM) for the different bias voltage settings.*

The strip noise for the bias voltage scan is shown in figure 42. The highest strip noise ($\sim$ 2.3 ADC-counts) is for a bias of -100 V, while for the other settings the strip noise is similar ($\sim$ 1.6 ADC-counts). The reason for this behavior is that the common mode subtraction is applied e.g. also if for a bias voltage -20 V the raw noise is larger, the CM subtraction is also larger (see figure 41) resulting in a strip noise similar to the other bias voltage settings. The strip S/N ratio is not shown because these runs had the preshower installed, resulting in very few statistics for single-strip clusters, instead the cluster signals will be investigated. Figures 42, 44 show the cluster signal and the cluster S/N ratio. The bias scan runs were taken with the preshower material still installed. The mean cluster signal value decreases with decreasing bias voltage, meanwhile the best cluster S/N ratio is for a bias voltage of -80 V.

Except for very low bias voltages, the noise values are expected to remain practically constant as the bias voltage is increased as seen in figure 40; instead the signal should increase to a maximum value, which occurs at total depletion, that is, when the depleted region covers the whole active silicon chip. A slight improvement in the S/N ratio can occur also after total depletion, because of an increased charge collection efficiency due to the higher electric field in the silicon, as seen in figures 42, 44. Total depletion for the silicon should occur around -70 V [11]. From the bias voltage scan, the bias -80 V gives the best cluster S/N ratio. Therefore using a bias voltage around -80 V the present strip S/N ratio value of $\sim$ 21 can be increased.

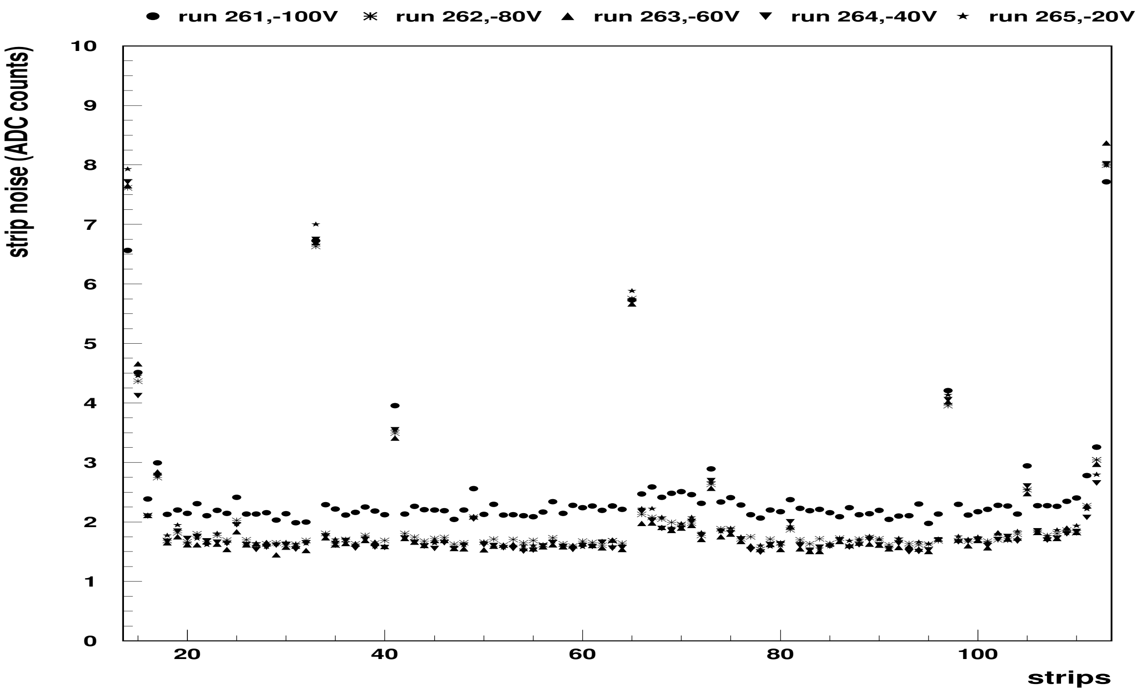

Figure 42: *The strip noise for the different bias voltage scan values.*

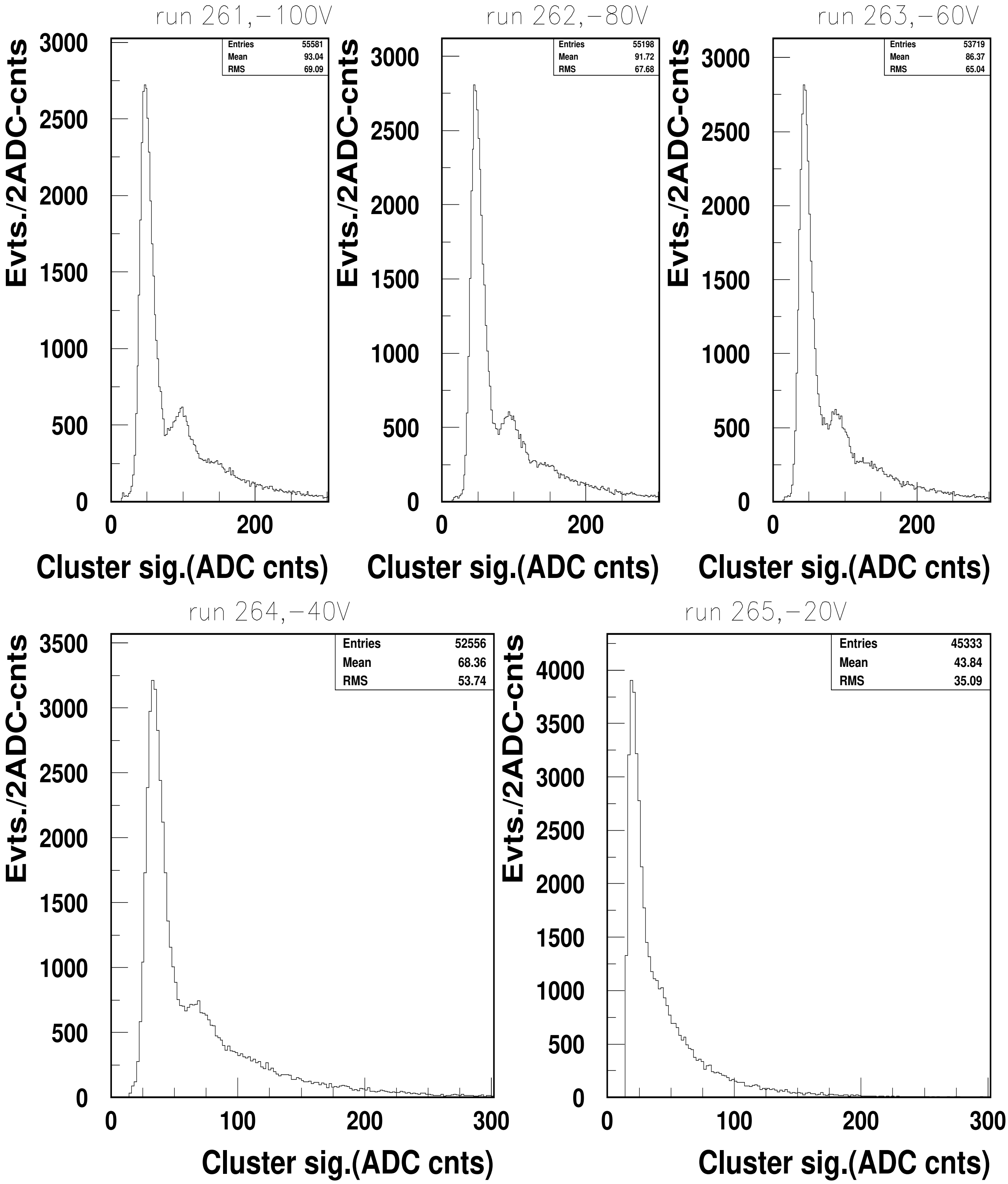

Figure 43: *Cluster signal for the different bias voltage scan values.*

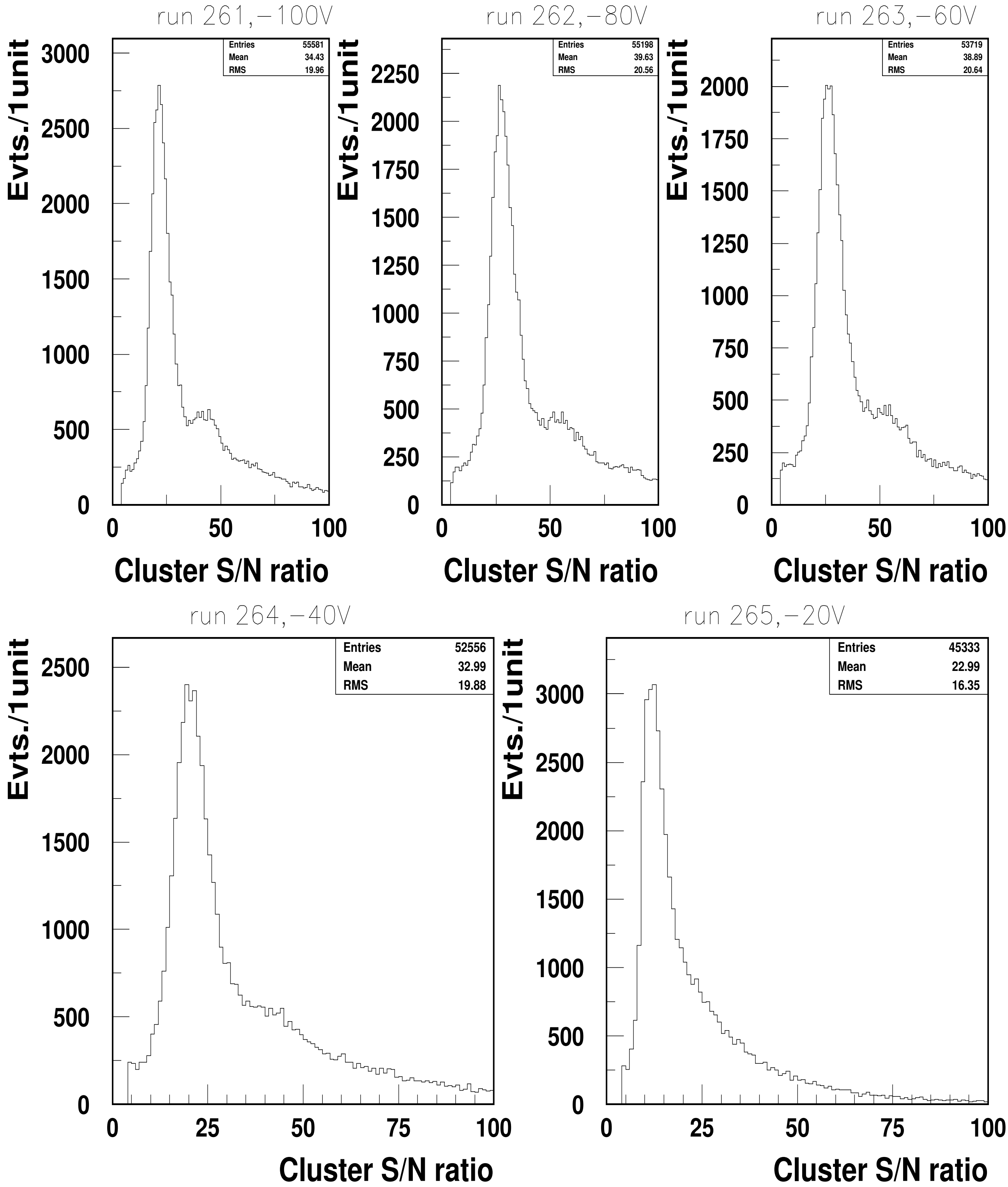

Figure 44: *Cluster S/N ratio for the different bias voltage scan values.*

4.2.7 The Eta-Y Transformation

As already discussed in the introduction (section 1) of this note, the precise determination of the η-y transformation is of primary importance for improving the accuracy of the transverse polarization measurement. The purpose of the silicon microstrip detector is to determine accurately the η-y transformation in situ, during data-taking. In section 4.1 the η-y transformation results, with y measured from the test-beam telescope are presented. The eta (η) variable is defined as (see section 1):

$$\eta = \frac{E_u - E_d}{E_u + E_d} \tag{24}$$

where E_u and E_d are the measured energy deposits in the upper (UP module) and lower module (DOWN module) of the TPOL calorimeter, respectively. In this section, the y variable is the vertical coordinate of the incident particle hit position measured by the silicon microstrip detector: the silicon strip number is converted into centimeters, and y is centered with respect to the calorimeter vertical center i.e. y=0 for η =0. The test-beam energy is 6 GeV for both data sets: no-preshower and preshower runs. Figure 45 shows the η-y scatter plot for the two data sets.

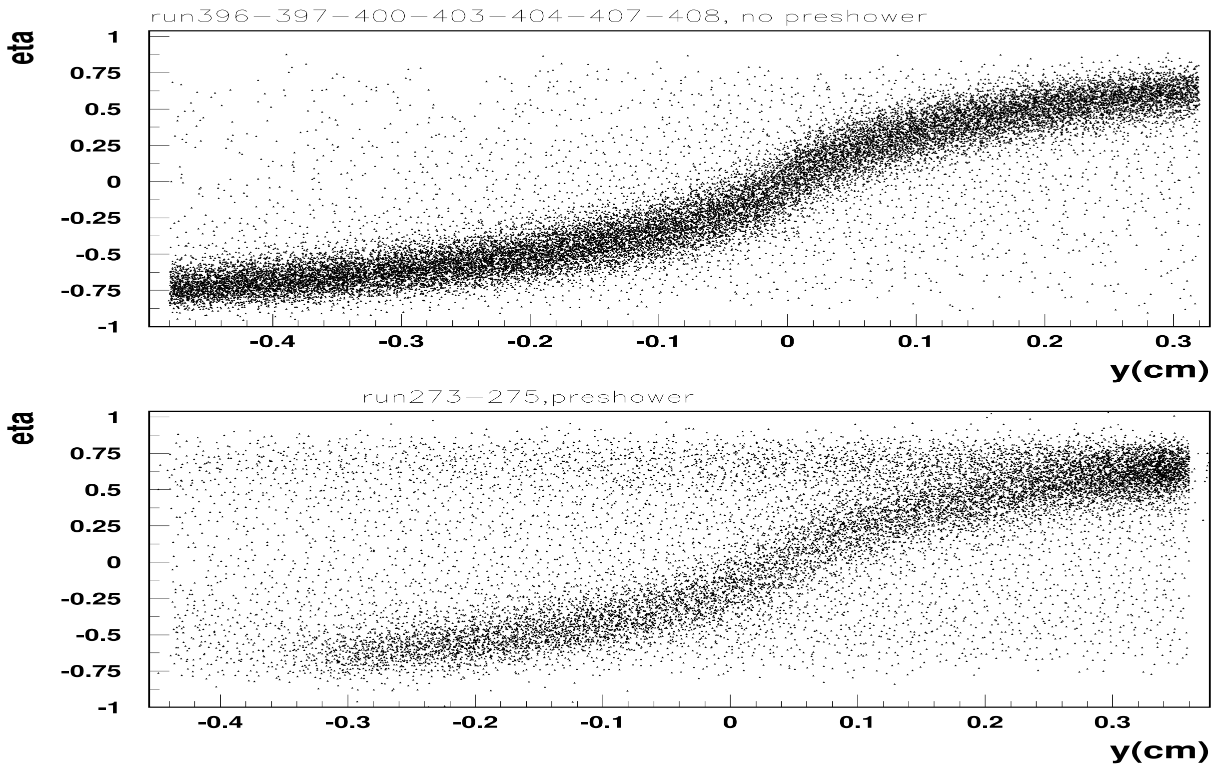

Figure 45: *The η-y scatter plot for no-preshower (runs 273 and 275) and preshower runs(396,397,400,403,404,407,408). The y variable is measured by the silicon detector. For both data sets the test-beam energy is 6 GeV.*

The η-y scatter plots are obtained by requiring that there is only one reconstructed cluster in the silicon, a lower threshold cut is applied to the cluster signal and calorimeter signal values. In both plots (figure 45) one can see the clear shape of the η-y relation. The lower plot in figure 45 (preshower) has fewer points at y<-0.3cm, because for the preshower data the TPOL was 2 mm lower than in the no-preshower setup, resulting in fewer hit in the silicon (edge of the beam, see figure 29); η is not very sensitive to a 1-2 mm TPOL table shift. The darker region at positive y and η ~0.75 is thought to be due some slice of extra preshower material in front of the colorimeter which we were not aware of.

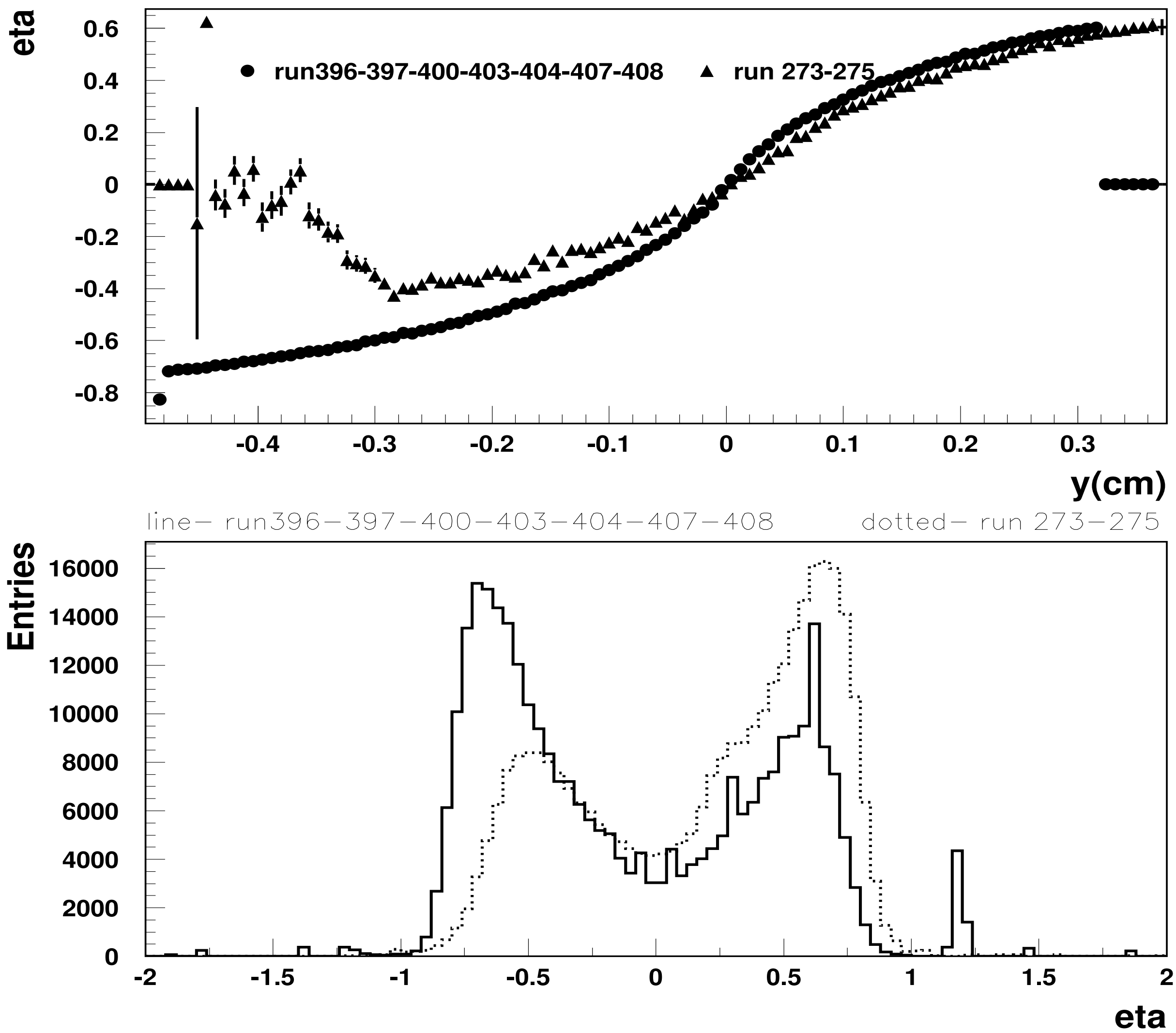

Figure 46: *Top plot, the η-y profile histograms for no-preshower (runs 273 and 275) and preshower runs(396,397,400,403,404,407,408), superimposed. Bottom plot, the η calorimeter distribution, both data sets contain the same number of events.*

Figure 46 compares the η-y transformations as profile histograms. The preshower η-y transformation is flattened out with respect to the no-preshower η-y transformation. This is a typical effect of the preshower material; the more material the more flattened out the η-y transformation, because the showers incident on the calorimeter face become larger. For preshower data at y<-0.3cm (edge of the beam) the the plot rises towards η =0.

The lower plot of figure 46 compares the η distribution for the two data sets (same number of events); with no cuts applied. If some cuts (e.g. low energy calorimeter threshold) are applied the basic shape remains the same.

Figure 47 displays the fitted η-y profile histograms. The fitted function is of the type (y is the vertical coordinate):

$$\eta(y) = \frac{|y|}{y}\left[1 - e^{-|y|/P_3} + P_1(e^{-|y|/P_3} - e^{-|y|/P_2})\right] \tag{25}$$

The slices in y where Δy=80μm; the η means for each slice is plotted as a profile histogram and then fitted. The continuous line is the η-y transformation at 8 GeV, for the old CERN test-beam data; instead the semi-continuous line is the η-y transformation obtained from the telescope data (see section 4.1). In both cases the test-beam η-y transformation is flatter then the CERN data. There are slight differencies (top plot) between the η-y transformation obtained from the telescope and silicon data, due to different elctronics, calibration, method used etc.. The preshower data was fitted only between -0.1$\leq$ y$\leq$3.7, because the fit worsens if extended in the negative y region, while for no-preshower data the fit was between -0.45$\leq$ y$\leq$0.3.

These preliminary results are positive. To do a proper η-y transformation study, data should be taken at various higher test-beam energies. The main range of interest is between 5-14 GeV, the incident Compton photon energy range. A test-beam is foreseen at CERN with energies up to 50 GeV, at the end of July 2001, with the new TPOL setup i.e. 6*6 cm^2 silicon detector.

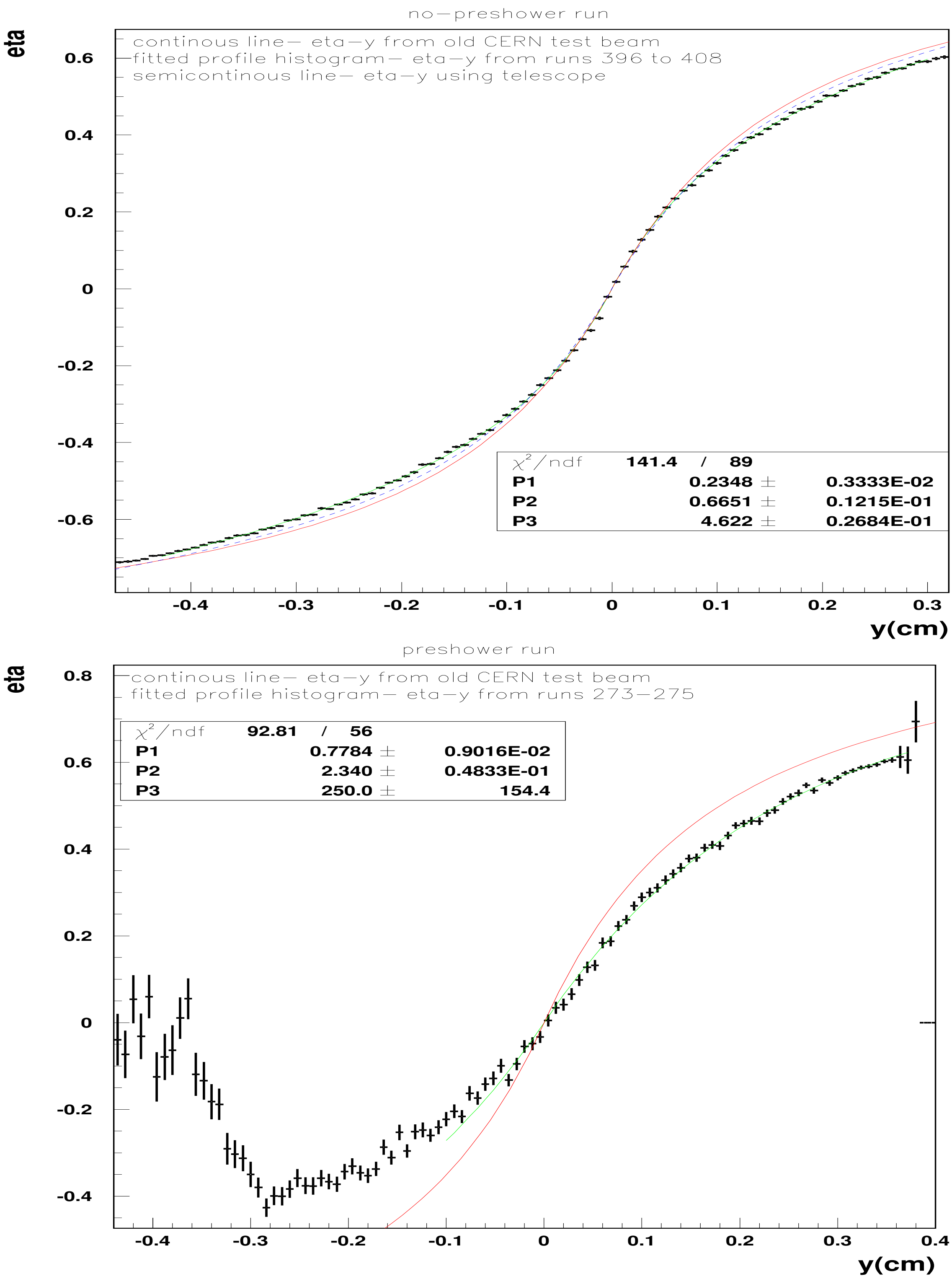

Figure 47: *The fitted η-y profile histograms for preshower(runs 273 and 275) and no-preshower(396,397,400,403,404,407,408) data sets, and the old CERN test-beam η-y transformation function. In the top plot also the η-y obtained from telescope data is shown.*

4.3 Data Analysis of the Telescope and implications for the TPOL Silicon

In this section, results from the Telescope will be used to assess the performance of the TPOL silicon. The Telescope event information was used, together with the geometry of the testbeam setup in order to predict the position of an event at the silicon strip detector in the TPOL. In addition, the efficiency of the TPOL silicon was estimated by using the Telescope to predict the position of hits in the TPOL. The Telescope pedestal and noise values are imported from a configuration file at run time, whereas the TPOL silicon pedestal and noise values for each strip are calculated for a particular run using events captured by the random trigger. The data runs used for this analysis were:
373, 374, 375, 376, 380, 382, 383, 384, 385, 386, 387, 388, 392, 393, 394.
All runs were taken with the TPOL preshower removed, and with the gated trigger. The beam energy for each run was 6 GeV.

4.3.1 Telescope Data Structure

Each event saved by the Telescope consists of ADC counts for those channels which exceeded threshold in each detector plane of the Telescope (i.e. T1,T2 and T3). The TPOL silicon data consists of a dump of the ADC counts of the entire 100 strips. The random trigger events were used offline to determine pedestals and noise as described above.

4.3.2 TPOL Position Performance

The predicted event position in the TPOL silicon was estimated using a track reconstructed in the Telescope detectors T1,T2 and T3. The track was then compared with the actual results from the TPOL silicon (see figure 48).

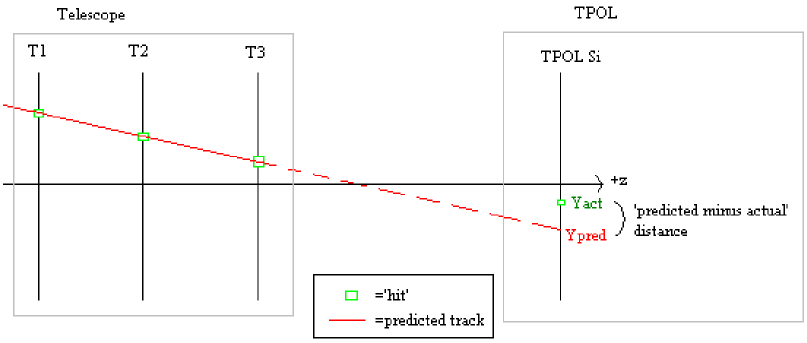

Figure 48: *The predicted and actual measurements from the TPOL.*

A correlation of predicted event position Y_{pred}, with recorded event position Y_{act}, on the TPOL silicon can clearly be seen in figure 49.

The data in the correlation consists of those events having registered one strip over 100 ADC counts in the horizontal and vertical strips of T1,T2,T3 and also over 9$\times$ rms noise in the (only horizontal) silicon strips of the TPOL. Events were excluded from this data if they were noisy (more than one strip registered over 3$\times$ rms noise), or if the silicon failed to record an event.

The criteria for an event were:

- in the TPOL silicon, a single strip registering greater than 9$\times$ rms noise
- no other strips in the TPOL silicon registering over 3$\times$ rms noise

Figure 50 is a histogram of the difference between predicted and actual position (in μm) at the TPOL silicon detector. The width of this distribution is 132.15 $\pm 2.86\mu m$.

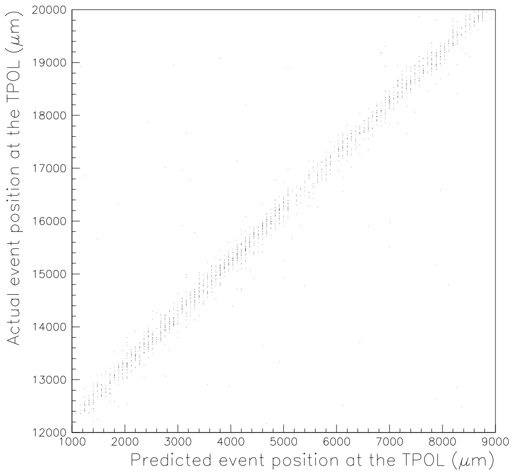

Figure 49: *The correlation of predicted and actual TPOL event position.*

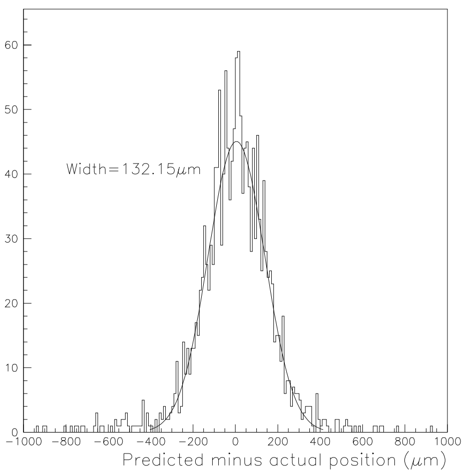

Figure 50: *The difference between predicted and actual event position at the TPOL silicon.*

4.3.3 Telescope Rotation Corrections

The possibility exists that the three Telescope detectors, T1, T2 and T3 were rotated with respect to each other, and also that the TPOL silicon was rotated with respect to the Telescope as a whole. This effect is important to consider when assessing the TPOL silicon position performance, as rotated detectors will cause systematic shifts in predicted TPOL position for tracks with different trajectories. To begin with, the Telescope's internal rotations were examined, and then the relative orientation of the TPOL silicon ascertained. To ascertain the internal rotations, two detectors are used to analyse the third. If a rotation is present, then a systematic shift of 'predicted minus actual' event position will be observed across the breadth of the detector, as in figure 51.

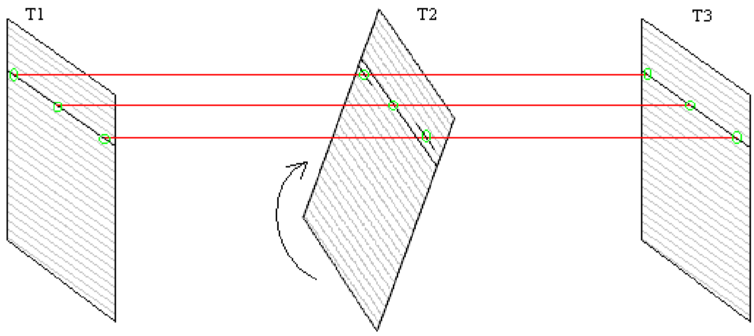

Figure 51: *The systematic shift of 'predicted minus actual' event position across the breadth of the detector arises from a relative rotation. Here, T1 and T3 are used to predict the 6th strip to fire for all three particle tracks, but the rotation means that the 7th,6th and 5th strips fire depending on the track's x coordinate.*

Luckily, some of the rotations (about the x and y axes in figure 52) are relatively unimportant, as they involve a *cosine* term, which hardly varies for small angles.

Rudimentary calculations for rotations about the x and y axes show that the apparatus is not sensitive to rotations $\leq 3.2^o$. A one-strip relative shift ($50\mu m$) across the entire breadth of the detector requires a relative rotation of

$$\theta = \cos^{-1}\left(\frac{639}{640}\right) \quad (= 3.2^o) \tag{26}$$

However, for relative rotations about the z axis, the situation is quite different. Rotations of as little as 0.08^o cause a one-strip shift across the breadth of the detector.

$$\tan^{-1}\left(\frac{50}{640 \times 50}\right) \quad = (0.08^o) \tag{27}$$

Hence, for this analysis, only rotations around the z axis are examined. The detector T1 was taken as the reference detector. Hits in T1 and T2 were used to predict the track

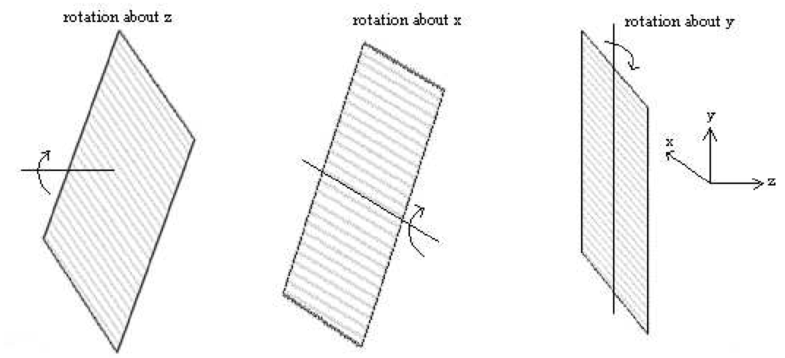

Figure 52: *Rotations which might be present at each detector.*

position at T3. Figure 53 (left) shows a scatter plot of the shift from left to right of the value of 'predicted minus actual' event position for detector T3. The other two scatter plots represent the shifts across T2 and T1 respectively.

An iterative fit was made to determine that a correction of 0.27^o around the z axis should be applied to T3 in order to make it 'flat' across the width. This is shown in figure 54.

Using the new T3 event position, T1 and T3 were once again used to re-predict the track position at T2 (see figure 54), and T2 and T3 were again used to predict the impact point on T1 (see figure 54). As can be seen from figure 54, both distributions are flat. This indicates that the rotation of T3 about the z axis is sufficient to align the Telescope. The next step is to consider the relative rotation between the Telescope (as a whole) and the TPOL silicon. Because of the absence of vertical silicon strips in the TPOL, the actual horizontal position of the event at the TPOL silicon must be estimated using the track through the Telescope. Thus, any systematic shift of 'predicted minus actual' event position across the width of the silicon is somewhat smeared horizontally. This effect simply increases the breadth of the 'band' but should not affect the overall slope. Before the rotation was applied to T3, the TPOL silicon showed (to within error tolerances) no appreciable systematic shift. After the rotation to T3, the systematic shift was again smaller than the error. This can be seen in figure 55. Hence, by simple rotation of T3 about the z axis, a satisfactory alignment has been determined.

After applying the rotation to T3, the distribution width at the TPOL silicon (from figure 50) is recalculated, and shows a negligible drop (to within errors). This is depicted in figure 56.

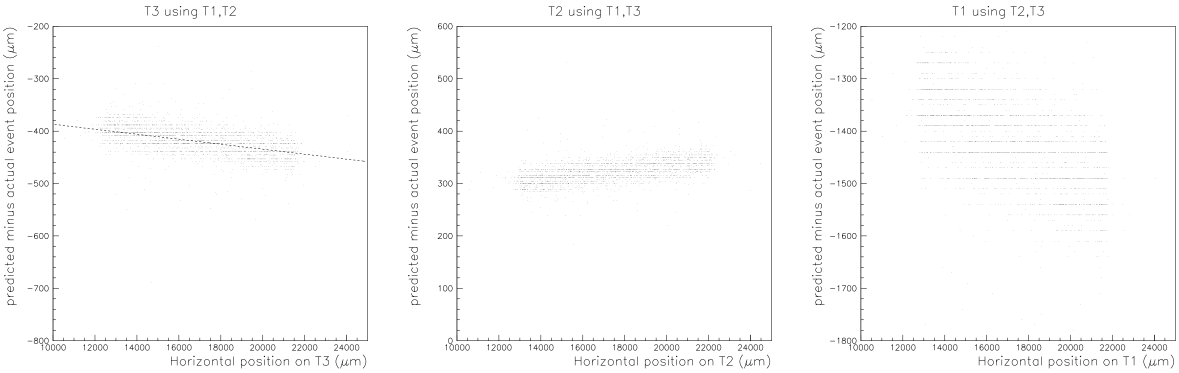

Figure 53: *Systematic shifts of 'predicted minus actual' event position across the widths of detectors T3, T2 and T1 (due to rotation about z-axis). NB the fit for T3 is* $y = -0.0047534x - 339.4$ *which corresponds to a* $\sim 47\mu m$ *(1 strip) shift from left to right.*

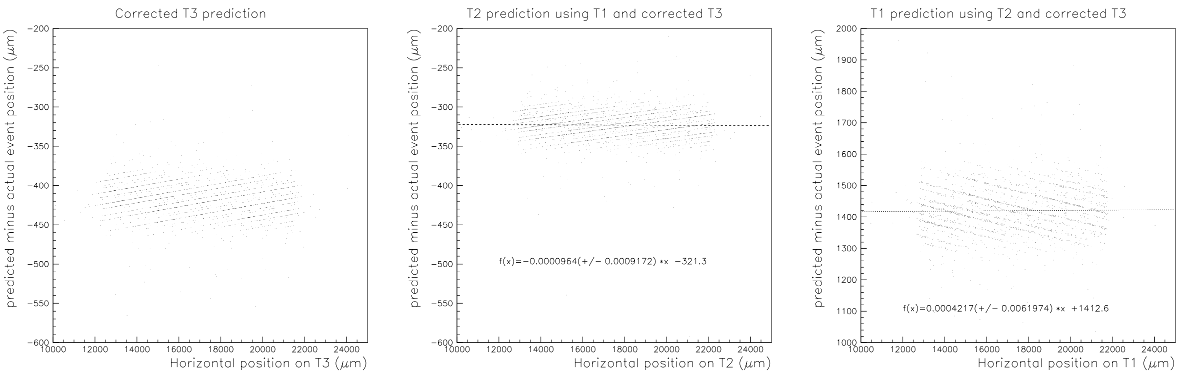

Figure 54: *Systematic shifts of 'predicted minus actual' event position across the breadths of T3,T2 and T1 are removed by rotating T3 about the z-axis*

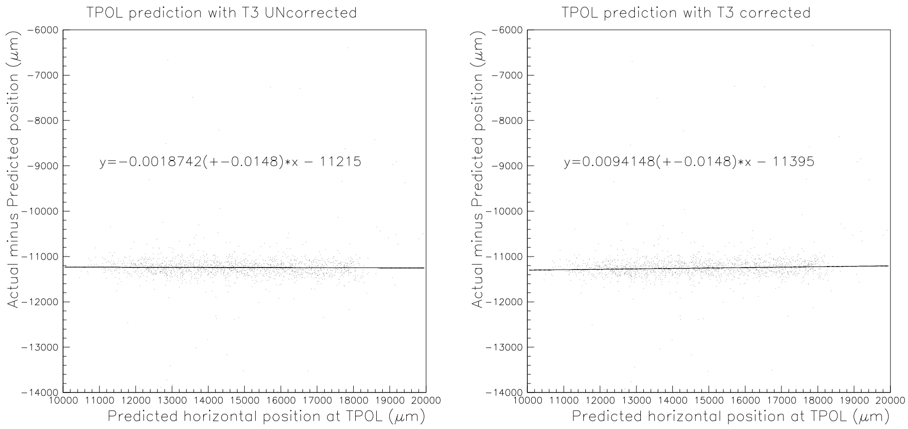

Figure 55: *Systematic shifts of 'predicted minus actual' event position across the TPOL silicon are removed by the rotation of T3. Left:T3 uncorrected Right:T3 corrected*

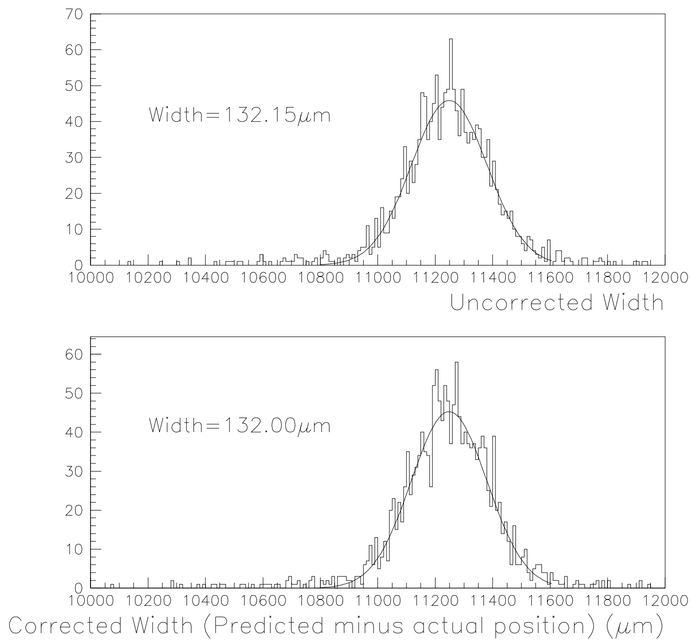

Figure 56: *The widths of the distributions of predicted minus actual event position. Top:T3 uncorrected Bottom:T3 corrected*

4.3.4 Monte-Carlo Simulation of Multiple Coulomb Scattering

The charged particles in the 6 GeV beam interact with matter as they pass through it. The majority of the interactions are simply small angle Coulomb scattering. The Particle Data Group [20] gives the following formula to estimate the Gaussian width of a Multiple Coulomb Scattering (MCS) distribution.

$$\theta_{space} = \frac{13.6MeV}{\beta cp} z \sqrt{\frac{x}{X_0}} \left(1 + 0.038 \ln \left[\frac{x}{X_0}\right]\right) \tag{28}$$

Where x/X_0 is the number of radiation lengths of material present, z is the particle charge, β is the particle velocity relative to that of light in a vacuum c, and p is the particle momentum. The various values of θ_{space} for each of T1,T2,T3, the 'dead' detector and the TPOL light-tight 2 mm Aluminium box were calculated. These angles were then corrected into θ_{plane}.

$$\theta_{plane} = \frac{\theta_{space}}{\sqrt{2}} \tag{29}$$

This correction arises from the fact that we are sensitive to the MCS only in the z-y plane. In practice, MCS will cause particles to emerge at an angle θ_{space} which is rotated about the z axis by a random amount between 0 and 2π. This effect reduces the MCS scattering projection in the z-y plane by a factor of $\sqrt{2}$. A Monte-Carlo simulation was performed (in the $x-z$ plane) in order to make an estimate of the effect of MCS on the observed width. This was done as follows: The data at T1 and T3 were smeared to simulate the resolution of the strip detectors ($50/\sqrt{12}\ \mu m$), and the Multiple Coulomb Scattered track created by Monte-Carlo simulation was overlayed onto this, providing a Monte-Carlo impact point at the TPOL Silicon. This was then compared with the predicted impact point on the TPOL silicon (which was generated using the proper track through the Telescope). The width obtained (see figure 57) was 102 μm ± 1.

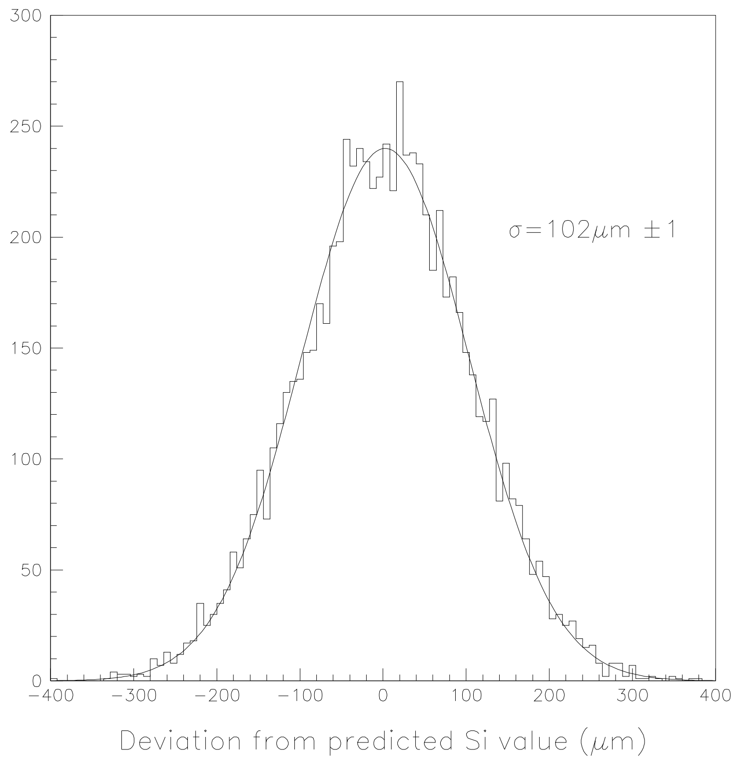

Figure 57: *Monte-Carlo simulation of MCS.*

4.3.5 Geant Simulation of Multiple Coulomb Scattering

The Particle Data Group [20] formula (28) provides a Gaussian width θ_0, which it states is sufficient to describe the central 98% of the distribution. In reality, the scattering is much more accurately described by the theory of Molière [21]. The distribution is roughly Gaussian for the central portion of the distribution, but has larger tails at larger scattering angles. The Particle Data Group [20] states that their approximation is accurate to 11% or better for $10^{-3} < x/X_0 < 100$. For the scattering considered in the test beam, x/X_0 is indeed inside the range stipulated, however the number of surfaces of scattering magnifies any error in the Monte-Carlo distribution, with the error on one surface feeding into the input for the next surface. For this reason it was decided to attempt a more accurate simulation. Geant code was used to simulate the scattering, and T1 and T3 smeared to allow for the telescope resolution (as in the previous section). A Gaussian fit was performed, and the width obtained was 138 ± 1.5 μm (figure 58). There are also error sources on this estimation of the width, but the observed width of 132 ± 3 μm is consistent with good performance of the TPOL and the simulation.

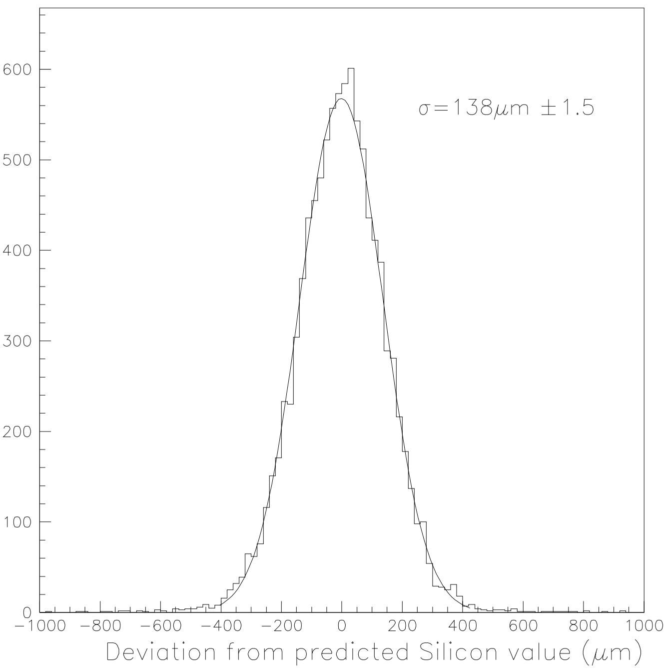

Figure 58: *Geant Monte-Carlo simulation.*

4.3.6 Multiple Coulomb Scattering Estimation Using Variances

The effect of MCS was also estimated by propagating the uncertainties introduced by scattering in the various pieces of material. The beam was defined by events at detectors T1 and T3. The error on the position measurements (i.e. σ_{T3} and σ_{T1}) was taken to be the theoretical resolution for the strip detector $50/\sqrt{12}\ \mu m$. Thus, the variances of the position measurements at T1 and T3 were

$$Var(T1) = \sigma_{T1}^2 \tag{30}$$

$$Var(T3) = \sigma_{T3}^2 \tag{31}$$

The scattering angles at each scattering surface $\theta_1, \theta_d, \theta_2, \theta_3, \theta_{Al}$ were calculated using equation 28). Next, the gradient of the track through the telescope is determined as shown in figure 59. From the equation

$$T_4 = T_3 \ + \ Z_4 m_3 \ + \ Z_4\theta_3 \ + \ (Z_4 - Z_{Al})\theta_{Al}, \tag{32}$$

the following equation is derived

$$Var(T_4) = Var(T_3) + Z_4^2 Var(m_3) + Z_4^2 Var(\theta_3) + (Z_4 - Z_{Al})^2 Var(\theta_{Al}) + Z_4 Cov(T_3, m_3) \tag{33}$$

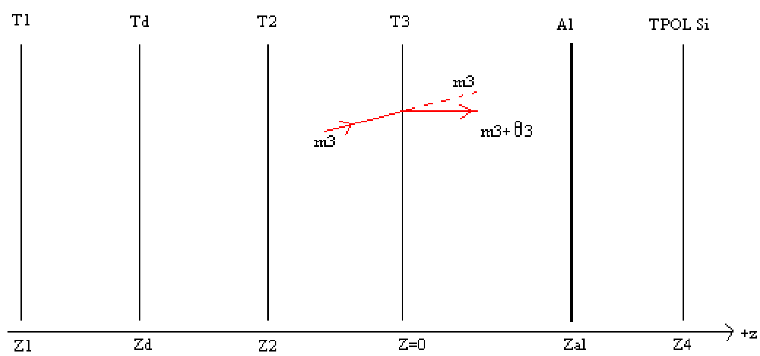

Figure 59: *The gradients and scattering angles for the surfaces in the Telescope-TPOL system. $z = 0$ at the detector T3. The track has gradient m_3 prior to hitting T3, and then is scatterd by an angle θ_3. In the small angle approximation the deflection can simply be added.*

With reference to figure 59, the relationship 34 may be written.

$$T_3 = T_1 - Z_1 M_3 - Z_d\theta_d - Z_2\theta_2. \tag{34}$$

Re-arranging

$$m_3 = \frac{1}{Z_1}(T_1 - T_3 - Z_d\theta_d - Z_2\theta_2) \tag{35}$$

For two uncorrelated distributions $< \Delta x \Delta y >= 0$, hence

$$Cov(T_3, m_3) = \frac{-1}{Z_1} Var(T_3), \tag{36}$$

From equation (35),

$$Var(m_3) = \frac{1}{Z_1^2}\left(Var(T_1) + Var(T_3) + Z_d^2 Var(\theta_d) + Z_2^2 Var(\theta_2)\right) \tag{37}$$

Therefore, from equations (33 to 37) we obtain

$$Var(T_4) \simeq 120\ \mu m \tag{38}$$

This result is close to the result expected, however its use is limited as the Gaussian approximation is only valid to $\sim$11%.

4.3.7 TPOL Silicon Efficiency

For this analysis, 'events' were considered to be those having passed threshold (>100 ADC counts) in both horizontal and vertical sections of the detectors T1,T2 and T3. The efficiency of the TPOL silicon was estimated by analysing its response to these events. The silicon was deemed to have responded if there was a signal over 3×rms noise. The cleanliness of the signal was not considered, and neither was cluster finding, but a good indicator of the validity of the approach is gained from the distributions of the 'predicted minus actual' event position at the TPOL silicon. One would expect the width of the distribution to increase markedly if the prediction were inaccurate (i.e. the silicon had not responded correctly). As can be seen in figure 60, the clean events with a single strip 9× rms noise response (and nothing else over 3× rms) have a similar width to 'noisy' events which have a 9× rms response *and* some other strips reaching over 3× rms. They also have a similar width to those events having only strips exceeding 3× rms noise. Hence, for the efficiency calculation, all these events are included as signal.

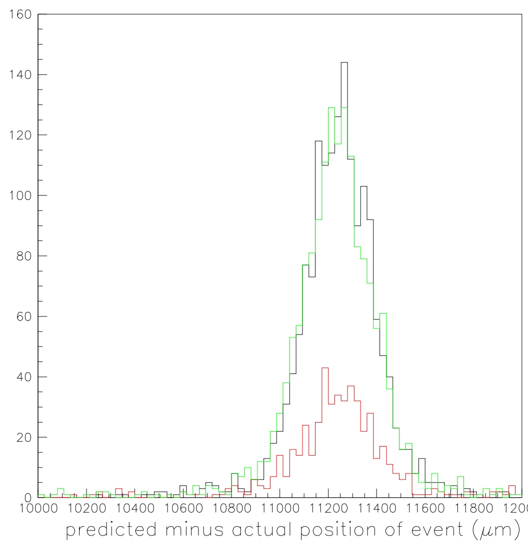

Figure 60: *Widths for clean 9rms signal (black), noisy 9rms signal (red) and 3rms signal (green).*

Those events having no TPOL silicon response over 3× rms noise are not seen by the TPOL, and, as we shall see, most of these events miss the $\sim 1cm^2$ TPOL silicon, and so are excluded from the efficiency calculation. To determine which events do not register in the TPOL silicon because they miss the detector, the extremities of the TPOL silicon must be determined. This calculation is complicated slightly by the fact that the beam was not uniform over the area of the Telescope detectors T1,T2 and T3. In fact the beam was quite weak near the edges of these detectors. For this reason it is necessary to examine the *ratio* of events having no signal in the TPOL silicon to those having a signal in the TPOL, and to see how this ratio varies as we scan across the predicted event positions at the TPOL silicon. In figure 61, marked changes in the ratio can be seen at the edges of the TPOL silicon.

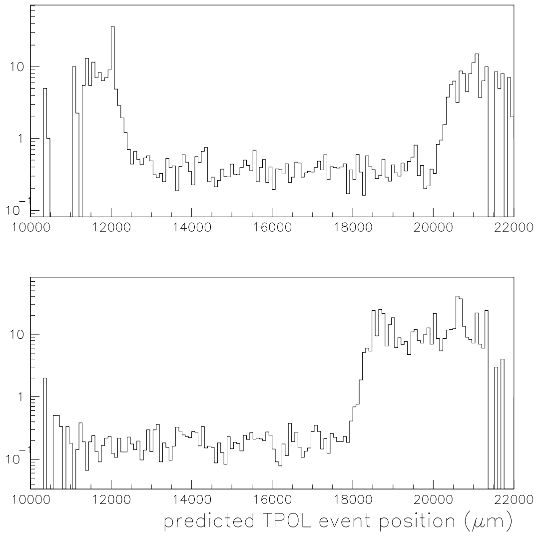

Figure 61: *Log plot of ratios of events having no signal in the TPOL to those having a TPOL signal. (Top:Vertical position Bottom:Horizontal position)*

For this reason the boundaries used for the efficiency calculation were set at:

- Vertical position (horizontal strips):13000 $\rightarrow$ $20000\mu m$
- Horizontal position:11000 $\rightarrow$ $18000\mu m$

Note that the effect is very small at one side of the TPOL silicon. This is primarily due to weak beam in this area and as such, the results simply represent low statistics. This can be seen in figure 62, which shows (in black) the predicted impact position on the TPOL silicon for both vertical and horizontal impact positions. In red are plotted the events which were predicted by the Telescope, but did not register in the TPOL silicon. These events lie inside the boundaries of the opposite direction to the plot, so the only reason they did not register *should* have been that they missed the silicon in the direction plotted. Clearly, the bunching around the boundaries set previously implies their correctness.

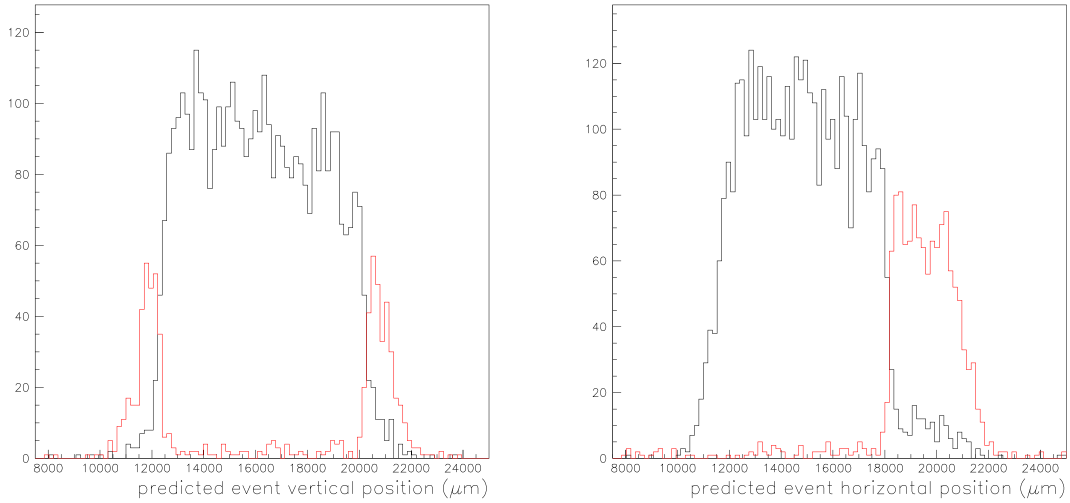

Figure 62: *Left:Vertical position of events (black) and events where the TPOL did not register (red) with a cut on* ***horizontal position inside 11-18000*** *μm. Right:Horizontal position of events (black) and events where the TPOL did not register (red) with a cut on* ***vertical position inside 13-20000*** *μm.*

When these cuts are applied, the events with TPOL silicon signal as a fraction of all events represents the true efficiency. This can be seen in figures 63 and 64. The TPOL silicon efficiency is uniform across the detector, and is approximately 97.8%.

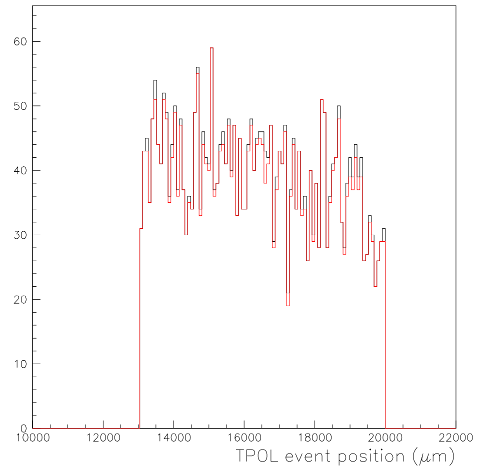

Figure 63: *Events in the TPOL (red) and the predicted events in the TPOL (black).*

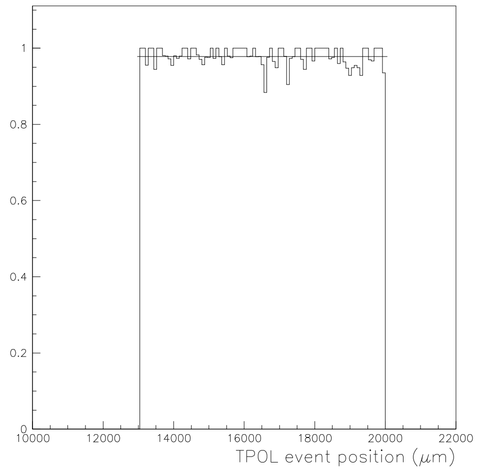

Figure 64: *Efficiency of the TPOL silicon as a function of position.*

4.4 Data Analysis and Results from the Fiber Detector

This section shows the results of the analysis of the data from the fiber detector. In order to determine the linearity of the calibration, dedicated runs were taken with the Ungated Trigger. The analyses have been done using both data sets: with and without the pre-shower.

Figure 65 shows the distributions of the y position reconstructed from the silicon detector. The upper and lower figures were obtained from the data with and without the pre-shower, respectively. The open histograms shows the y distributions from the inclusive samples of Ungated Trigger events. On the other hand, the shaded histograms represent the events, in which the Fiber Trigger was fired. As seen in the both figures, peaks were observed around the geometrical fiber position by requiring the Fiber Trigger.

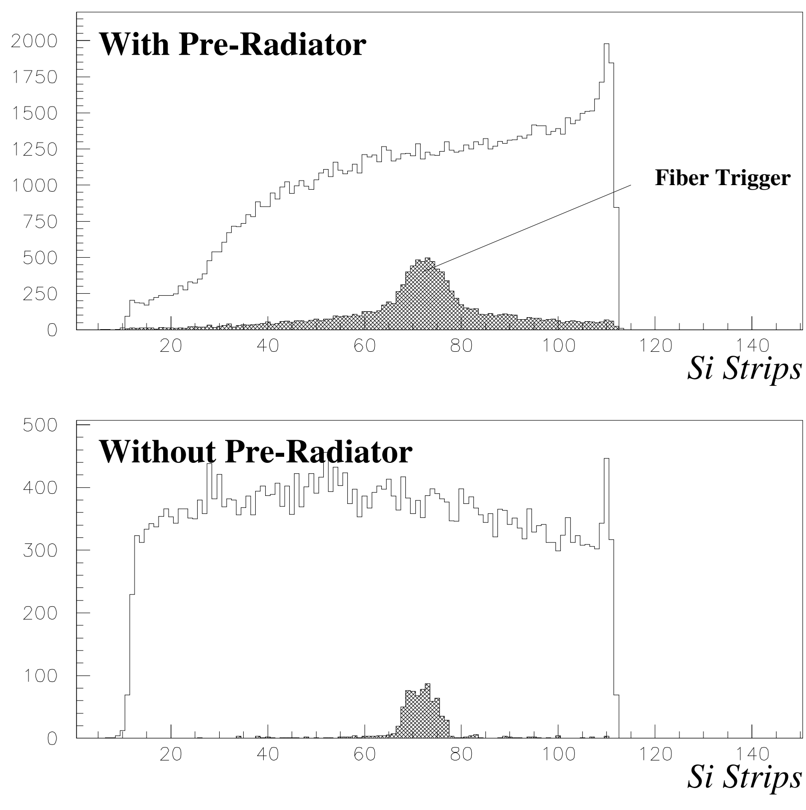

Figure 65: *The distributions of the y position reconstructed from the silicon detector. The unit of the horizontal axis is the physical silicon strip channel. The reconstructed y positions look different in the two plots because the complete detector was moved by 2mm upwards for "without pre-shower" data taking.*

As a result of Gaussian fits to those peaks, the σ values were found to be about 0.4 mm. That is comparable with the fiber radius, 0.5 mm. For the events with pre-shower, the particle multiplicity increased at the position of the silicon and the fiber detectors. Then, with the pre-shower, there tended to be more events whose reconstructed y positions with the silicon detector were away from the fiber peak, compared those without the pre-shower. This is the reason why we observed more tails in the upper figure of Fig 65.

During the data-taking, we changed the vertical position of the fiber detector in 1 mm steps, using metal rings of various diameters at the bottom of the fiber detector, which supported the fiber detector. Figure 66 and 67 show distributions of the reconstructed y position of the Fiber Trigger events, with and without the pre-shower. In all cases, the expected shifts of the peak positions was observed. In each position, a Gaussian was fitted to the y distribution. The mean values (y_{Si}) obtained are compared with the geometrical fiber position (y_{fib}) in Fig. 68.

Figure 68 shows the obtained y_{Si} values as a function of y_{fib}. The circle and triangle points represent the results from data with and without the pre-shower, respectively.

In both cases, the center position of the silicon detector was shifted by about 1.6 mm from the center of the fiber detector, which was aligned to the center of the calorimeter. This turned out to be due to the mis-alignment of the silicon detector.

In addition to the above problems, systematic shifts of about 80 μm were seen between the data with and without the pre-shower. In between the collection of both data sets, a visual telescope measurement scan was carried out by a specialized DESY team, which confirmed that the height of the fiber detector could be varied by means of replacing the metal rings with an accuracy of $\leq 50\,\mu$m. The reason for the systematic shift has not yet been understood.

Straight line fits were performed for the data with and without pre-shower. The lines shown in Fig 68 are the results of the fits. In both cases, the slope parameters were consistent with unity. The inserted histogram shows the distribution of the residuals of y_{Si} from the results of fits (y_{fit}). As seen in the figure, the residuals are distributed well within $\pm 40\,\mu$m. From this result, we conclude that the precision of the linearity calibration using the fiber detector was $\leq 40\,\mu$m in our current setup.

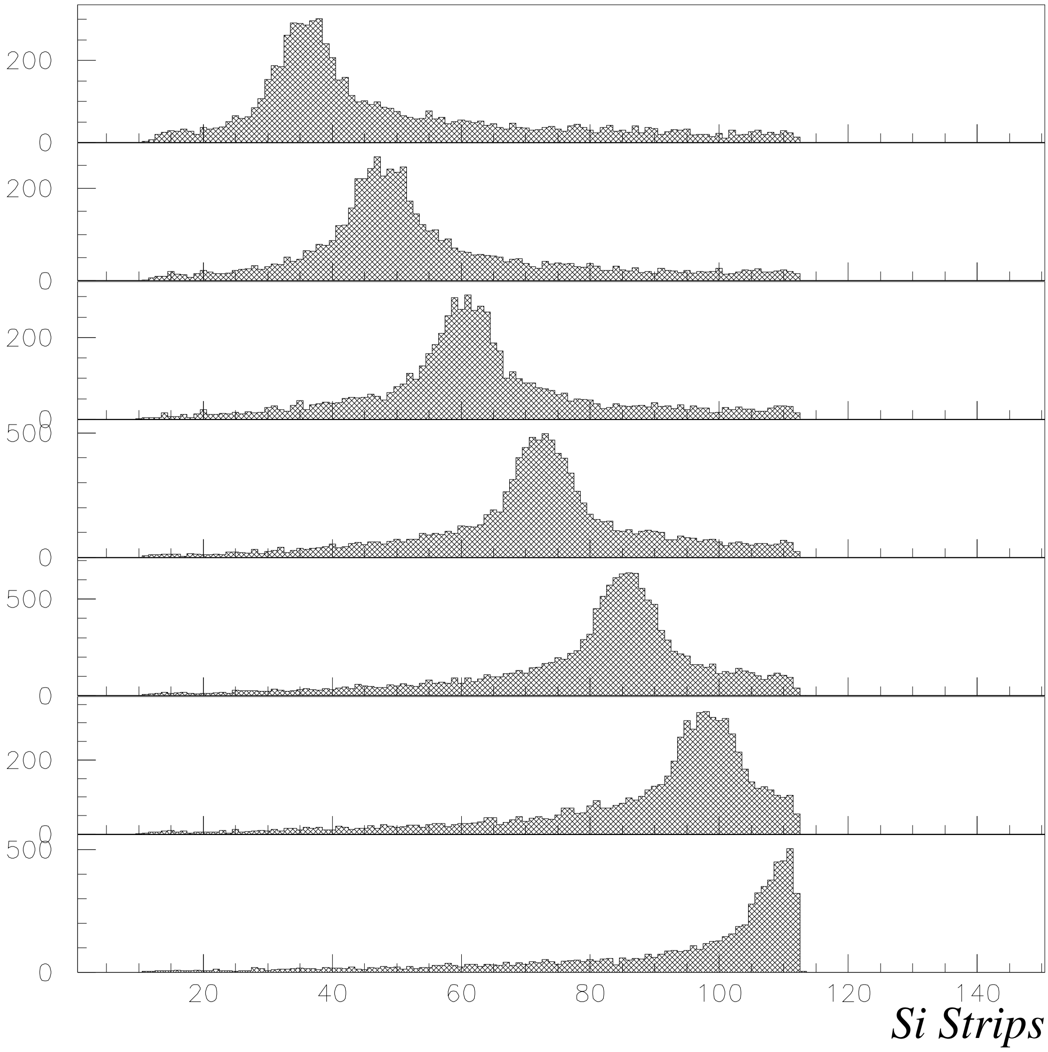

Figure 66: *The reconstructed y position distributions of the Fiber Triggered events. The data were taken with the pre-shower. The geometrical fiber vertical positions were adjusted to be* $y_{fib} = -4, -3, -2, -1, 0, +1, +2$ *with respect to the center of the calorimeter, by changing the different diameters of metal rings at the bottom of the detector.*

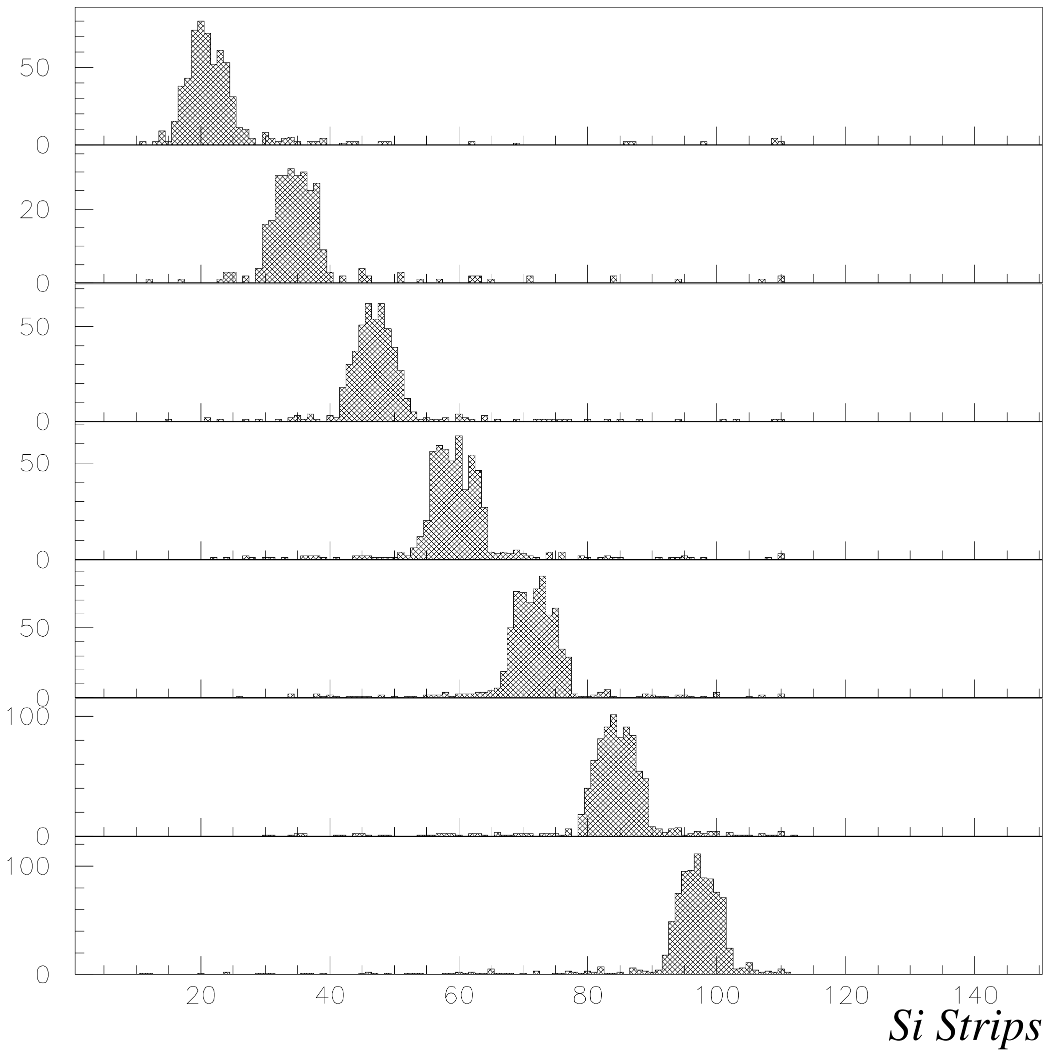

Figure 67: *The reconstructed y position distributions of the Fiber Triggered events. The data were taken without the pre-shower. The geometrical fiber vertical positions were adjusted to be* $y_{fib} = -5, -4, -3, -2, -1, 0, +1$ *with respect to the center of the calorimeter, by changing the different diameters of metal rings at the bottom of the detector.*

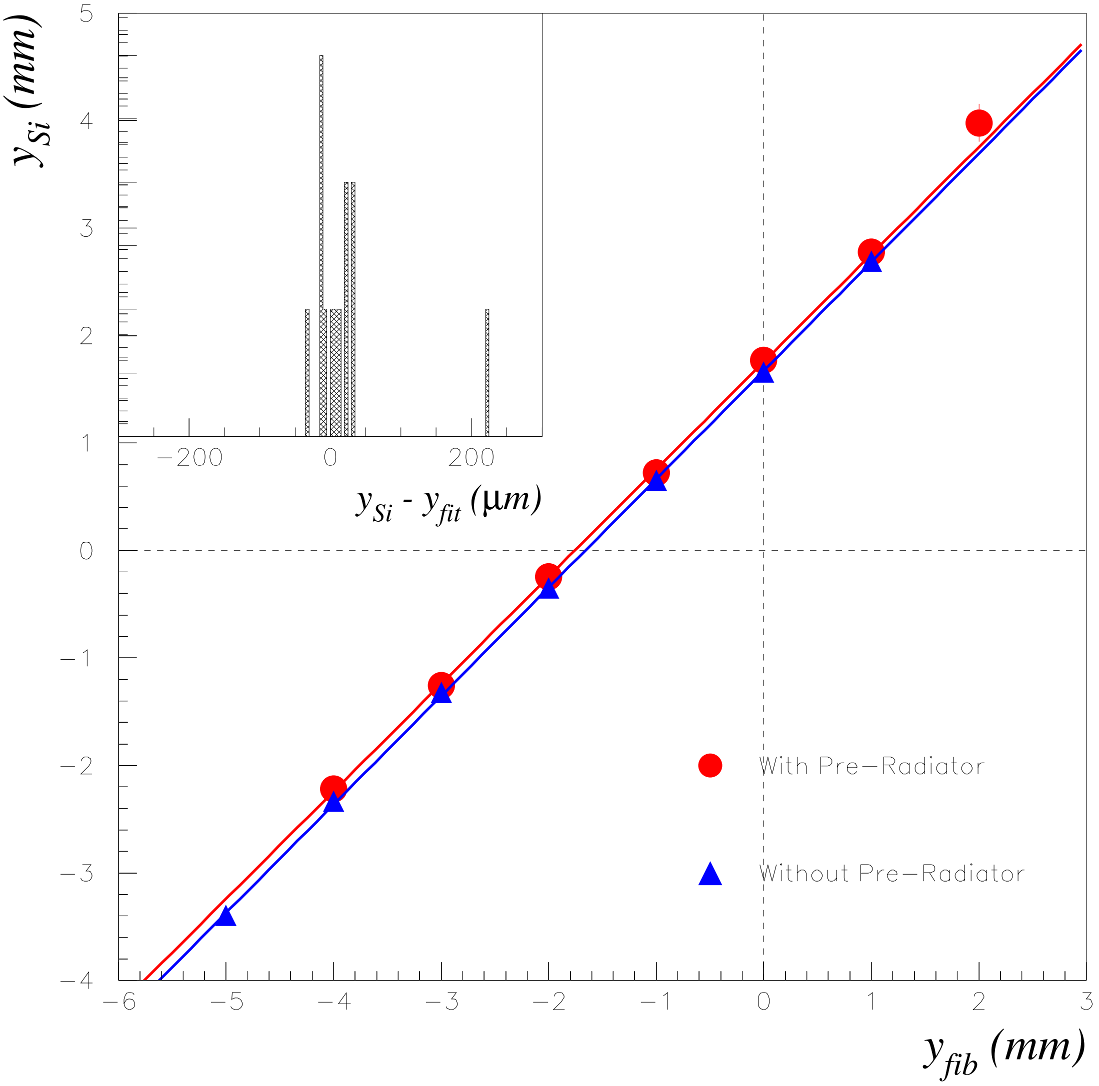

Figure 68: *The mean values of y distributions (y_{Si}) as a function of the geometrical fiber position (y_{fib}). The circles and triangles represent the results from the data with and without the pre-shower, respectively. The lines show the results of fits to linear functions. The inserted histogram show the residuals of y_{Si} from the results of fits.*

4.5 Conclusions

The TPOL group carried out an electron test-beam measurement at DESY in January-February 2001, of the modified TPOL polarimeter i.e. a position sensitive detector (silicon and fiber detectors) was installed together with the TPOL calorimeter, for test-beam data taking The DESY test-beam results have been positive and can be summarized as following:

- Calorimeter: very good linearity and spatial uniformity of the calorimeter, energy resolution $\sigma_E = 26\%$, spatial resolution $\sigma_y = 0.4\ mm$ at 6 GeV $y = 0$.
- Silicon Detector: Strip signal to noise ratio S/N$\sim$21 except for some noisier channels. The cluster signal distribution (no-preshower) has a Landau shape and the cluster mean S/N ratio is $\sim$25. The optimal silicon bias voltage is $\sim$-80 V. The default voltage bias during the test-beam was -100 V, if the optimal bias voltage is used ($\sim$-80 V) then the S/N ratio should increase noticeably. The η-y transformation was measured with a relatively good precision.
- Telescope: Results and analysis are consistent with TPOL silicon detector being limited by a resolution of $< 50\ \mu m$.
- The TPOL silicon efficiency was spatially uniform and was $\sim 97.8\%$
- Fiber Detector: the precision of the linearity calibration is better than 40 μm.

The incident Compton photon energy range is between 5-14 GeV; so to make a proper study of the η-y transformation higher energies are required. A future test-beam is foreseen at CERN at the end of July 2001, with energies up to 50 GeV. The new TPOL setup will be tested there i.e. the TPOL calorimeter, fiber detector and a 6*6 cm^2 silicon detector.

Acknowledgments

We thank several people at IC-London for the work done, advice and support given, in building the silicon microstrip prototype detector and for the test beam preparation: B. Cameron, M. Raymond, A. K. Jamdagni, L. Toudup, S. Greenwood, M. Kasey, M. Khaleeq, G. Barber, P. Savage D. R. Price, I. Clark and D. Clark.

We would like to thank G.Barber and P.Savage for the mechanical design and construction of the fiber detector. We are also grateful to K.Tokushuku who provided us the scintillating fibers and gave us the valuable advice throughout the experiments. We also thank the financial support by the Japanese Ministry of Education, Science and Culture.

We thank Peter Schuler, for his collaboration in preparing and modifying the spare TPOL calorimeter that was used in the test-beam.

We thank Ties Behnke, the POL2000 coordinator, for his constant interest and advice, in the preparation and the running of the test-beam.

We thank Maria C. Petrucci, for her support and collaboration throughout the whole test-beam period, in particular regarding the usage of the test-beam silicon telescope.

We thank Ulrich Koetz, for giving us the possibility to use the T22 test-beam line.

We thank Norbert Meyners, for explaining us the safety and operation procedures of the T22 test-beam area, and also for helping us with the installation technicalities.

We thank Dr John Hart for his assistance in using error propagation to analyse the the Telescope.

References

[1] R.J.Cashmore et al., *Electroweak Physics at HERA: Introduction and Summary, Proceedings of the Workshop: Future Physics at HERA Vol.1, edited by G.Ingelman, A.De Roeck and R.Klanner, Hamburg (1996) 129.*

[2] F.Zetsche, *Lepton Beam Polarisation at HERA,ibid. 222.*

[3] R.Beyer et al., *Electroweak Precision Tests With Deep Inelastic Scattering at HERA, ibid. 140.*

[4] O.Deppe et al., *Measurement of Weak Neutral Current Couplings of Quarks of at HERA,ibid. 163.*

[5] Polarization 2000 Group, *Polarization 2000, DESY-PRC 98-07 (1998).*

[6] D.P. Barber et al., *The HERA polarimeter and the first observation of electron spin polarization at HERA*, 1993.

[7] D.P. Barber et al., Nucl. Inst. Meth. **A 338**, 166 (1994).

[8] M.Ruh et al., *Construction and Beam Test of a Spare Calorimeter for the HERA Transverse Polarimeter.* Internal Polarimeter Report 97-05 (1997).

[9] M.Milite, *The ZEUS muon-VD and Testbeam Results.* Http://www.desy.de/m̃ilite/studentseminar.ps.gz. The transparencies shown at ZEUS student seminar.

[10] ZEUS Coll., U. Holm (ed.), *The ZEUS Detector.* Status Report (unpublished), DESY, 1993, available on `http://www-zeus.desy.de/bluebook/bluebook.html`.

[11] ATLAS collaboration, *ATLAS98-99 Silicon microstrip detector layout*, 1999, available on `http://www-ccint.kek.jp/managers/silicon/si_det.html`.

[12] L.L. Jones et al., *The APV25 Deep Submicron Readout Chip for CMS Detectors.* In Snowmass 1999, Electronics for LHC experiments 162-166, 1999, available on `http://www.te.rl.ac.uk/med`.

[13] *FIC 8234 Dual 68040 Fast Intelligent Controller User's Manual*, 1993, available on `http://www.ces.ch`.

[14] E. Murer, *VI2C-manual*, 1997.

[15] G. Claus, W. Dulinski, A. Lounis, *Strip Detectors Read-Out System user's guide.* CRN 96-33, 1996.

[16] M. Morrissey, *SEQSI-manual*, 1996.

[17] R.Hamatsu, *Study of radiation dose in the silicon detector of the TPOL polarimeter using GEANT*, 2000, available on `http://heal1.phys.metro-u.ac.jp/~hamatsu/StudyOfTPOLDose.html`.

[18] R.Hamatsu, M.Inuzuka, K.Matsuzawa, *Proposal for the experiment in Jan, 2001*, available on
http://www-zeus.desy.de/~inuzuka/pol2000/documents/pro.ps.gz. Setup for Test Beam at DESY.

[19] N. Meyners. Private communication.

[20] *The European Physical Journal C, Vol. 15 Number 1-4, p166 (2000).*

[21] *Geant v3.13 modules GMOLI.FPP & GMOLS.FPP*, available on
http://wwwinfo.cern.ch/adsoc/geant_html3/note247.html.